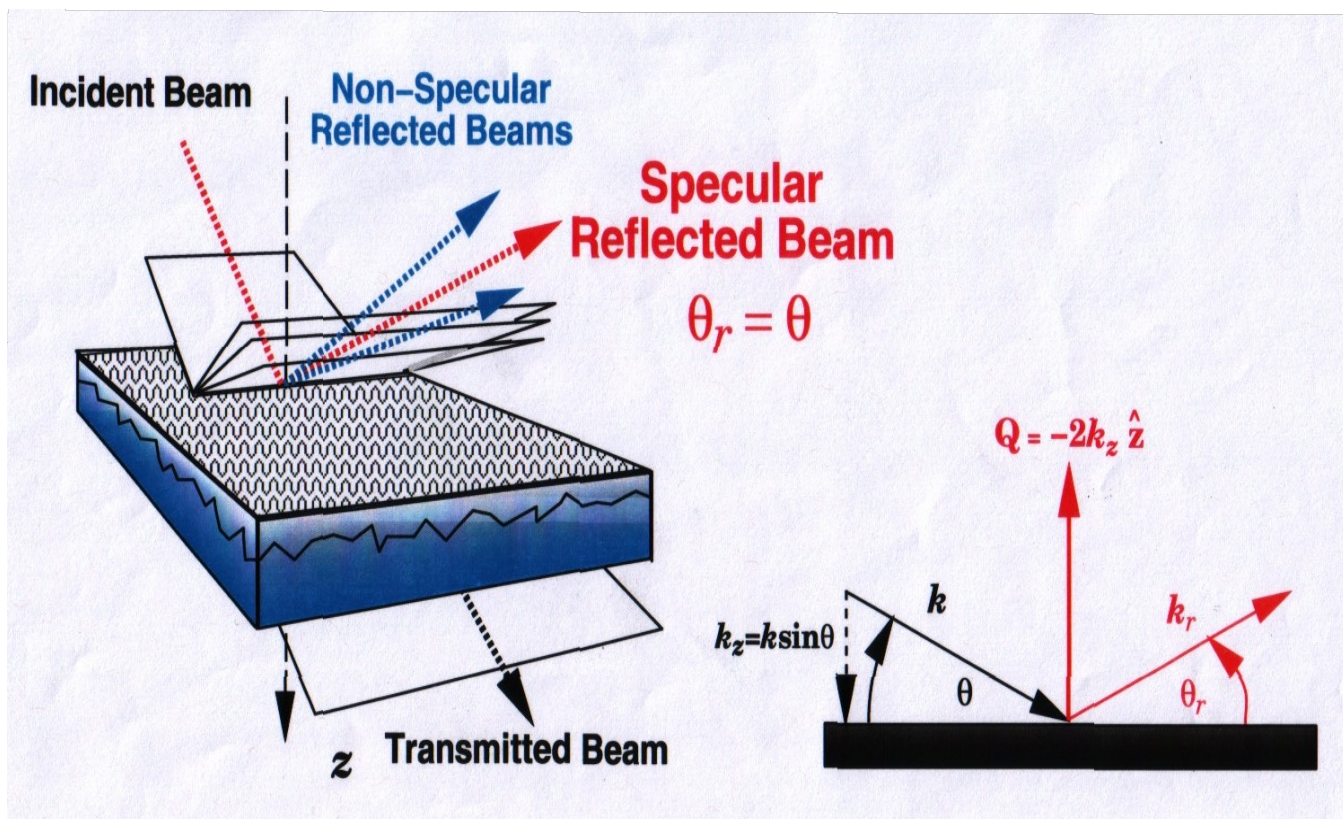


National School on Neutron and X-Ray Scattering

Argonne and Oak Ridge National Laboratories

Neutron Reflectometry

24 June 2014



(Figure courtesy of Norm Berk)

C.F.Majkrzak, *NIST Center for Neutron Research*,
Gaithersburg, MD

Part 1: Basic reflectometry concepts

Part 2: Neutron wave characteristics and coherence

Part 3: The phase problem, direct inversion and simultaneous fitting

Part 4: Applications of NR to studies of the nano-scale structure of thin film materials

Appendices

Bibliography

Part 1: Basic Reflectometry Concepts

- <> general notes
- <> probing structure beneath the surface boundary
- <> scattering length density (SLD) depth profiles
- <> specular reflection from a *flat* object
- <> wave/particle behavior
- <> coherence length -- plane waves and wave packets
- <> spatial and Q resolutions
- <> non-specular scattering

Principal Uses and Advantages of Neutron Reflectometry:

- * For the specular condition, provides the chemical (isotopic) scattering length density (SLD) depth profile along the surface normal with a spatial resolution approaching half a nanometer.
- * With polarized neutrons, provides the *vector* magnetization depth profile of a ferromagnetic material.
- * Isotopic contrast, particularly applicable to hydrogen and deuterium.
- * A non-destructive probe which can penetrate macroscopic distances through single crystalline substrates, making possible reflection studies of films in contact with liquids within a closed cell.
- * As a consequence of the relatively weak interaction between the neutron and material, a remarkably accurate theoretical description of the reflection process and quantitative analysis of the data is possible, although the Born approximation is often not valid and an “exact” or “dynamical” formulation is required.

Importance of Sample System Preparation

- > The great success in using neutron reflection/diffraction to study thin film systems of hard condensed matter, in particular the structures and fundamental interactions in magnetic materials, is largely due to the ability to tailor, with atomic-layer accuracy and precision, single-crystalline, layered sandwiches and superlattices (using vapor deposition techniques such as molecular beam epitaxy in ultra-high vacuum). Advances in film deposition techniques and lithography continue at a remarkable rate.
- > Similarly, neutron reflectometry in principle can be applied as a probe to further our understanding of the structure and function of molecules in lipid membranes, of relevance in biology and bioengineering, when comparable control over the fabrication of model systems is achieved. Great progress has been made toward realizing this goal in practice. However, we are still at a relatively early stage of development in our ability to engineer soft condensed matter films on atomic and nanometer scales. Progress can be expected as efforts in creating and manipulating membrane / molecular systems accelerates.
- > Employing phase-sensitive methods in reflectivity measurements ensures a unique scattering length density (SLD) depth profile. Additional application of hydrogen / deuterium substitution techniques and comparison with molecular dynamics calculations assures a correspondingly high degree of certainty of obtaining an unambiguous chemical composition depth profile.

Why is specular neutron reflectometry so special?

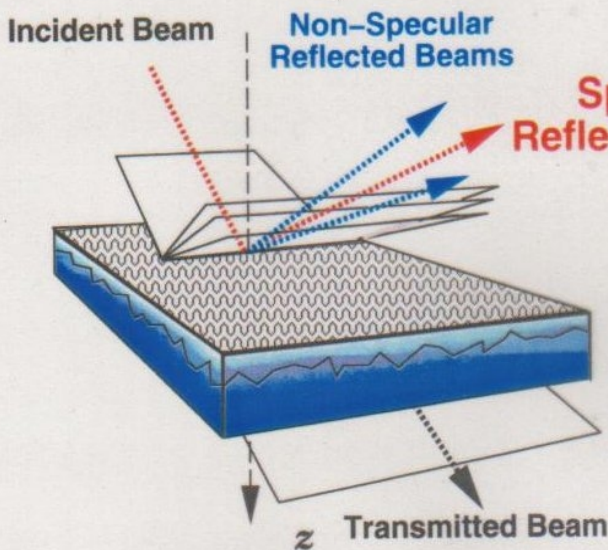
<> Neutron reflectometry (NR) is a valuable probe of the structure of both hard and soft condensed matter in thin film or multilayered form -- particularly for hydrogenous and magnetic materials. NR can see *beneath* the surface and provide quantitative structural information from *everywhere within* the film on a nanometer scale.

<> Both “forward” and “inverse” scattering problems for specular neutron reflection are mathematically solvable, exactly, from first-principles quantum theory. The mathematically unique solutions are thus far only possible in one dimension and for non-absorbing potentials of finite extent.

<> Phase-sensitive neutron specular reflectometry, employing references, enables direct inversion of composite reflectivity data sets to yield a unique scattering length density depth profile for an “unknown” film of interest, without fitting or any adjustable parameters.

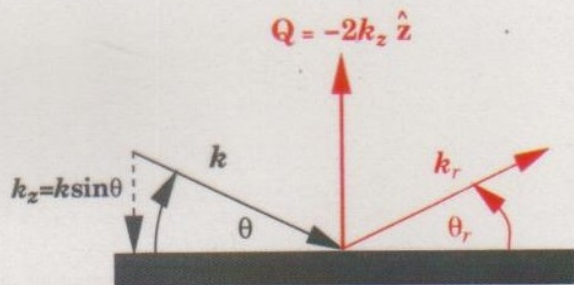
<> The spatial resolution and accuracy of the SLD profile thereby obtained is limited only by the statistical uncertainty in the measured reflected intensities and truncation of the reflectivity data sets at the maximum value of wavevector transfer attainable.

$$\text{Reflectivity} = \frac{\text{Number of reflected neutrons}}{\text{Number of incident neutrons}} = |r|^2$$



Specular Reflected Beam

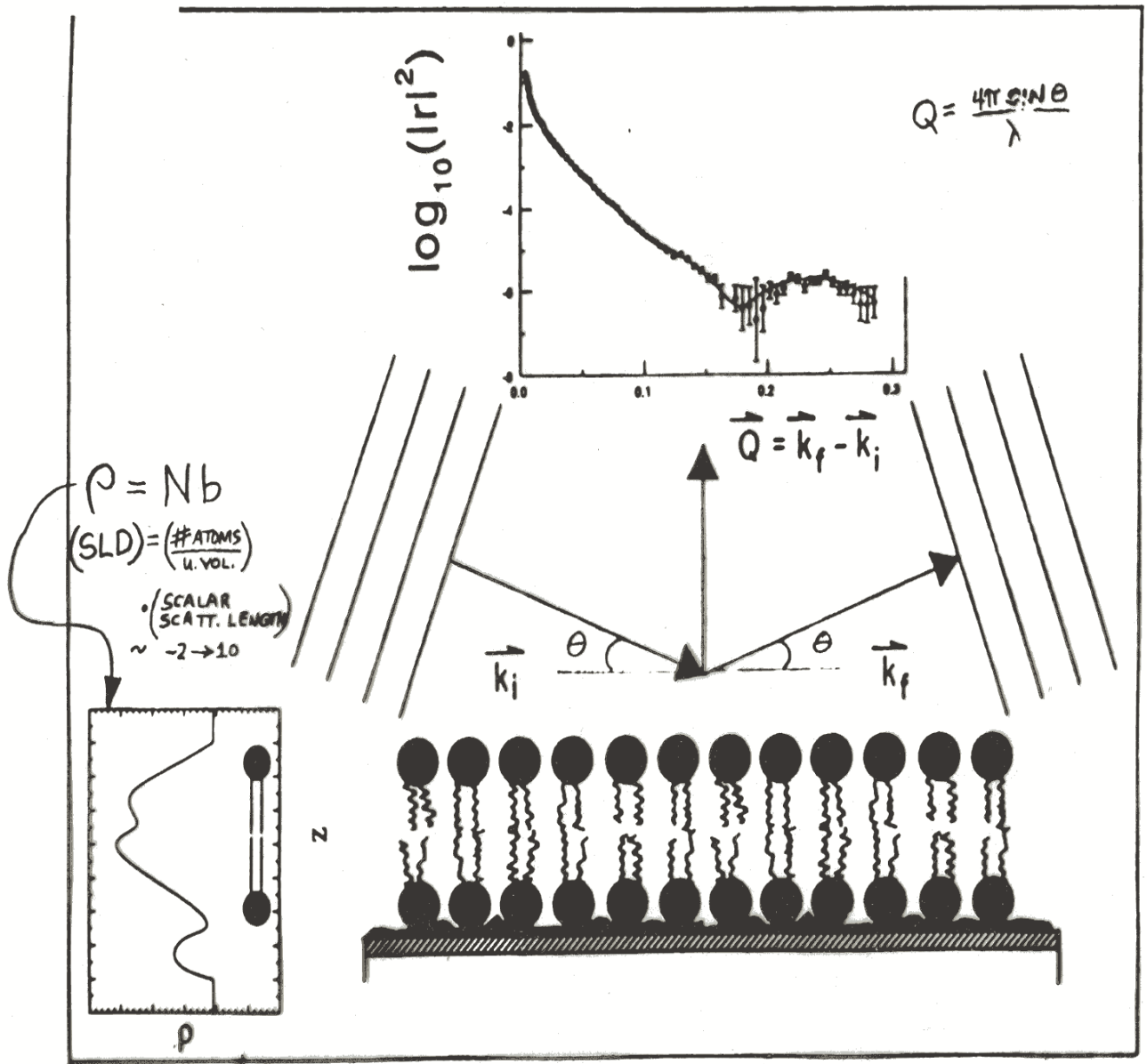
$$\theta_r = \theta$$



Specular reflection: $\bar{\rho}(z) = \langle \rho(x, y, z) \rangle_{xy}$

Non-Specular reflection: $\Delta\rho(x, y, z) = \rho(x, y, z) - \bar{\rho}(z)$

(AFTER N.F. BERK ET AL.)



Overview of the specular reflection method to determine the scattering length density (SLD) depth profile along the mean normal to the surface. The reflectivity (reflected intensity / incident intensity) $|r|^2$ is measured as a function of wavevector transfer Q . $|r(Q)|^2$ can then be fit to a model of the SLD profile from which the corresponding chemical composition depth profile can be inferred. Note that the SLD obtained in this manner corresponds to the in-plane average value (i.e., the plane perpendicular to Q).

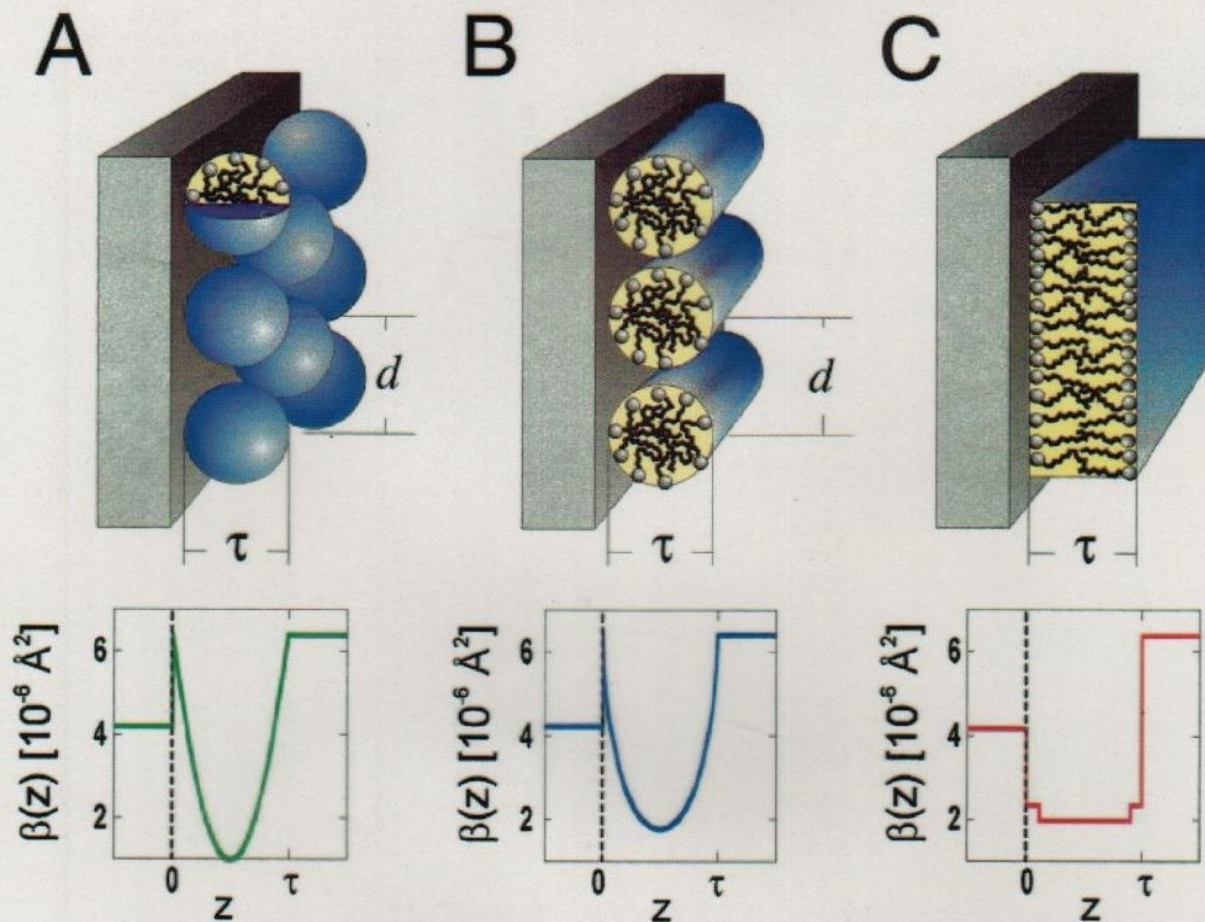


FIG. 1. (Color) Schematic diagram of adsorbed layer structures consisting of (A) spherical micelles, (B) cylindrical micelles, and (C) a bilayer, including the film thickness τ and interaggregate spacing d . Also shown are examples of neutron scattering length density profiles normal to the interface, $\beta(z)$, corresponding to each structure at the quartz/D₂O interface at a fractional surface coverage of 0.55. The head-group and alkyl tails of the surfactants have different scattering length densities, but because of the arrangement of the molecules this is only apparent in the bilayer $\beta(z)$.

single-crystal quartz block and reflected from the quartz-solution interface were recorded as a function of angle of incidence. The off-specular background, including any signal due to scattering from the bulk solution [15], was subtracted to give the reflection coefficient of the surfactant-coated interface. All solutions used were above their critical micelle

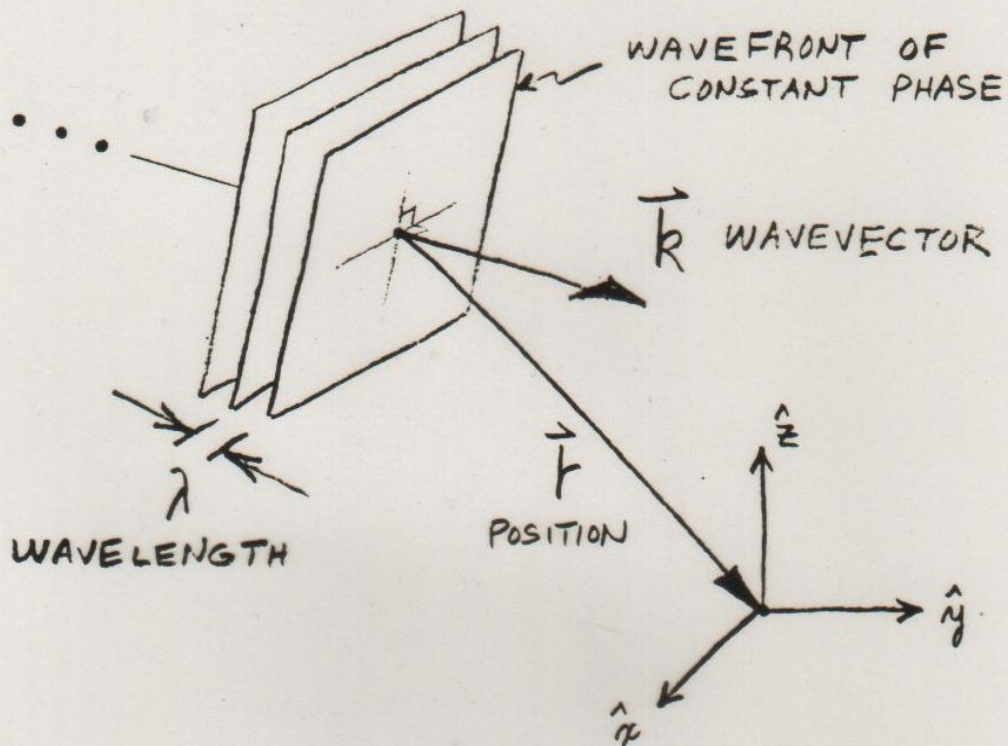
or aggregation concentration, a condition which leads to a saturated adsorbed film at the solid-solution interface.

The cationic surfactant tetradecyltrimethylammonium bromide (TTAB) forms nearly spherical micellar aggregates consisting of approximately 80 molecules in bulk solution. Small angle neutron-scattering measurements [16] give mi-



FIG. 2. 200×200-nm² AFM tip deflection images of (A) spherical TTAB aggregates adsorbed onto quartz from water solution, (B) cylindrical TTAB aggregates adsorbed onto quartz from an aqueous 200mM NaBr solution, and (C) planar DDAB bilayer adsorbed onto quartz from water solution. Long-wavelength undulations visible in (B) and (C) arise from roughness in the underlying quartz.

THE NEUTRON AS A PLANE WAVE PROPAGATING IN FREE SPACE



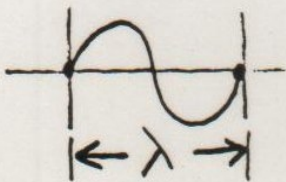
WAVEFUNCTION

$$\Psi \propto e^{i \vec{k}_0 \cdot \vec{r}}$$

$$\begin{cases} \vec{k}_0 = k_{0x} \hat{x} + k_{0y} \hat{y} + k_{0z} \hat{z} \\ \vec{r} = x \hat{x} + y \hat{y} + z \hat{z} \end{cases}$$

FOR \vec{k}_0 ALONG \hat{z} , FOR EXAMPLE,

$$\Psi \propto \cos(k_{0z} z) + i \sin(k_{0z} z)$$



$$= \left(\frac{2\pi}{\lambda} z \right)$$

$|\Psi|^2 \propto$ PROBABILITY OF THE NEUTRON BEING THERE

FOR ELASTIC INTERACTIONS
TOTAL ENERGY OF THE
NEUTRON IS CONSTANT

$$\begin{aligned}\text{TOTAL ENERGY} &= \text{KINETIC ENERGY} \\ &+ \text{POTENTIAL ENERGY} \\ &= \text{CONSTANT}\end{aligned}$$

WAVE EQUATION OF MOTION
(SCHRÖDINGER EQUATION)

$$\underbrace{\left[\frac{-\hbar^2}{2m} \nabla^2 \right]}_{\text{K.E.}} + \underbrace{V(\vec{r})}_{\text{P.E.}} = \underbrace{E}_{\text{T.E.}} \Psi$$

$$\nabla^2 = \frac{\partial^2}{\partial x^2} + \frac{\partial^2}{\partial y^2} + \frac{\partial^2}{\partial z^2}$$

IN VACUUM

$$\text{K.E.}_0 = \frac{\hbar^2 k_0^2}{2m}$$

IN THE CONTINUUM LIMIT

$$V(\vec{r}) = \frac{2\pi\hbar^2}{m} \sum_{j=1} N_j b_j = \frac{2\pi\hbar^2}{m} \rho$$

NUMBER OF ATOMS
OF TYPE j PER UNIT
VOLUME

SCATTERING LENGTH
DENSITY (SLD)

COHERENT
SCATTERING LENGTH
OF ATOM j —

$$b = \underbrace{\text{Re}b}_{\text{SCATTERING}} + i \underbrace{\text{Im}b}_{\text{ABSORPTION}}$$

IN VACUUM

$$E_0 = \frac{\hbar^2 k_0^2}{2m} + 0$$

IN A MATERIAL MEDIUM

$$E = \frac{\hbar^2 k^2}{2m} + \frac{2\pi\hbar^2}{m} \rho$$

CONSERVATION OF ENERGY REQUIRES $E_0 = E$
SO THAT

$$k^2 = k_0^2 - 4\pi\rho$$

∴ THEREFORE

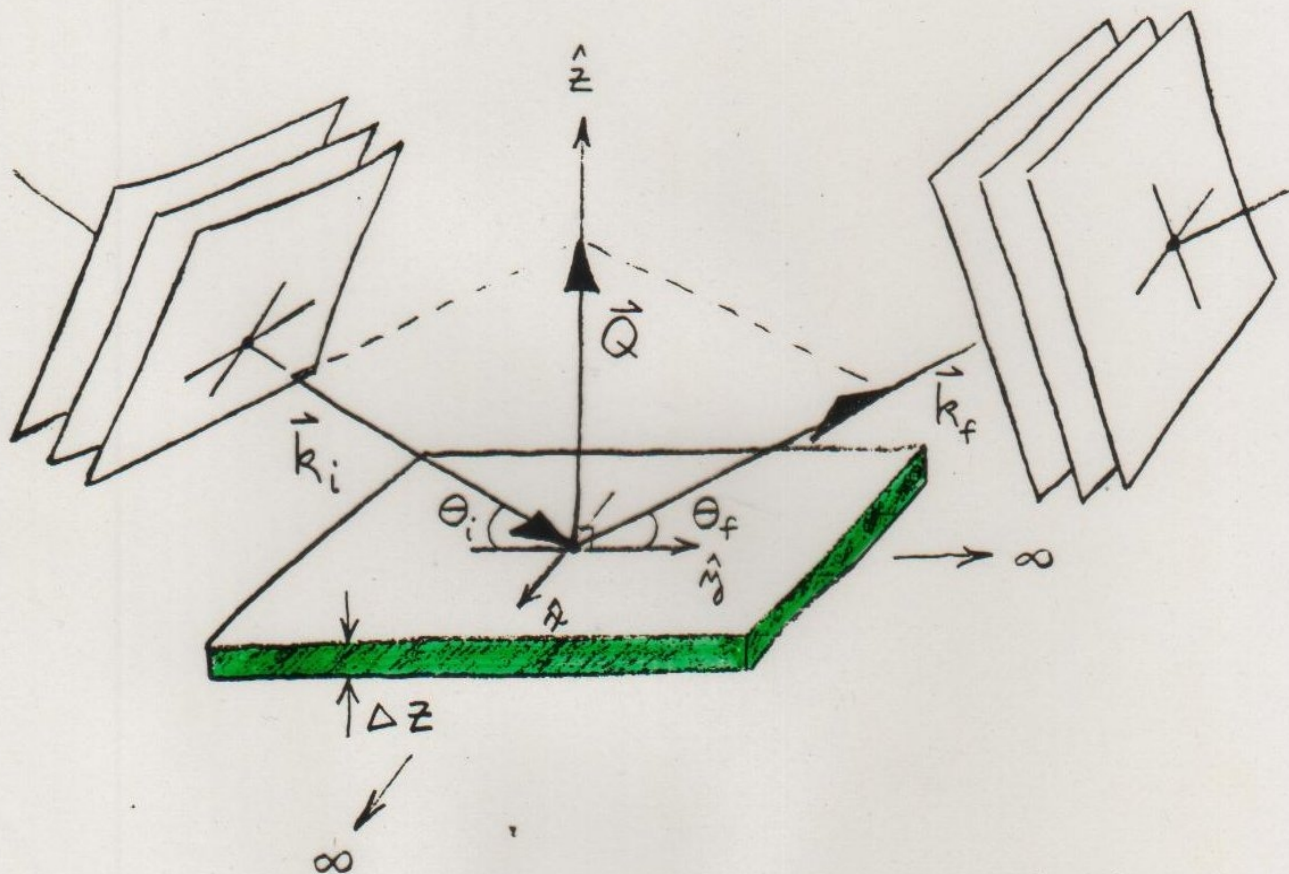
$$[\nabla^2 + k^2] \Psi = 0$$

CAN THEN DEFINE A REFRACTIVE INDEX $n \equiv \frac{k}{k_0}$

OR

$$n^2 = 1 - \frac{4\pi\rho}{k_0^2}$$

REFLECTION FROM AN IDEAL FILM OR SLAB OF MATERIAL



WAVEVECTOR TRANSFER $\vec{Q} = \vec{k}_f - \vec{k}_i$

$\rho = \rho(z)$ ONLY

EXPANDING $k^2 = k_0^2 - 4\pi\rho$,

$$k_x^2 + k_y^2 + k_z^2 + 4\pi\rho = k_{0x}^2 + k_{0y}^2 + k_{0z}^2.$$

NOW IF $\rho = \rho(z)$ ONLY, THEN

$$\frac{\partial \rho}{\partial x} \text{ AND } \frac{\partial \rho}{\partial y}, \text{ WHICH ARE}$$

PROPORTIONAL TO THE GRADIENTS OF THE POTENTIAL OR FORCES IN THE RESPECTIVE DIRECTIONS, ARE EQUAL TO ZERO. THUS, NO FORCE ACTS ALONG THESE DIRECTIONS TO CHANGE k_x AND k_y . THEN

$$k_x = k_{0x} \text{ AND } k_y = k_{0y} \text{ ARE}$$

"CONSTANTS OF THE MOTION".

SUBSTITUTING $\underline{\Psi}(\vec{r}) = e^{ik_{0x}x} e^{ik_{0y}y} \underline{\Psi}(z)$

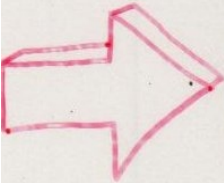
INTO $[\nabla^2 + k^2] \underline{\Psi} = 0$ GIVES

$$\left[\frac{\partial^2}{\partial z^2} + k_z^2 \right] \underline{\Psi}(z) = 0$$

$$\text{AND } \therefore k_z^2 = k_{0z}^2 - 4\pi\rho(z).$$

BECAUSE THERE IS NO CHANGE IN THE POTENTIAL IN THE X- OR Y- DIRECTIONS, THERE CAN BE NO MOMENTUM CHANGE IN THESE DIRECTIONS EITHER

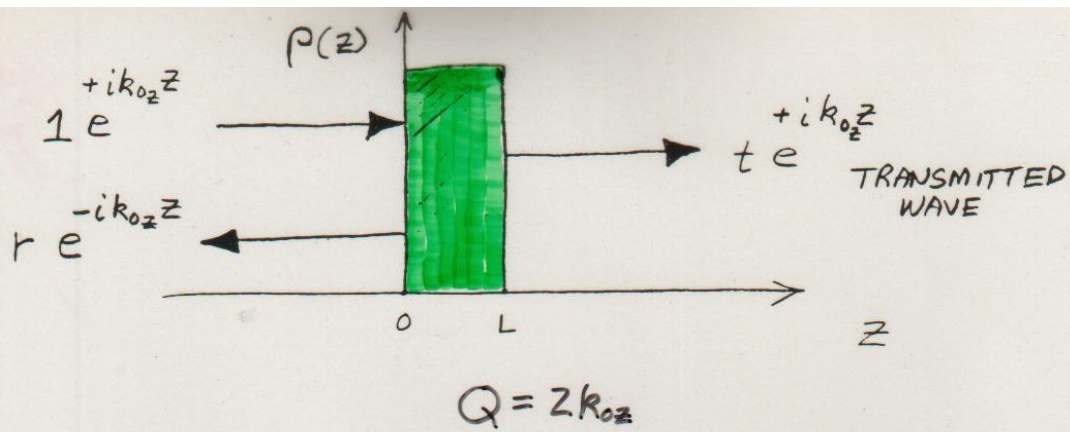
THE IDEAL SLAB GEOMETRY WITH $\rho = \rho(z)$ ONLY GIVES RISE TO THE COHERENT "SPECULAR" REFLECTION OF A PLANE WAVE WHICH IS DESCRIBED BY A ONE-DIMENSIONAL WAVE EQUATION:


$$\left[\frac{\partial^2}{\partial z^2} + k_{0z}^2 - 4\pi\rho(z) \right] \psi(z) = 0$$

IN THIS CASE $\theta_i = \theta_f \equiv \theta$,

$$|\vec{k}_i| = |\vec{k}_f| \quad \text{AND} \quad Q = 2k \sin\theta \\ = 2k_z$$

$$\text{ALSO, } \eta_z^2 \equiv 1 - \frac{4\pi\rho(z)}{k_{0z}^2}$$



FROM THE WAVE EQUATION,
IT IS POSSIBLE TO FIND
A SOLUTION FOR THE
REFLECTION AMPLITUDE IN
INTEGRAL FORM
(SEE ARTICLE PAGES) :

$$r(Q) = \frac{4\pi}{iQ} \int_{-\infty}^{+\infty} \psi(z) p(z) e^{+ik_{0z}z} dz$$

WHAT IS LOCALIZED AT z IN
THE SLD PROFILE $p(z)$ IN
"REAL" SPACE, IS DISTRIBUTED
OVER THE REFLECTION AMPLITUDE
 $r(Q)$ IN THE RELATED SCATTERING
OR "RECIPROCAL" SPACE

(Note: "article pages" are reproduced in the Appendix.)

$\psi(z)$ INSIDE THE MEDIUM
IS GENERALLY UNKNOWN:

BORN APPROXIMATION REPLACES
 $\psi(z)$ WITH THE INCIDENT
WAVE FUNCTION e^{+ik_0z} BASED
ON THE ASSUMPTION THAT
 $\psi(z)$ IS NOT SIGNIFICANTLY
DISTORTED FROM THE FREE
SPACE FORM (WEAK
INTERACTION): THEN

$$r(Q) \approx \frac{4\pi}{iQ} \int_{-\infty}^{+\infty} p(z) e^{iQz} dz$$

FOURIER
TRANSFORM

FOR A REAL POTENTIAL $p(z)$

$$\text{Re } r(Q) \approx \frac{4\pi}{Q} \int_{-\infty}^{+\infty} p(z) \sin(Qz) dz$$

IF ρ IS NOT EXACTLY $\rho(z)$,
 I.E., SOME VARIATIONS EXIST IN
 THE (x, y) -PLANE, THEN

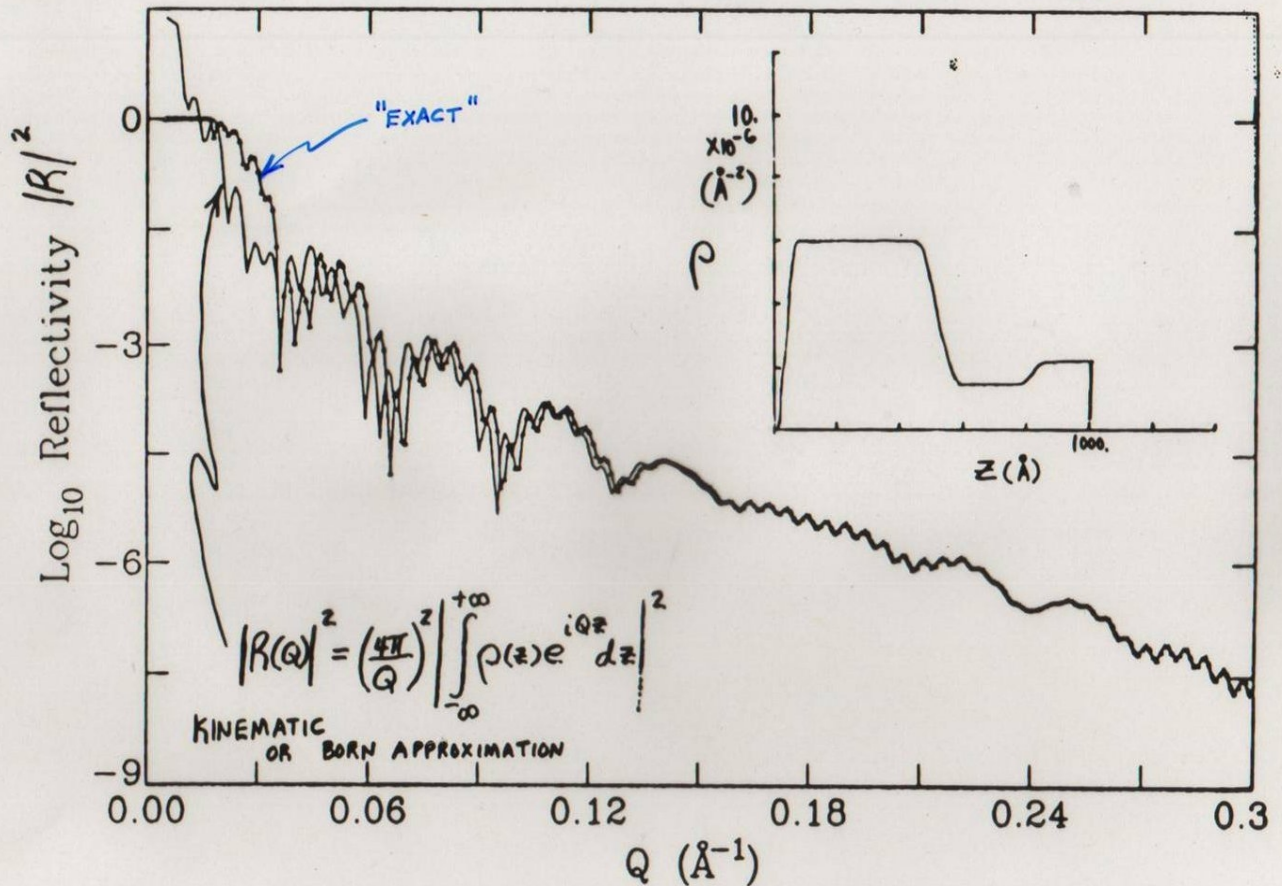
$r_{\text{BORN}} \approx \frac{4\pi}{iQ} \int_{-\infty}^{+\infty} \langle \rho(x, y, z) \rangle_{x, y} e^{iQz} dz$
 ON SPECULAR
 "RIDGE"
 WHERE $\vec{Q} = Q_z \hat{z}$

WHERE

$$\langle \rho(x, y, z) \rangle_{x, y} = \frac{1}{A} \iint_{-\infty}^{+\infty} \rho(x, y, z) dx dy = \bar{\rho}(z) \text{ ONLY}$$

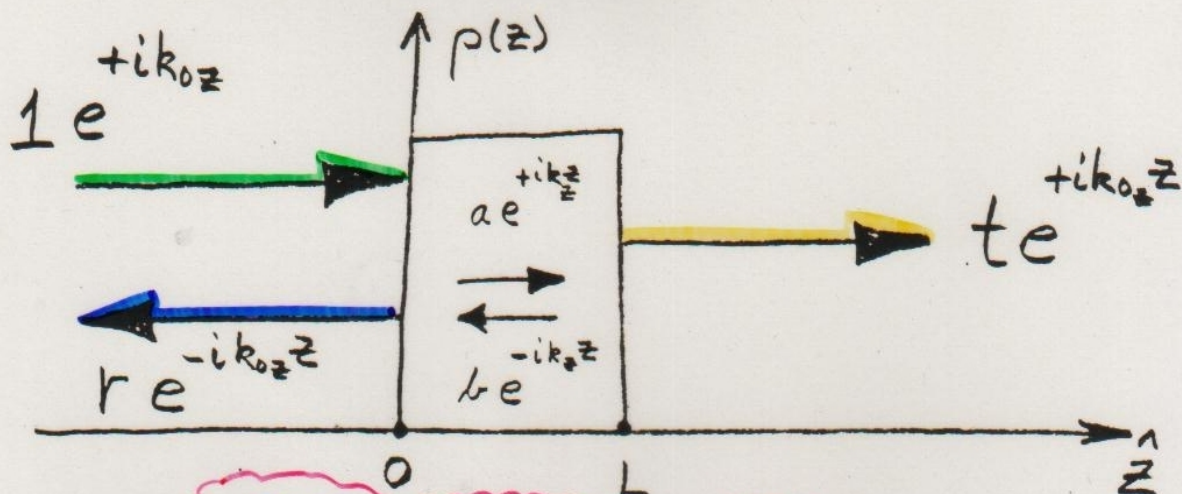
$\& \bar{A} =$ NORMALIZING AREA OF
 THE (x, y) -PLANE

PROBLEM: BORN APPROXIMATION FAILS AT SUFFICIENTLY SMALL Q — MUST THEN USE EXACT THEORY



Comparison between kinematic (line) and dynamic (triangle + line) plus-state reflectivities for a density profile similar to that of Fig.2 as described in the text.

Because the Born approximation often fails to be of sufficient accuracy for specular reflection at at low Q, an exact solution of the one-dimensional Schroedinger wave equation of motion becomes necessary. A practical method of solving this equation is possible, by imposing certain boundary conditions in piece-wise continuous fashion.

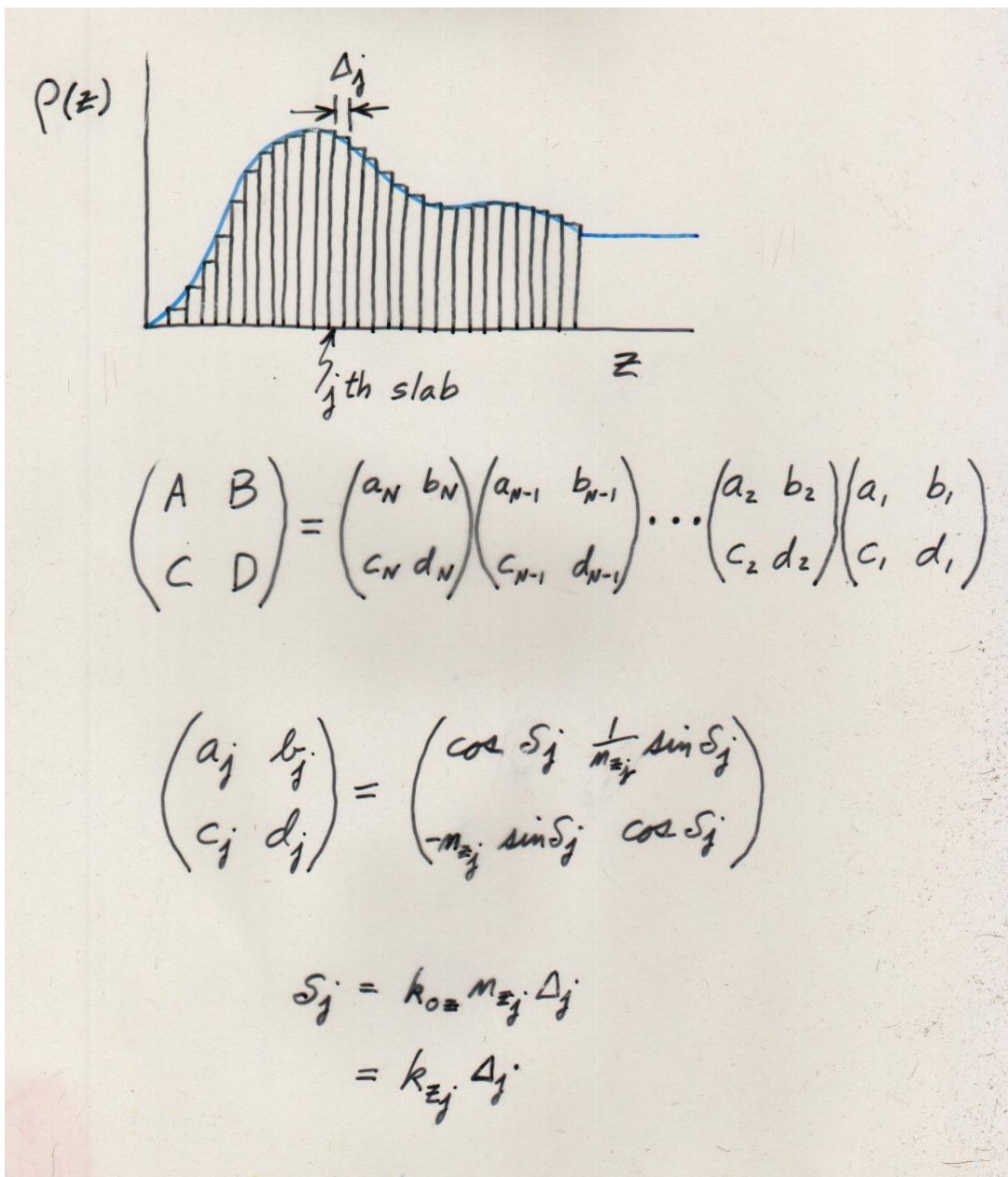


$$\frac{\partial^2 \psi(z)}{\partial z^2} + k_z^2 \psi(z) = 0$$

CONSERVATION OF MOMENTUM
AND PARTICLE NUMBER
REQUIRE THAT $\frac{\partial \psi(z)}{\partial z}$ AND $\psi(z)$

BE CONTINUOUS AT THE
BOUNDARIES $z=0$ & $z=L$

$$\begin{pmatrix} t \\ it \end{pmatrix} e^{ik_0zL} = \begin{pmatrix} A & B \\ C & D \end{pmatrix} \begin{pmatrix} 1+r \\ i(1-r) \end{pmatrix}$$



The elements A, B, C, and D of the so-called “transfer” matrix which relates the reflection, transmission, and incident wave amplitudes -- r, t, and 1, respectively -- contain all of the information about the SLD composition of the film. The transfer matrix can be constructed of a product of matrices, each of which corresponds to one successive “slice” of the film over which the SLD is taken to be a constant value. Thus, any arbitrary profile can be rendered -- and to whatever spatial resolution is needed by making the thicknesses of the slices small enough.

free film

Then, once we know $M_k(L)$:

$$\boxed{z=L}$$

$$\boxed{z=0}$$

$$\begin{pmatrix} 1 \\ i \end{pmatrix} t(k) e^{ikL} = \begin{pmatrix} A_k(L) & B_k(L) \\ C_k(L) & D_k(L) \end{pmatrix} \begin{pmatrix} 1+r(k) \\ i[1-r(k)] \end{pmatrix}$$

$$\boxed{r = \frac{B+C + i(D-A)}{B-C + i(D+A)}}$$

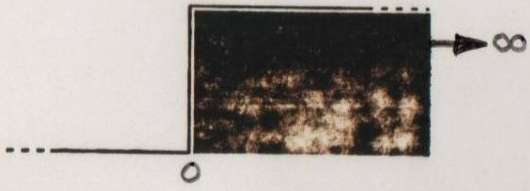
$$t = \frac{2ie^{-ikL}}{B-C + i(D+A)}$$

$$R = |r|^2 = \frac{\Sigma-2}{\Sigma+2}, \quad \Sigma = A^2 + B^2 + C^2 + D^2$$

(Courtesy of Norm Berk)

Here r and t are written in terms of the transfer matrix elements A , B , C , and D .

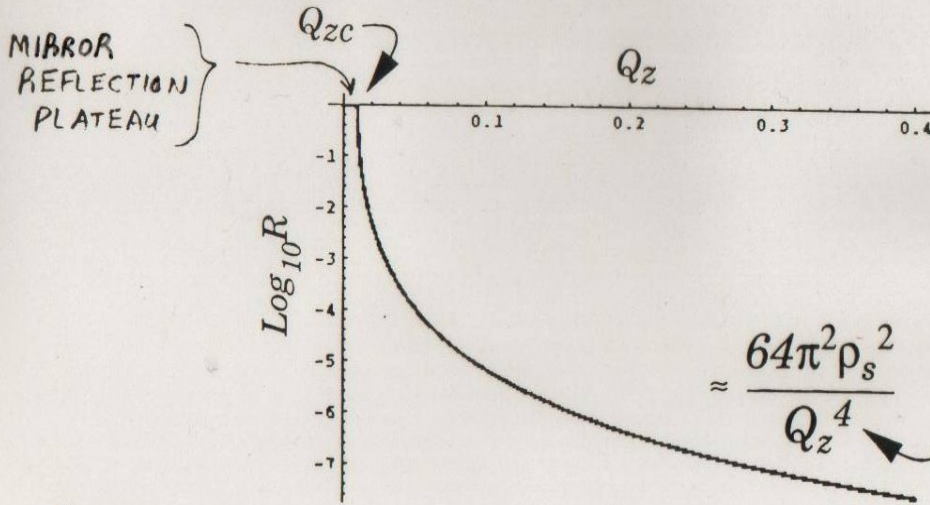
Fresnel Reflectivity



$$|r_F|^2 \equiv R_F(Q_z)$$

$$R_F(Q_z) = \frac{1 - \sqrt{1 - \frac{Q_{zc}^2}{Q^2}}}{1 + \sqrt{1 - \frac{Q_{zc}^2}{Q^2}}}$$

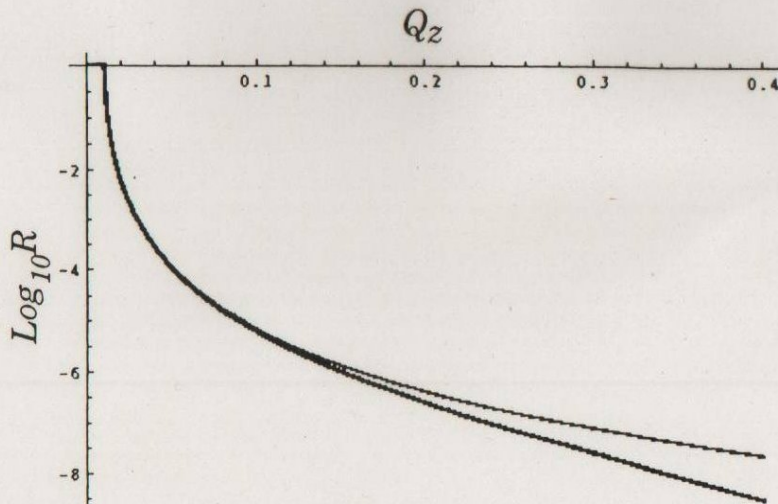
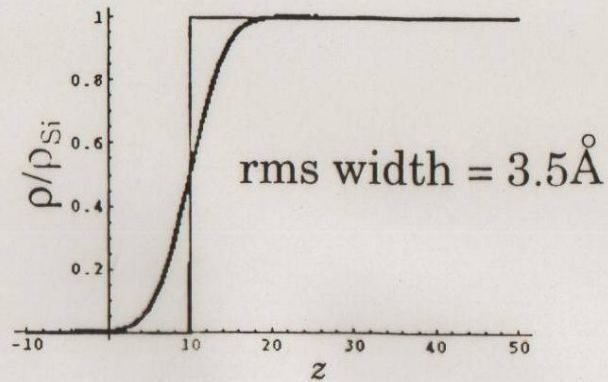
For $Q_z < Q_{zc}$, $R_F = 1$.



$$Q_{zc} = \text{SQRT}(16 * \pi * \rho) \text{ (Courtesy of Norm Berk)}$$

"Soft" substrate

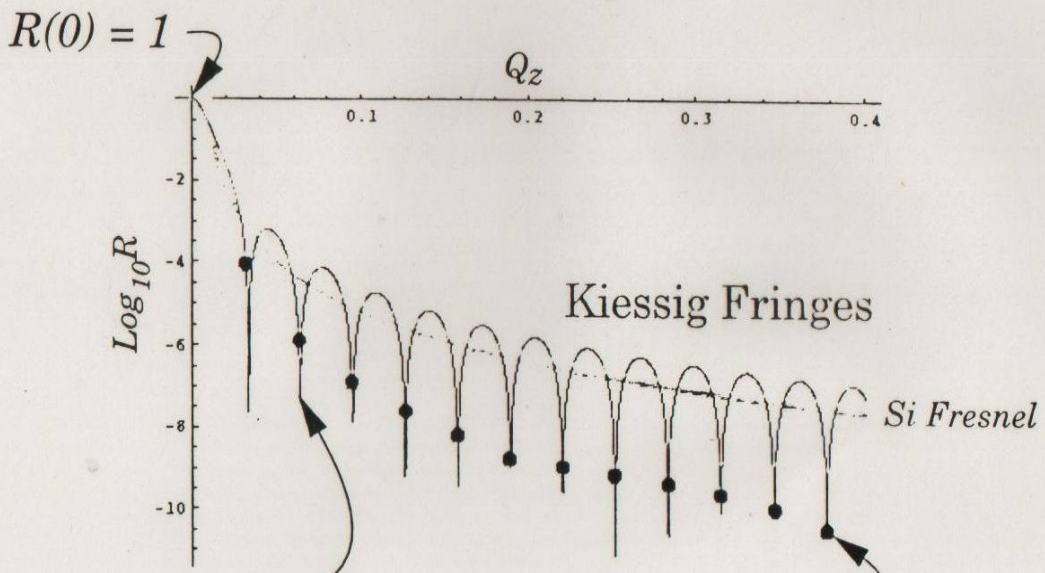
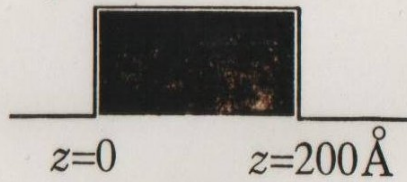
Smooth transition:
interlayer diffusion
roughness



For an interface that is not perfectly "sharp", the reflectivity falls off with increasing Q faster than $1/(Q^4)$.

Uniform slab

$$\rho = 2.07 \cdot 10^{-6} \text{ \AA}^{-2}$$



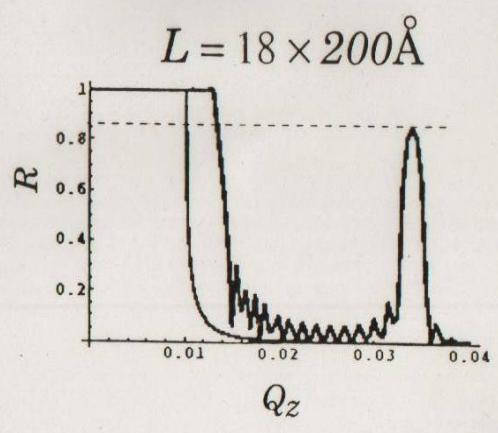
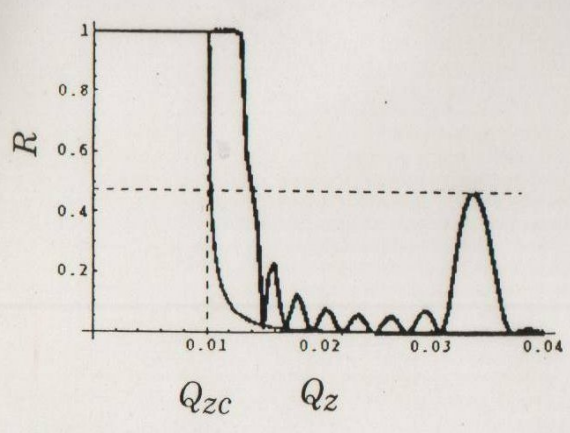
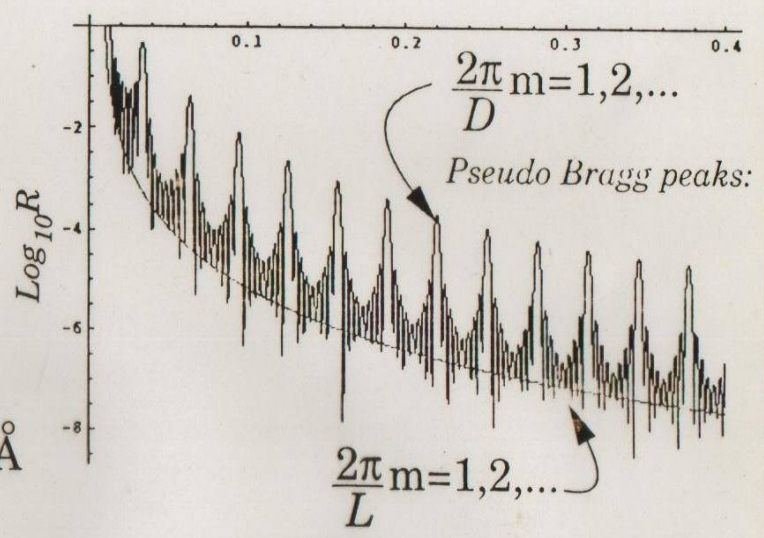
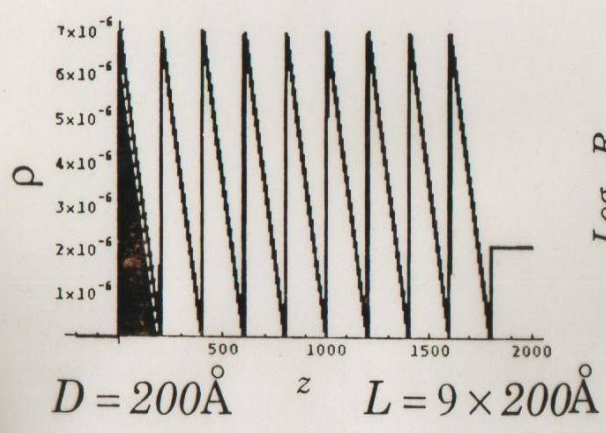
$$\sqrt{Q_z^2 - 16\pi\rho} = \frac{2\pi}{L} m = 1, 2, \dots$$

$$\frac{2\pi}{L} m = 1, 2, \dots$$

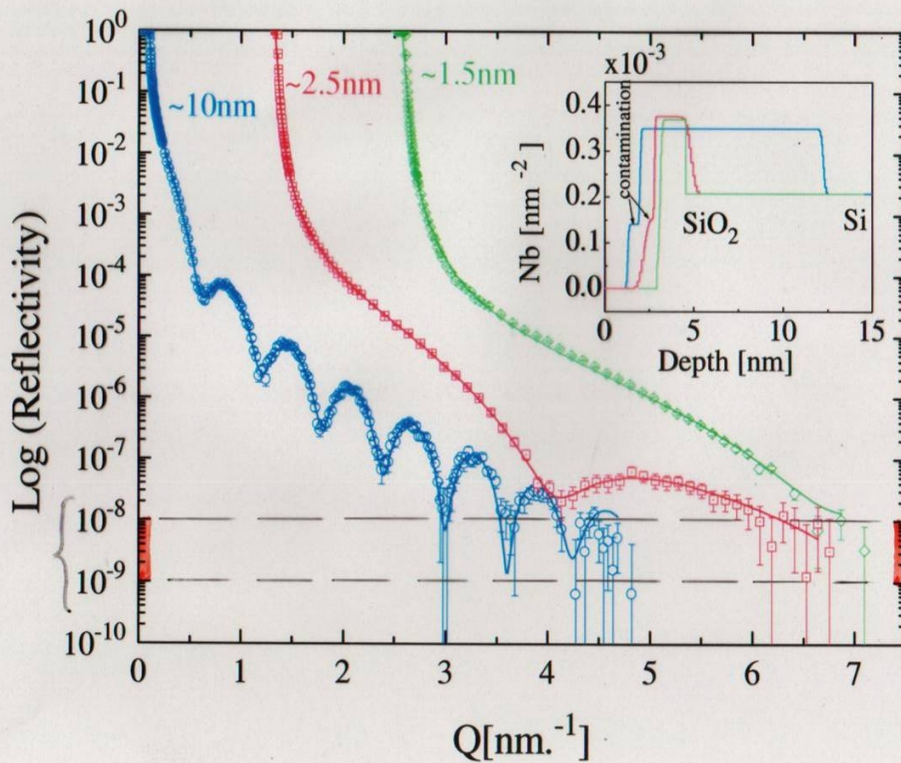
(Kinematical)

(N.F. BERK)

Multilayer on Si

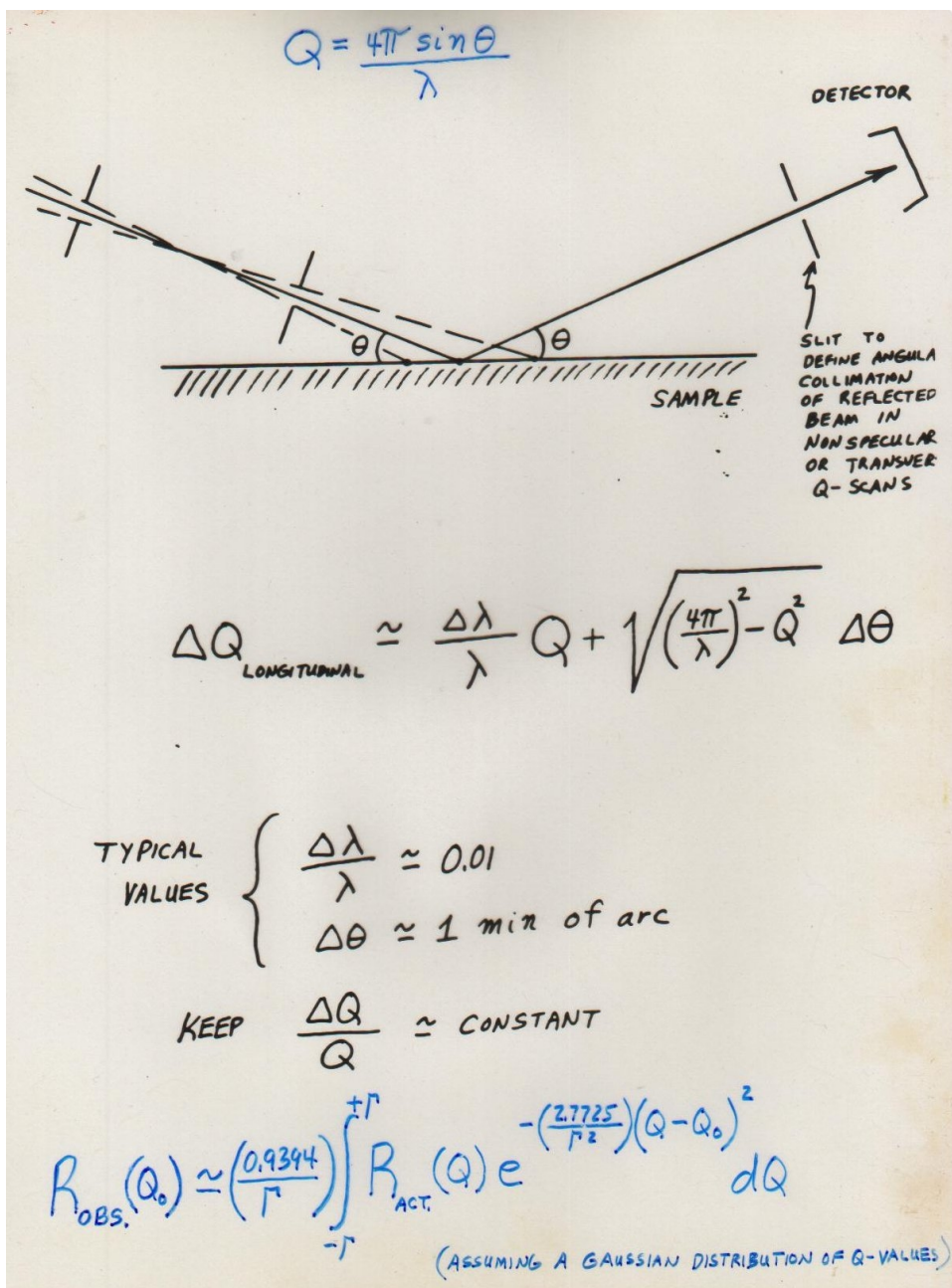


(M.F.BERK)

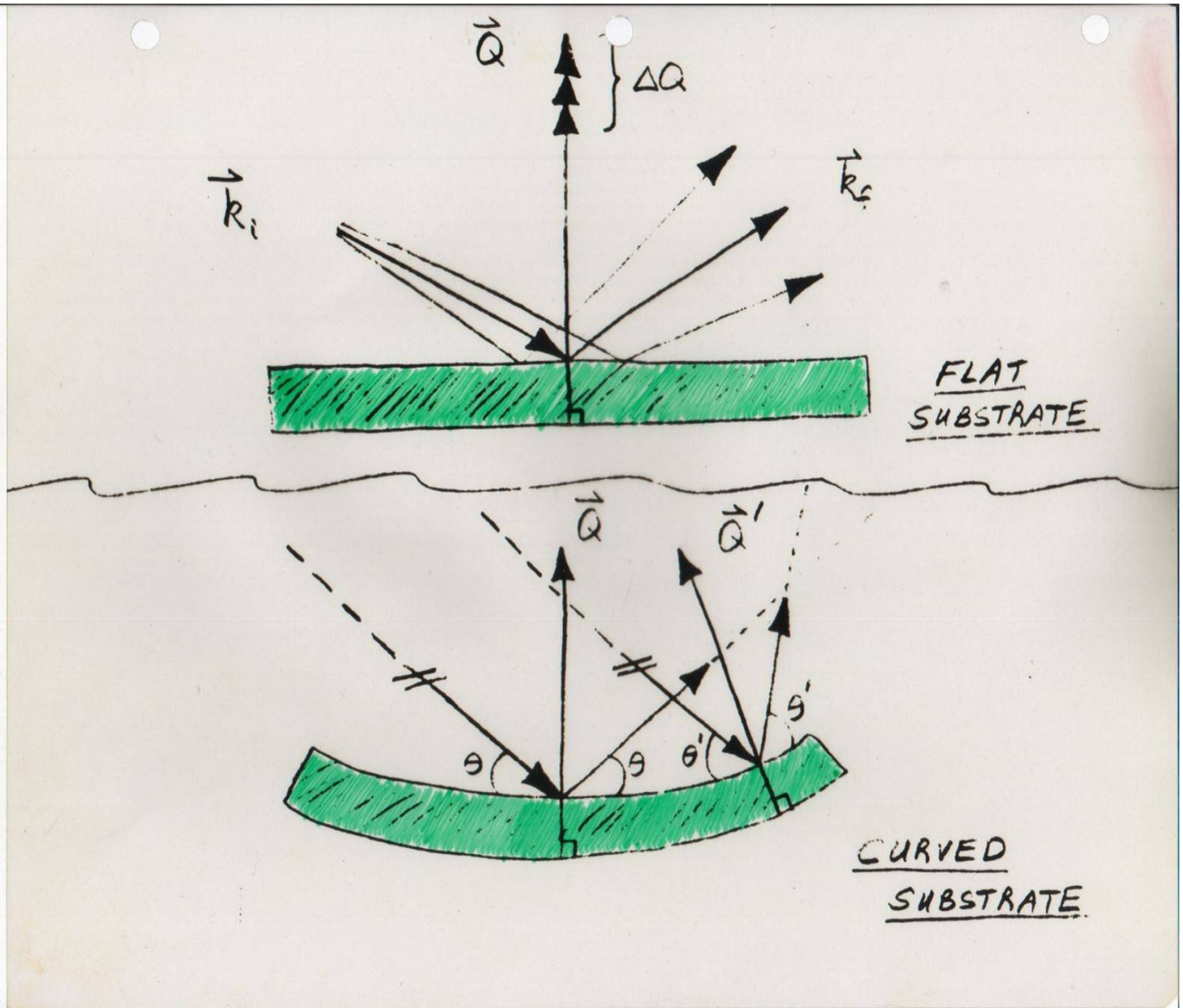


J. DURA et al.

This neutron specular reflectivity data shows that the reflectivity can be measured over a range of up to 8 orders of magnitude out to a maximum Q of 5 inverse nanometers with a spatial resolution of a fraction of a nanometer -- under certain conditions.

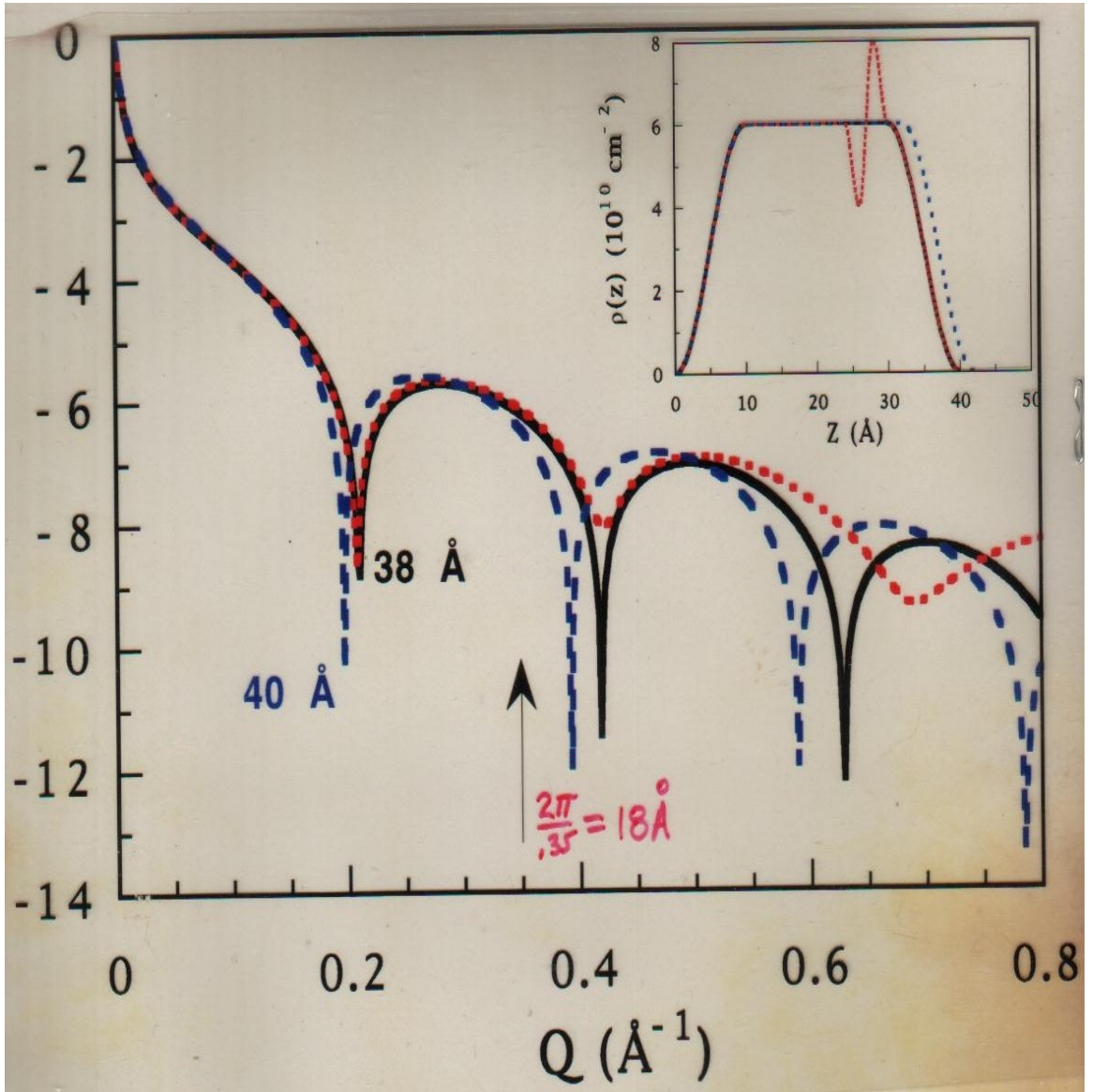


The incoherent instrumental beam resolution of the reflectometer which describes the distribution of directions and magnitudes of mean wavevectors, each of which is associated with an individual neutron wave packet in the collection that make up a beam, is convoluted with the actual reflectivity corresponding to the film sample. This convolution must be taken into account in analyzing the measured reflectivity in terms of a model SLD profile. ($R = |r|^2$.)



In addition to the guides, apertures, monochromator and source itself, the curvature of the substrate on which the sample film is deposited contributes to the incoherent instrumental beam resolution. The flatter the substrate, the smaller this contribution.

$\log_{10}(\text{reflectivity})$



Solid, long-dash, and short-dash neutron reflectivity curves corresponding to their respective scattering length density profiles shown in the inset. This series of curves and profiles illustrates the sensitivity of the reflectivity to the overall film thickness at reflectivities approaching 10^{-7} whereas detailed features such as the oscillation in the long-dash profile can only be accurately discerned at reflectivities an order of magnitude or so lower, at Q -values corresponding to $2\pi/\text{width of the feature}$.

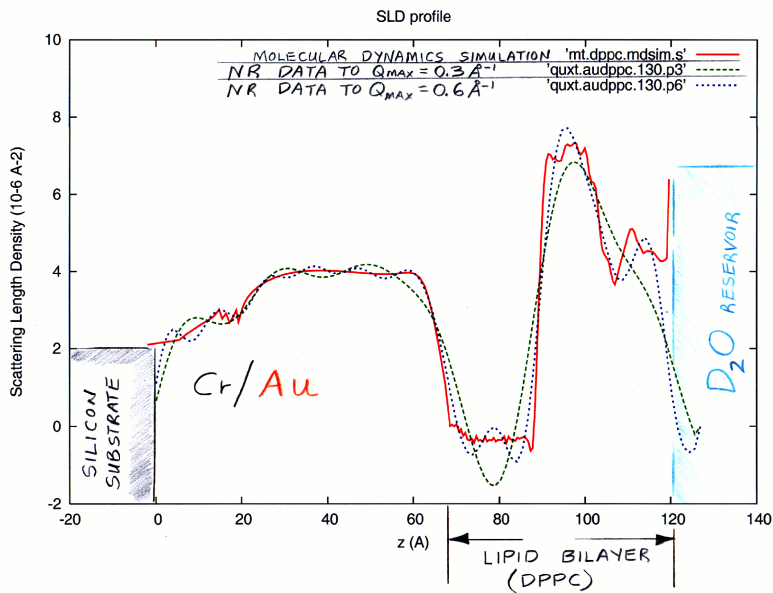
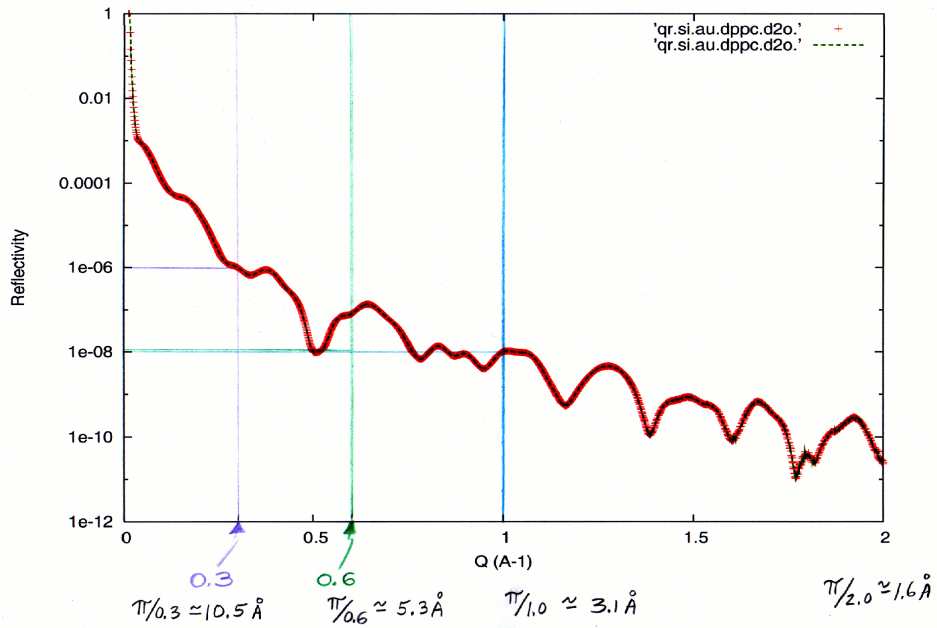
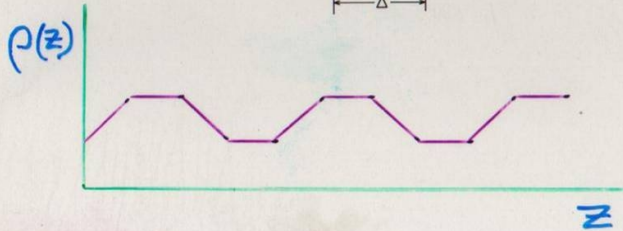
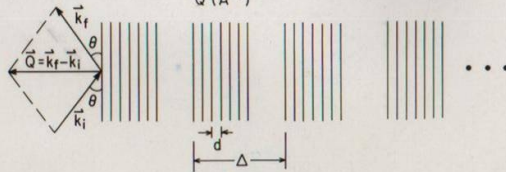
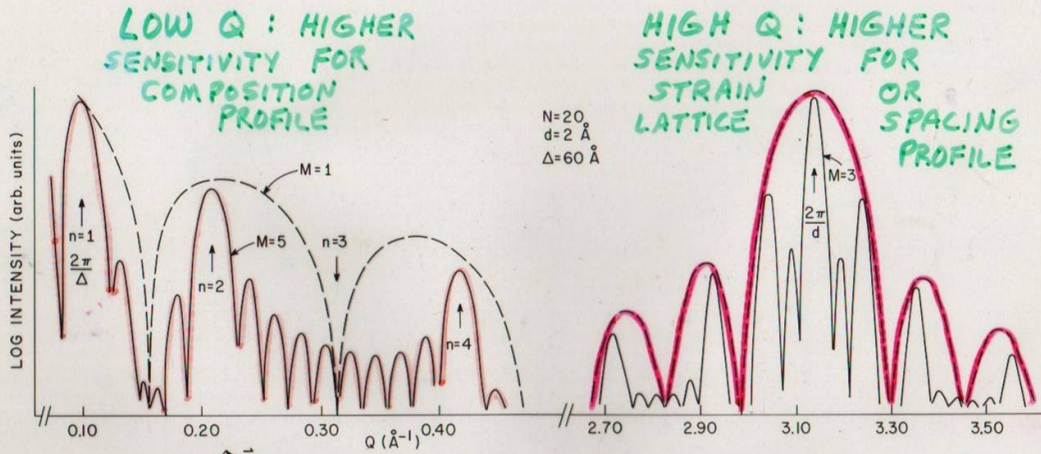


Illustration of the inverse relationship between the maximum value of Q up to which the reflectivity is measured and the spatial resolution in the corresponding SLD depth profile. Resolving smaller features in the profile in real space requires collecting reflectivity data up to larger values of Q in reciprocal space. The statistical accuracy in the measured reflectivity also affects the level of uncertainty in the associated SLD profile model to which the reflectivity data are fit.

"REFLECTIVITY" REGIME

CRYSTAL "DIFFRACTION" REGIME

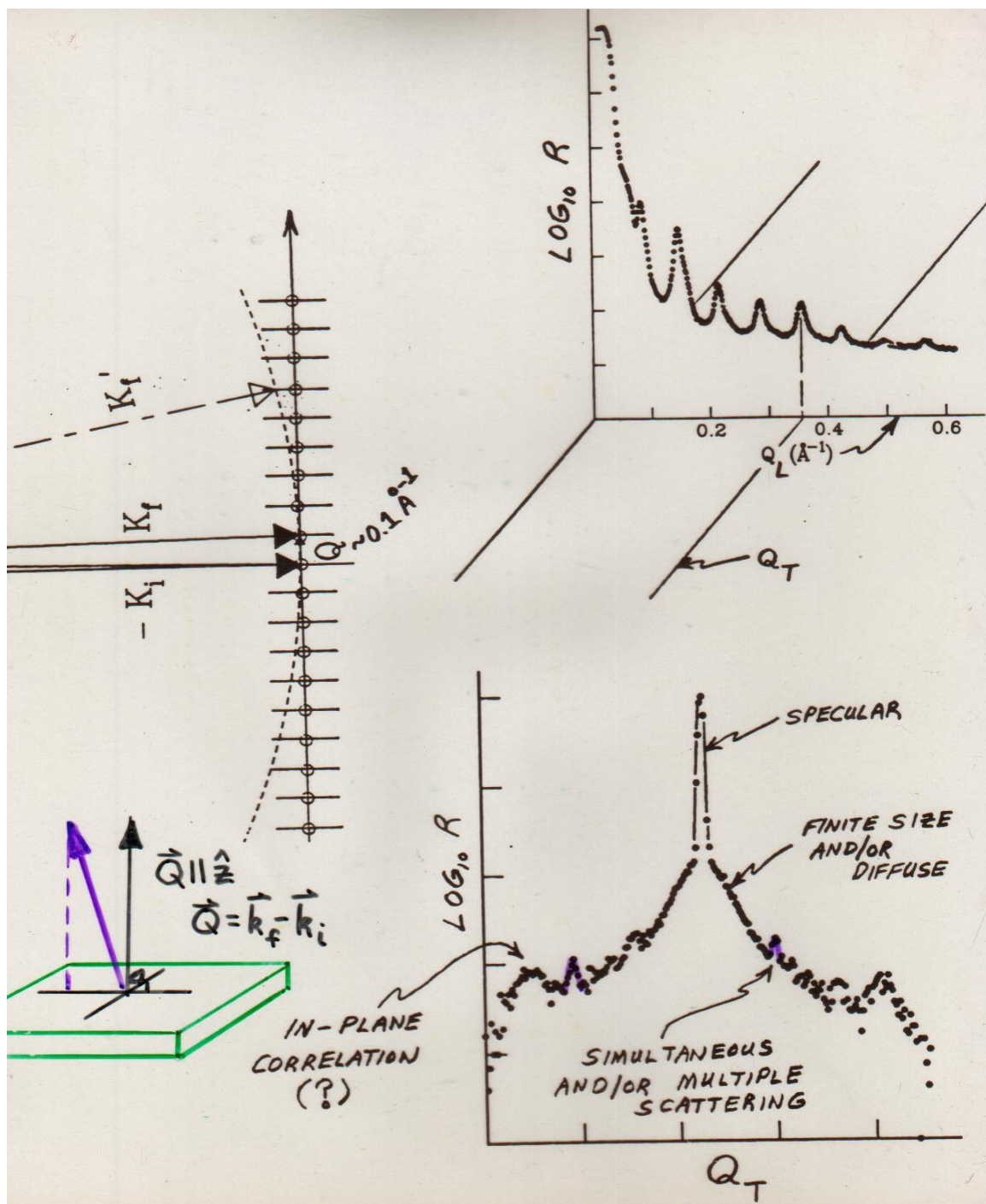


$$|R|_{KN}^2 = \left(\frac{4\pi}{Q}\right)^2 \left| \sum_{m=1}^M \sum_{n=1}^N \rho e^{iQ(md+n\Delta)} \right|^2$$

$$= \left(\frac{4\pi}{Q}\right)^2 \rho^2 \left| \frac{\sin(NQ\Delta/2)}{\sin(Q\Delta/2)} \right|^2 \left| \frac{\sin(MQ/2)}{\sin(Q/2)} \right|^2$$

Specular reflectivity measurements are conventionally taken to mean elastic diffraction over a region of sufficiently low values of Q that sensitivity to structure at inter-atomic length scales is insignificant. Continuing a specular scan to high enough Q eventually allows the interatomic structure of, say, a superlattice to be revealed.

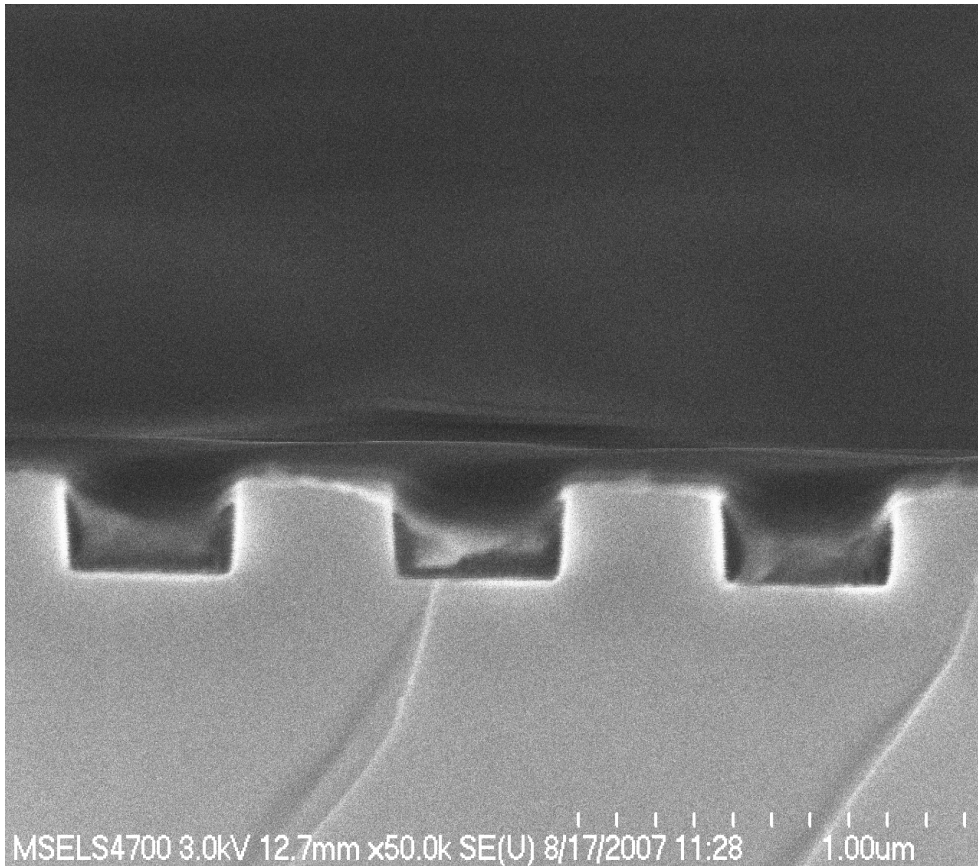
Non-specular reflection



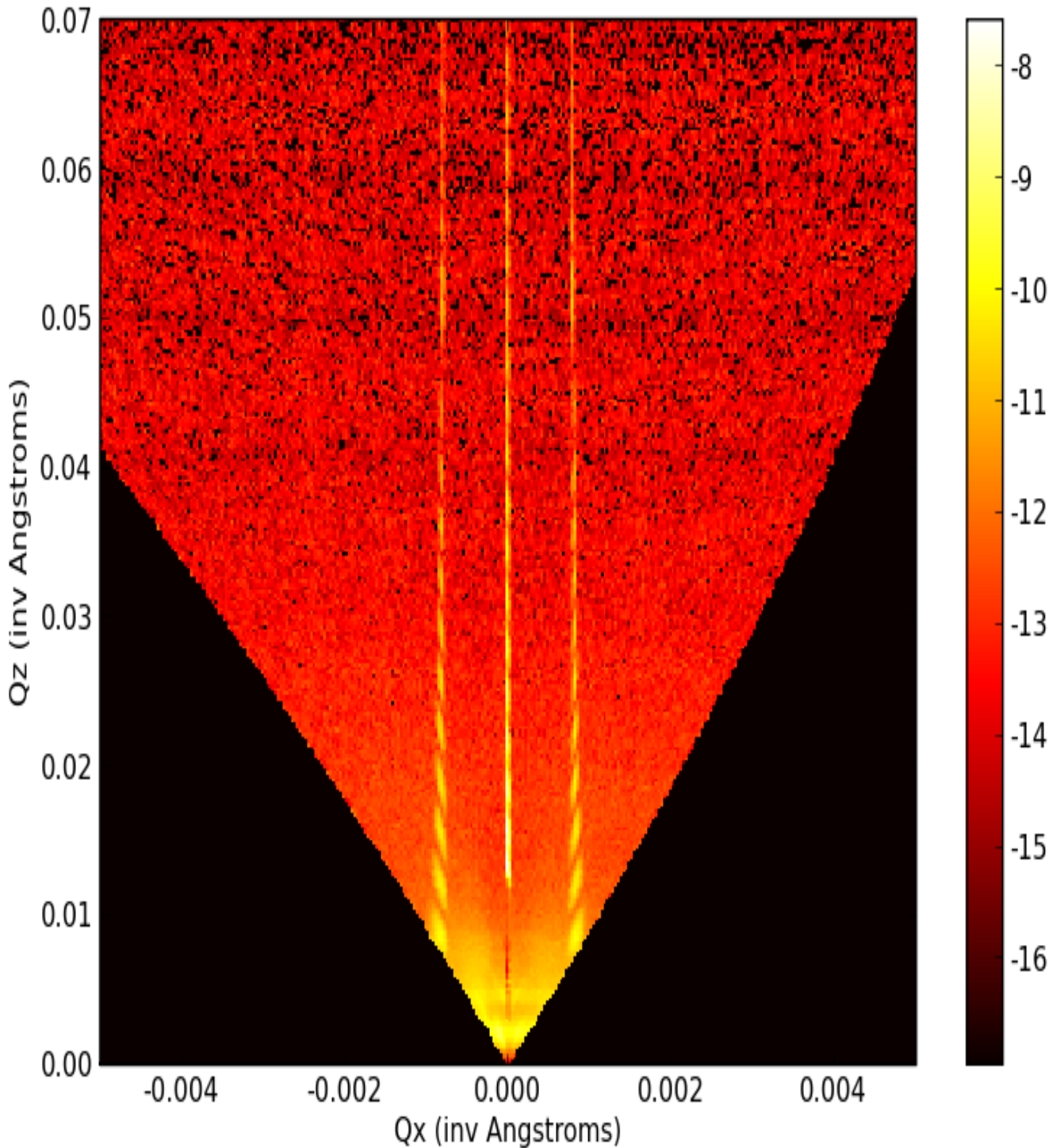
If a scan of reflected intensity is performed with a component of the wavevector transfer Q lying in the plane of the film, then information about *in-plane* variations of the SLD can be obtained.

Diblock copolymer lamellar nanostructures –

R.Jones, B.Berry, and K.Yager (NIST Polymer Division) and
S.Satija, J.Dura, B.Maranville et al. (NCNR).



Side-view scanning-electron micrograph of laser-interferometry-produced silicon substrate with 400 nm channels, spaced by 400 nm for a total repeat distance of 800 nm.



Neutron diffraction from silicon with channels cut in the surface in a periodic grating structure (as shown in the previous slide) without any material in the troughs. Using a position-sensitive-detector, both specular reflectivity (along the vertical Q_z axis) and non-specular (along the horizontal Q_x axis) can be collected.

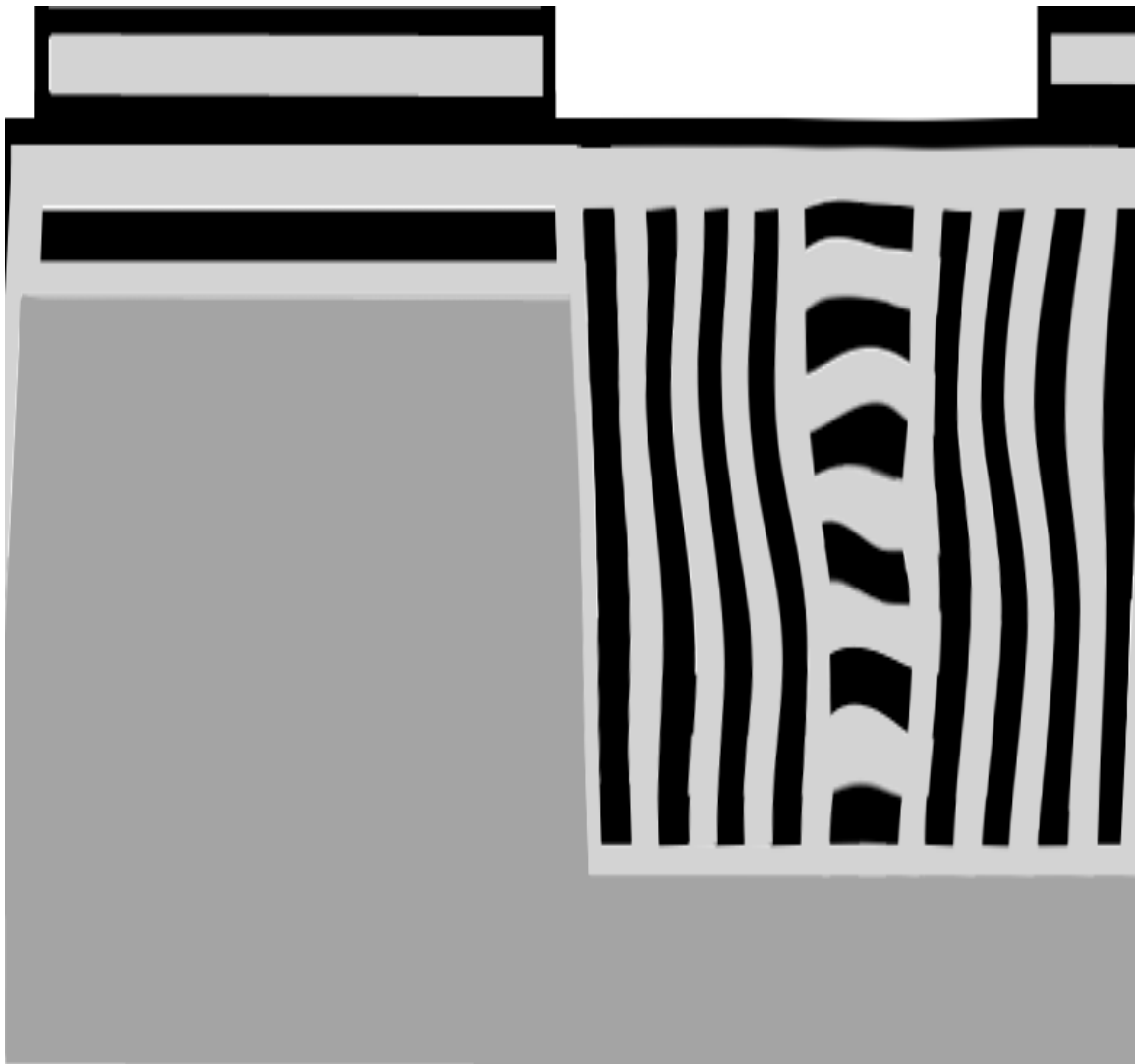
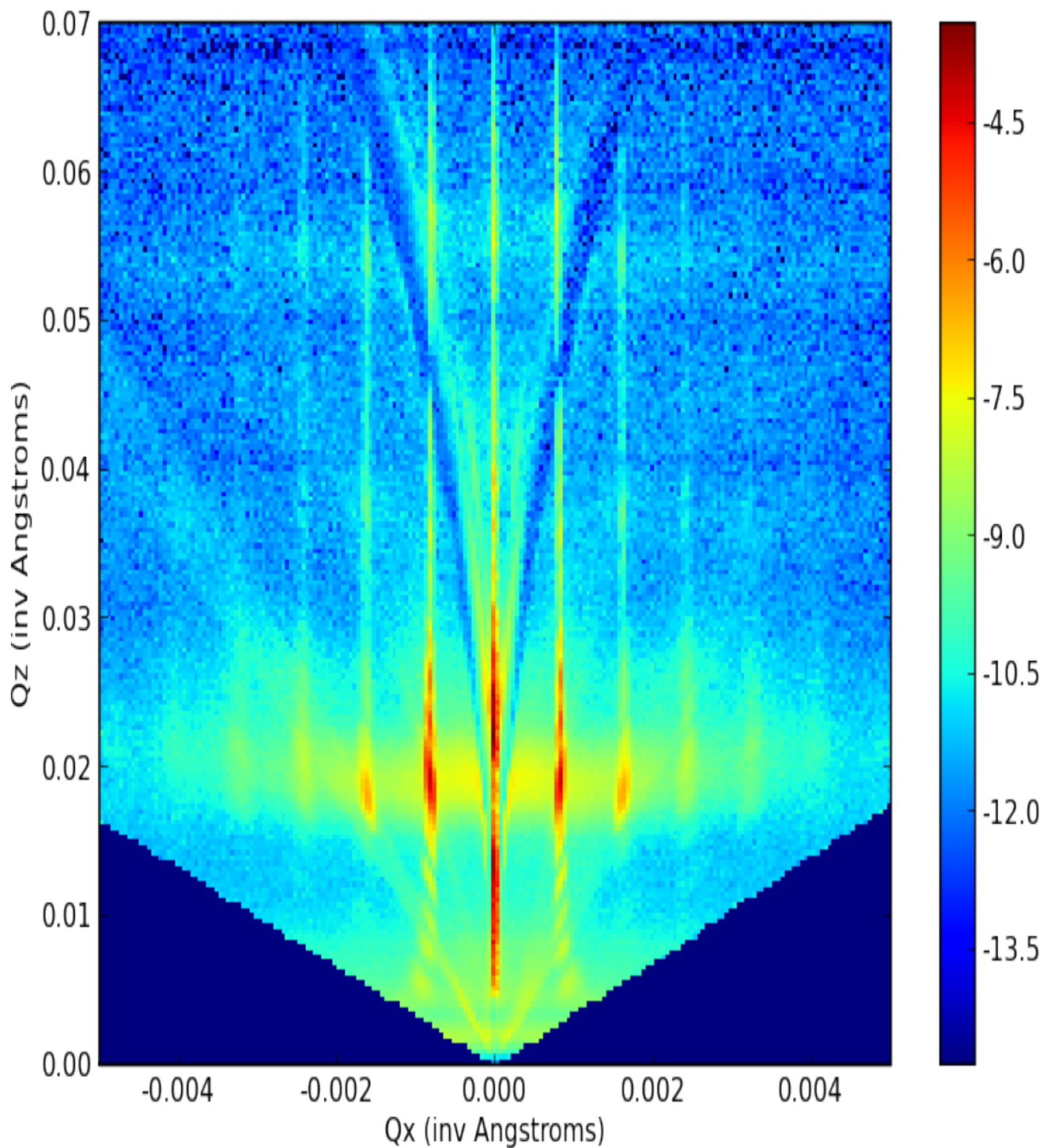
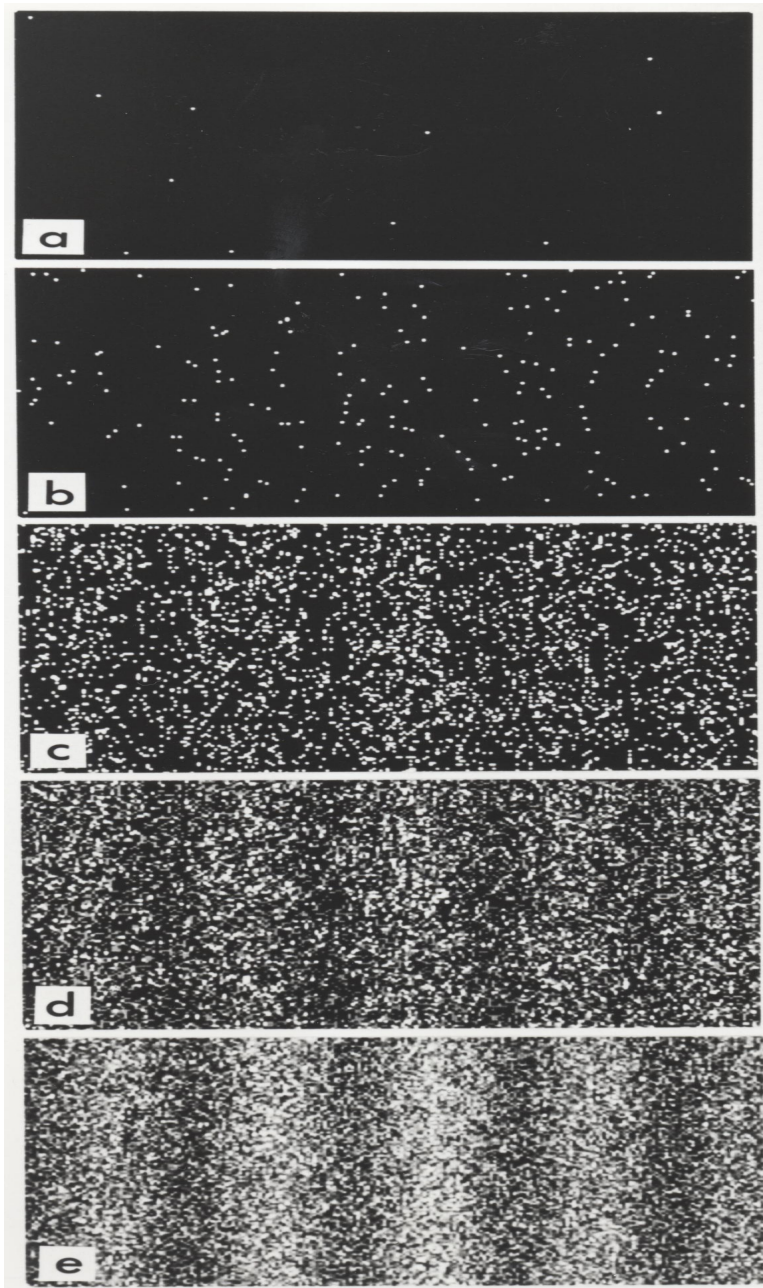


Diagram of expected orientation of di-block copolymer lamellae, with respect to the channels in the Si. The silicon substrate with etched channels is displayed in gray, with other lighter and darker regions corresponding to the two separate polymer components of the lamellae.



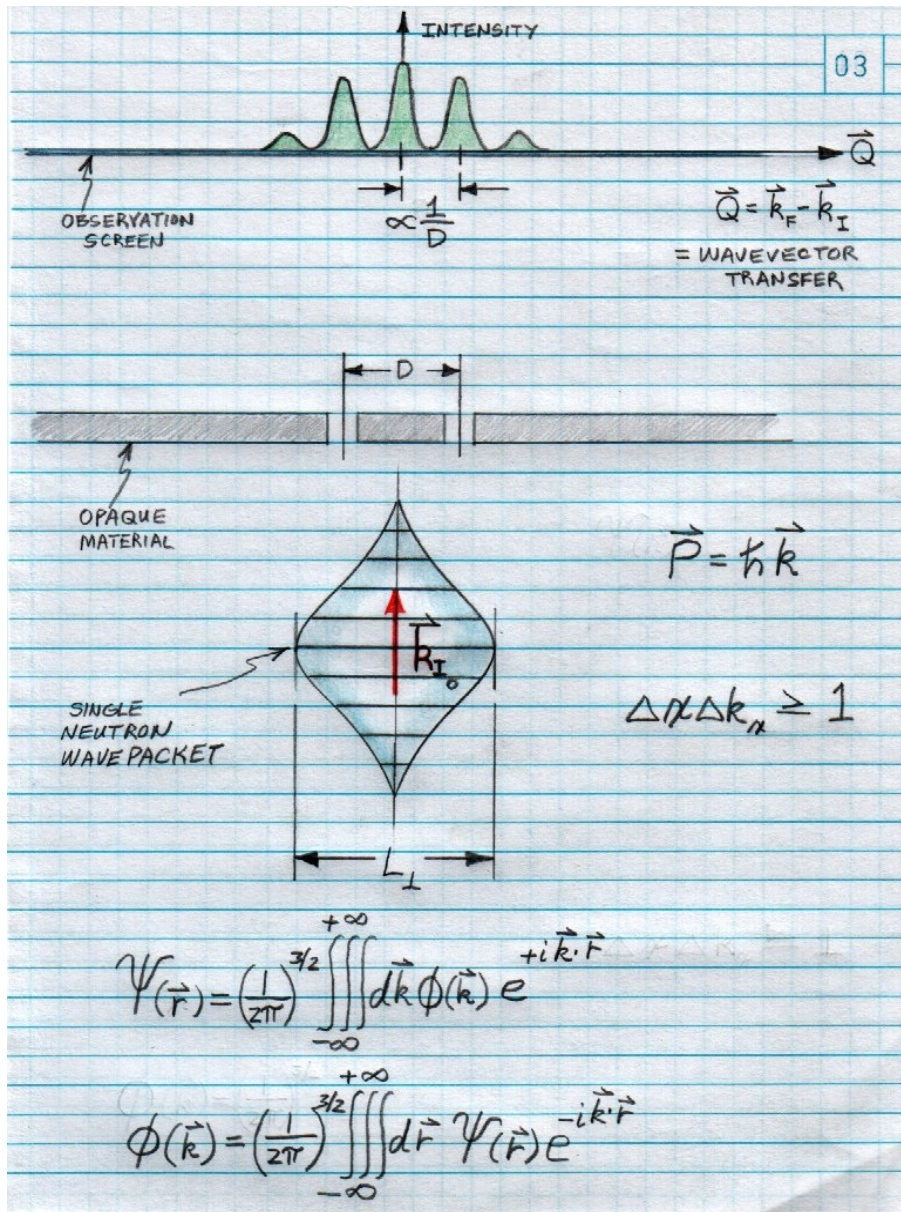
Neutron diffraction from Si channels filled with ordered di-block copolymer.

Part 2: Neutron wave characteristics and coherence

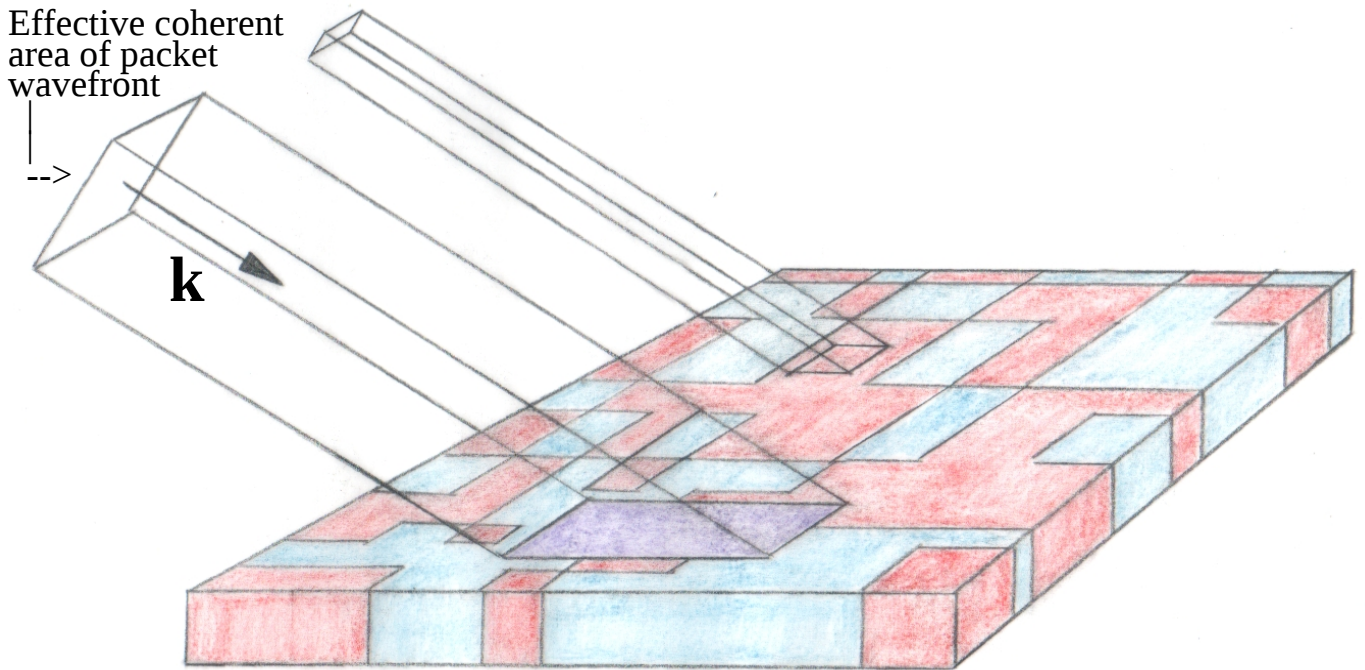


Electron diffraction pattern from a double slit -- one electron at a time (courtesy of Dr. Tanamura via Wikipedia.org). A liquid hydrogen moderator at a nuclear reactor facility acts as a spatially and temporally incoherent source of non-interacting, independent, individual neutrons described by wave packets which are to some degree localized in space. A collection of these individual wave packets can form a beam for use in a scattering instrument. The angular and energy distributions of the mean wave vectors associated with the neutron wave packets which make up a beam can be described as an incoherent instrumental resolution, as mentioned previously. (An incoherent source such as this is very different than a laser, for example, which produces photons in a highly-correlated, many-body state.)

Double slit diffraction of a wave packet describing a matter wave such as a neutron is depicted in the figure below.



Although the representation of a neutron as a plane wave is accurate as a solution of the one-dimensional Schroedinger wave equation for certain descriptions of specular reflection, there are important limitations. A plane wave is a mathematical idealization that has infinite spatial extent (and possesses, therefore, wavefronts which are perfectly coherent). This is physically unrealistic -- the neutron has a wave / particle duality and must be localized to some extent in space in a way that is consistent with the Heisenberg uncertainty relation of quantum mechanics. A single neutron interferes with the diffracting object by itself -- but the interference pattern becomes evident only after a sufficient number of such neutrons are collected at various locations in a detector to provide the required statistical accuracy.



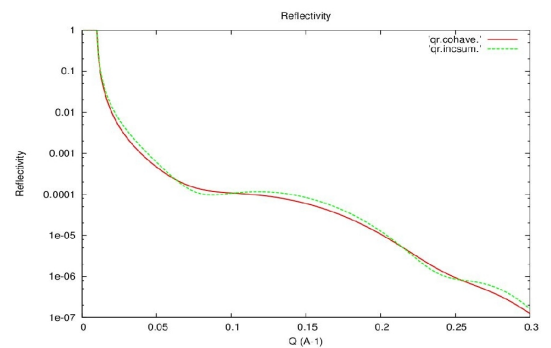
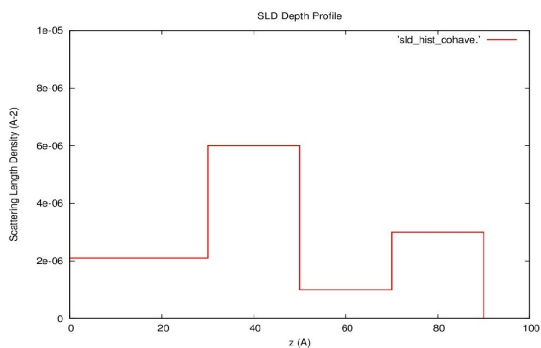
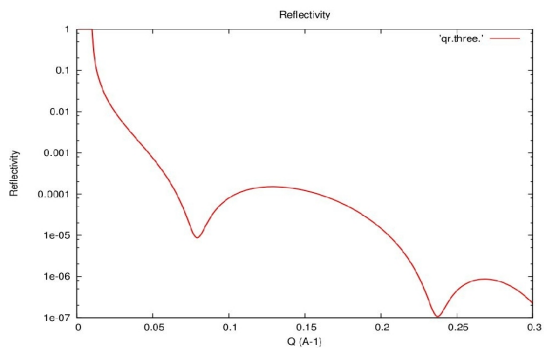
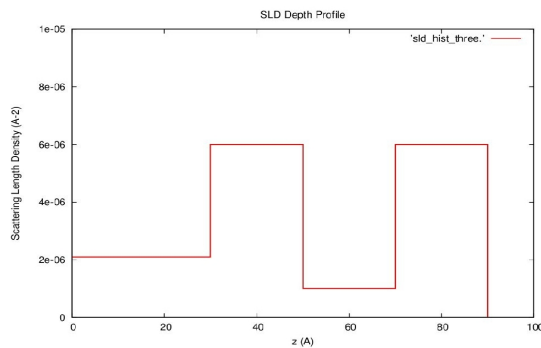
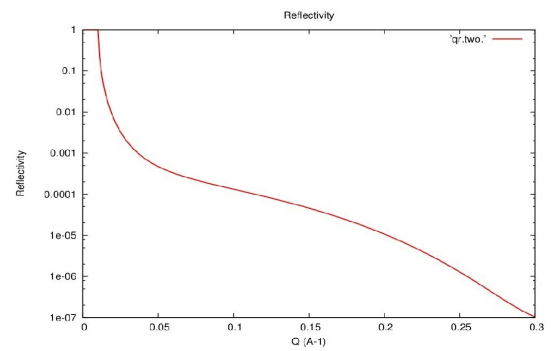
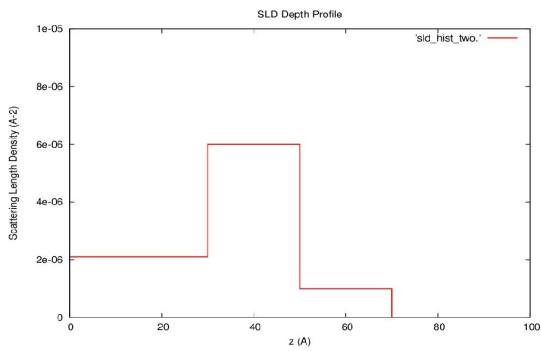
The effective transverse coherence area perpendicular to the propagation direction of the neutron wave packet is projected onto the film surface defining an area over which in-plane variations in SLD are averaged over in the specular process (note that the glancing angle of incidence enhances the projection along one in-plane direction):

$$r = (4\pi / (iQ)) \int_{-\infty}^{+\infty} \psi_{kz}(z) \langle \rho(x,y,z) \rangle_{x,y} e^{ikz} dz$$

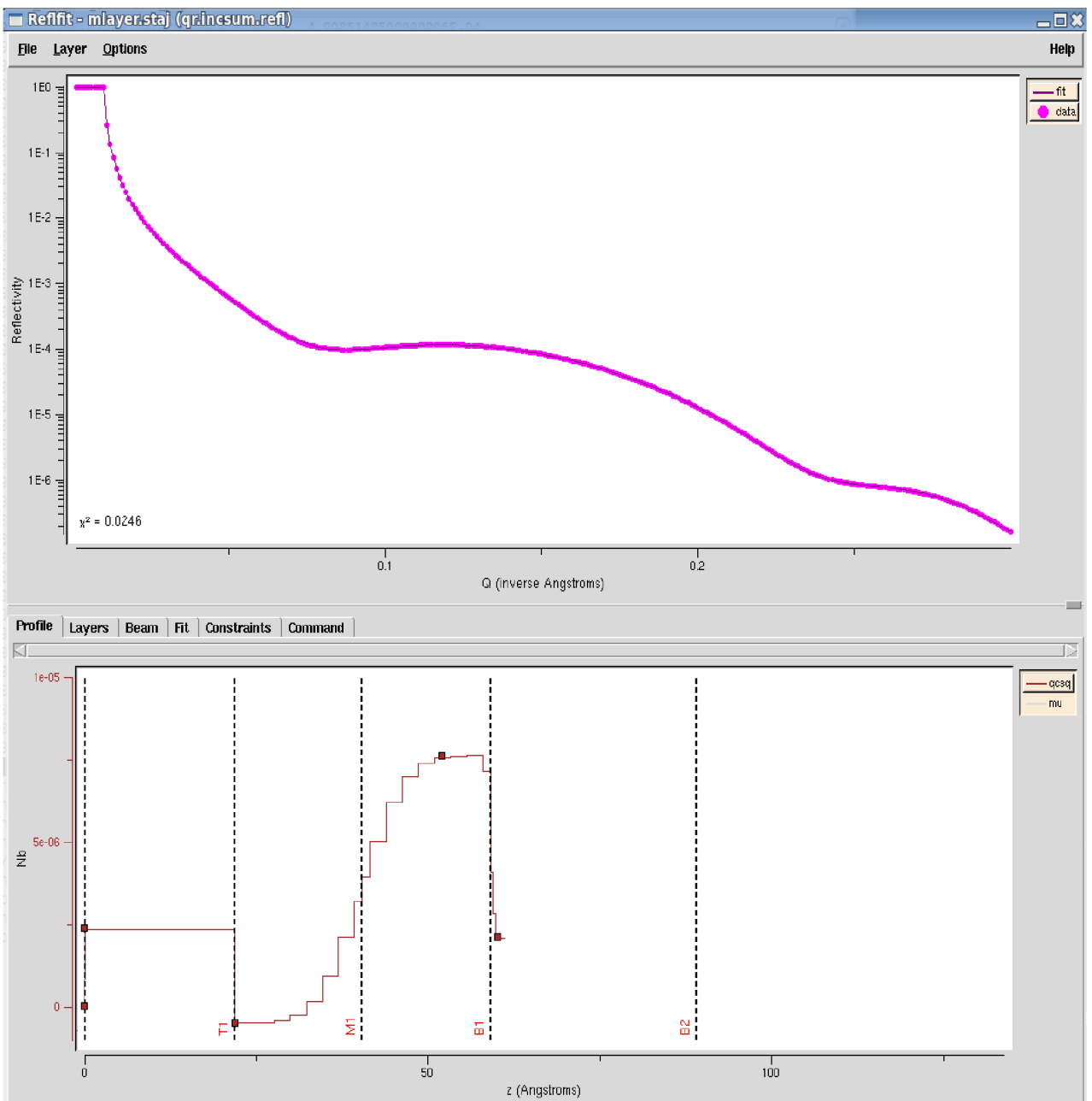
$$\langle \rho(x,y,z) \rangle_{x,y} = (1/A) \int_{-\infty}^{+\infty} \rho(x,y,z) dx dy$$

The length scale of the SLD variations must be small enough for effective averaging to occur within the projected area. (The purple shaded area is meant to represent the coherent average of separate areas of “red” and “blue” SLD.) If not, then the net measured reflected intensity $|r|^2$ is an area-weighted sum of reflectivities, each corresponding to an in-plane averaged SLD within a particular respective area, as depicted schematically in the figure above for the case of two distinct areas of different SLD (red and blue areas):

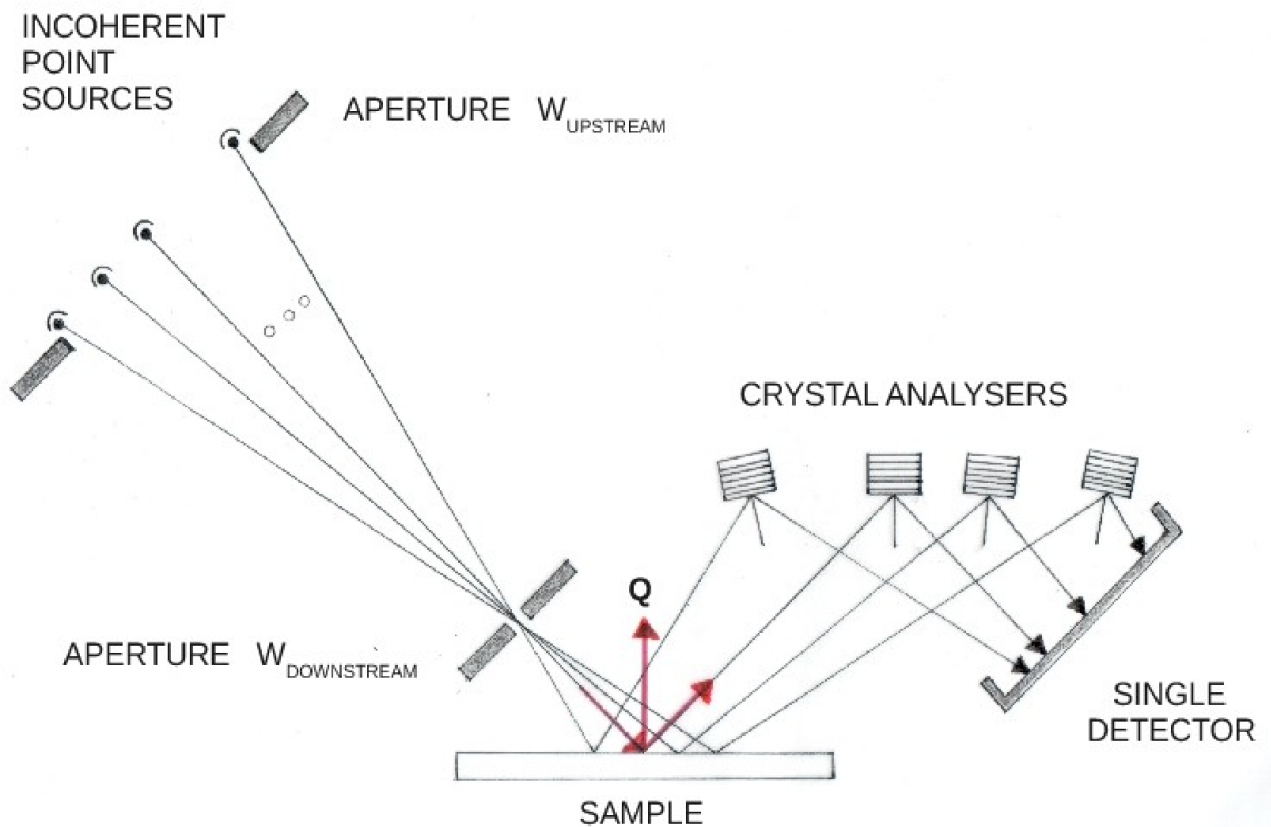
$$|r_{\text{NET MEASURED}}|^2 = (A_{\text{RED}} / A_{\text{TOTAL}}) |r_{\text{RED}}|^2 + (A_{\text{BLUE}} / A_{\text{TOTAL}}) |r_{\text{BLUE}}|^2$$



Three model SLD profiles with their corresponding specular reflectivity curves. The bottom profile, however, represents an average of the upper two assuming equal areas of coverage in the plane of the substrate. Corresponding to this bottom profile are two reflectivity curves -- one in which coherent averaging occurred, the other in which the net measured reflected intensity corresponds to a sum of two equally weighted reflectivities associated with the two upper SLD profiles. Although the two reflectivity curves on the bottom right appear very similar, comparing the results of fitting these two curves is anything but, as demonstrated in the next slide.



The top part of the figure shows the reflectivity corresponding to the *incoherent* sum case for the bottom SLD profile of the preceding slide -- along with a fit to the model data assuming (incorrectly -- for the purpose of illustration) that the reflectivity data represented a single uniform in-plane SLD. Note that the SLD profile corresponding to this fit -- as plotted in the lower part of the figure -- is physically meaningless. Clearly, it is essential to know whether in-plane inhomogeneities are being effectively averaged over by the incident neutron wave packet to be able to properly analyze and interpret a specular reflectivity measurement.



The liquid hydrogen moderator source, neutron guide, and all of the components of the reflectometer -- apertures, substrate on which sample film is deposited, monochromating crystals, etc., contribute, in varying degrees, to determining both the size, shape, and coherence of each individual neutron wave packet -- as well as to defining the distributions in direction and magnitude of the mean wavevectors of each of the wave packets in the ensemble composing the beam.

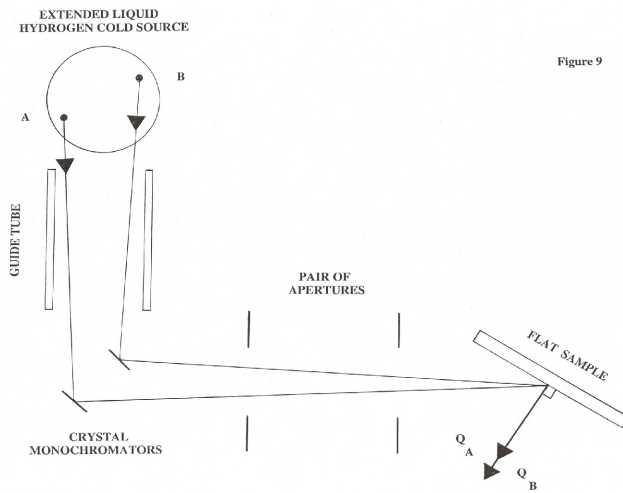


Figure 3a.

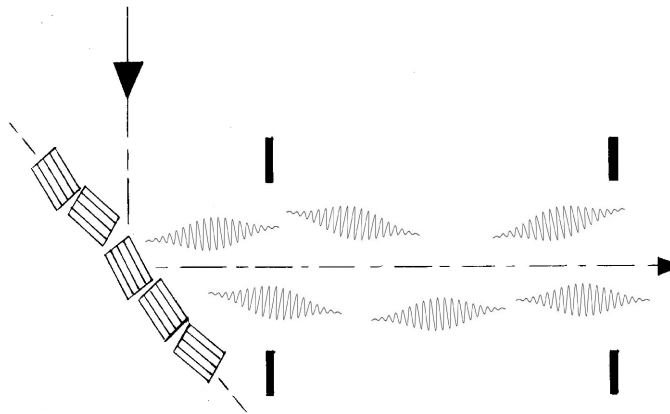


Figure 3b.

Another, more typical, configuration of a neutron reflectometer at a steady-state reactor source, using a single highly monochromatic incident beam, is shown in the upper diagram. The lower figure is a schematic representation of the incident neutron beam -- composed of localized, individual neutron wave packets -- possessing a distribution of mean wavevector directions and magnitudes.

It is possible to differentiate by experiment, to some degree, the coherent properties of the wave packets from the incoherent distributions of angle and wavelength associated with the beam, as illustrated in a following slide through the use of well-characterized material structures such as diffraction gratings.

Figure 13

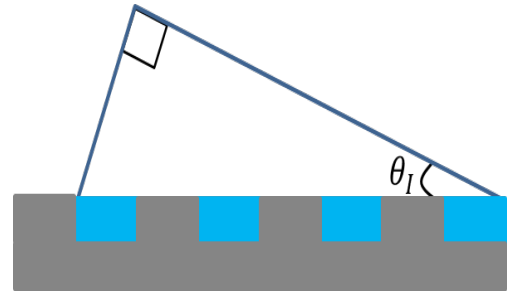
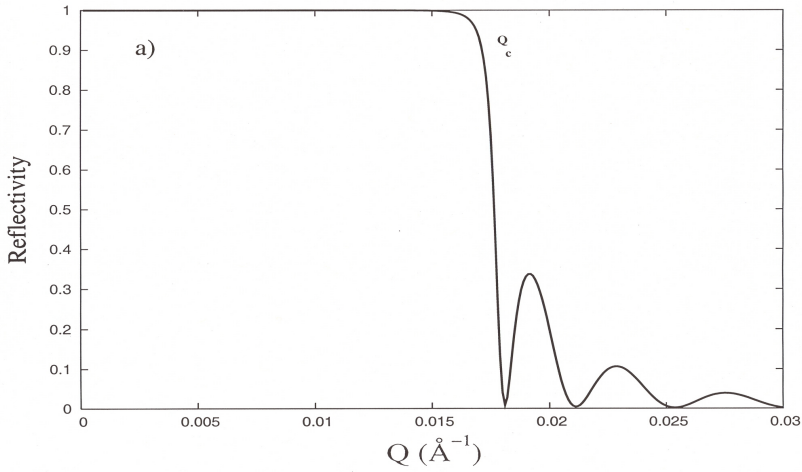
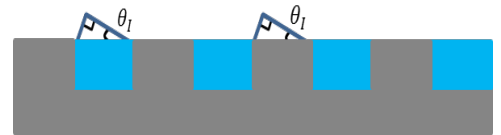
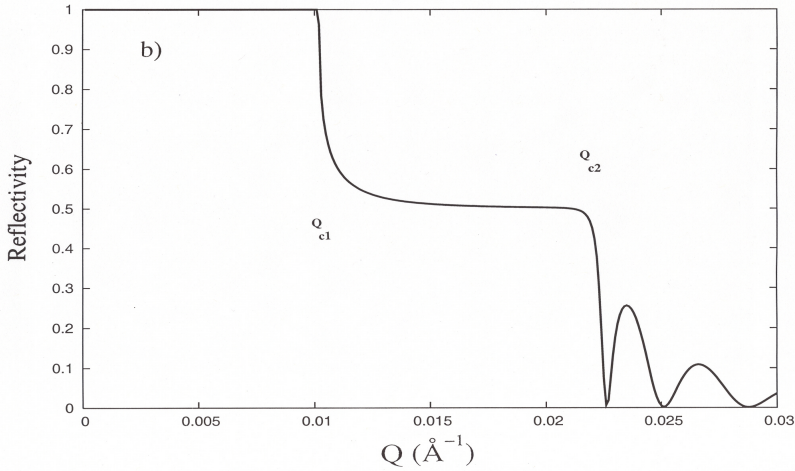
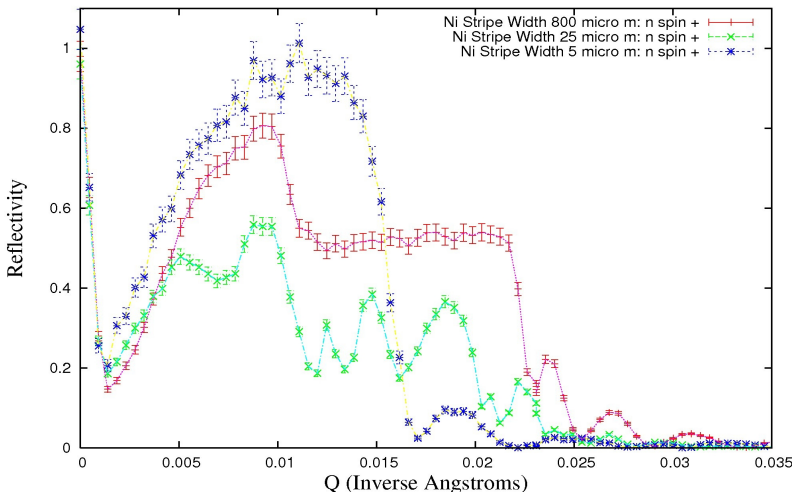


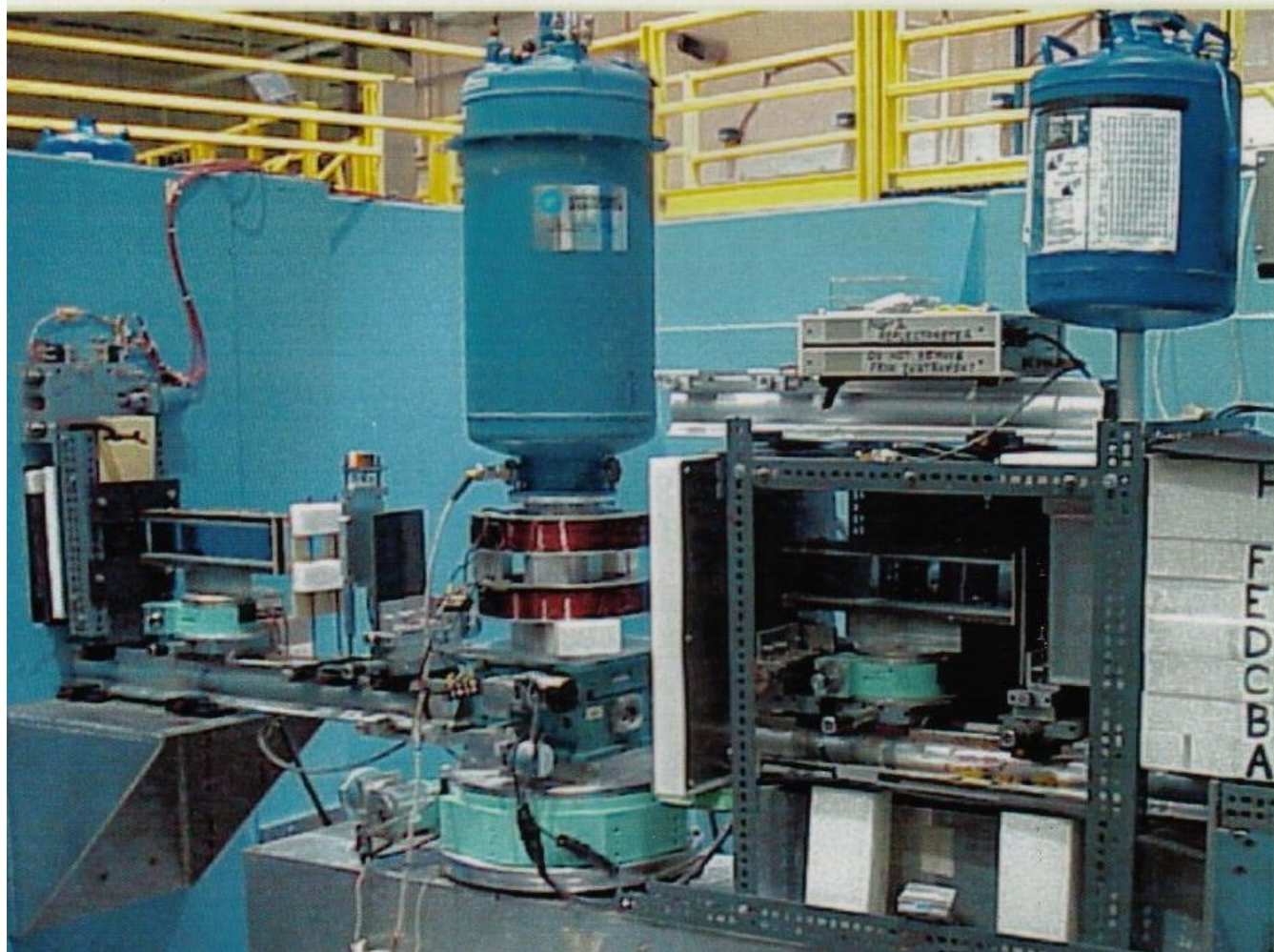
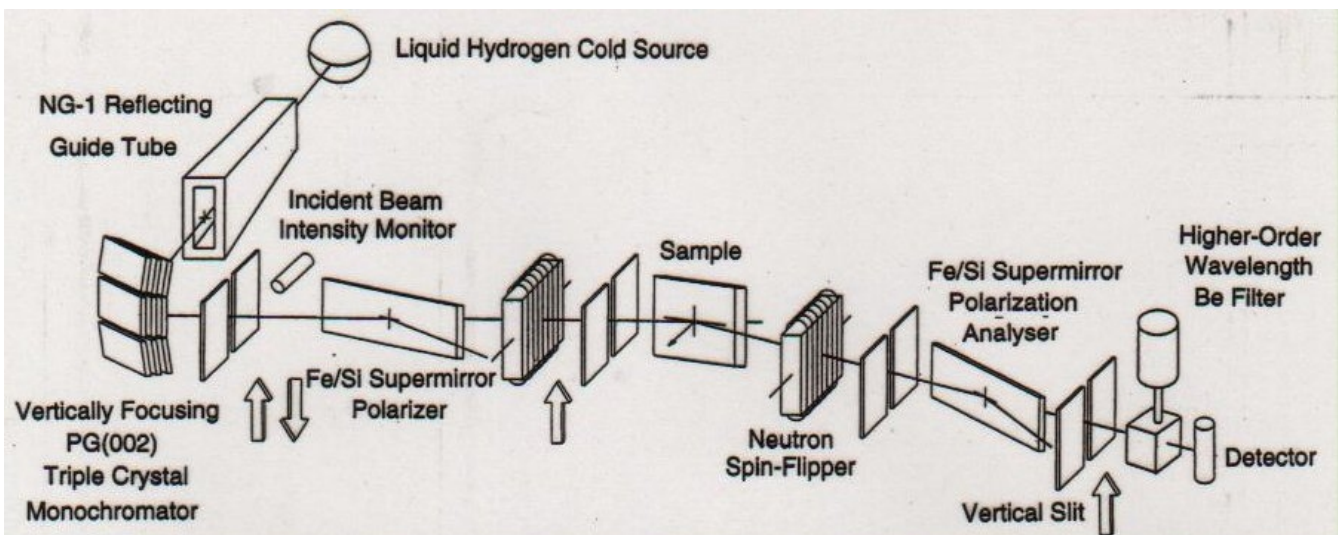
Figure 13



Model grating structures composed of two materials with different SLD values. Top -- the wave front of the neutron packet effectively averages over the in-plane density variations in specular reflection so that only a single critical angle is observed. Middle -- case where transverse coherence of the wavefront (perpendicular to the packet's mean \mathbf{k} vector) is not large enough to average so that two critical edges, one for each material SLD, are evident. Bottom -- actual neutron specular reflectivity data (without geometrical footprint correction) corresponding to examples for all three cases: coherent averaging; an incoherent sum of separate weighted reflectivities; and an intermediate case.

Grating Stripes Perpendicular to Scattering Plane

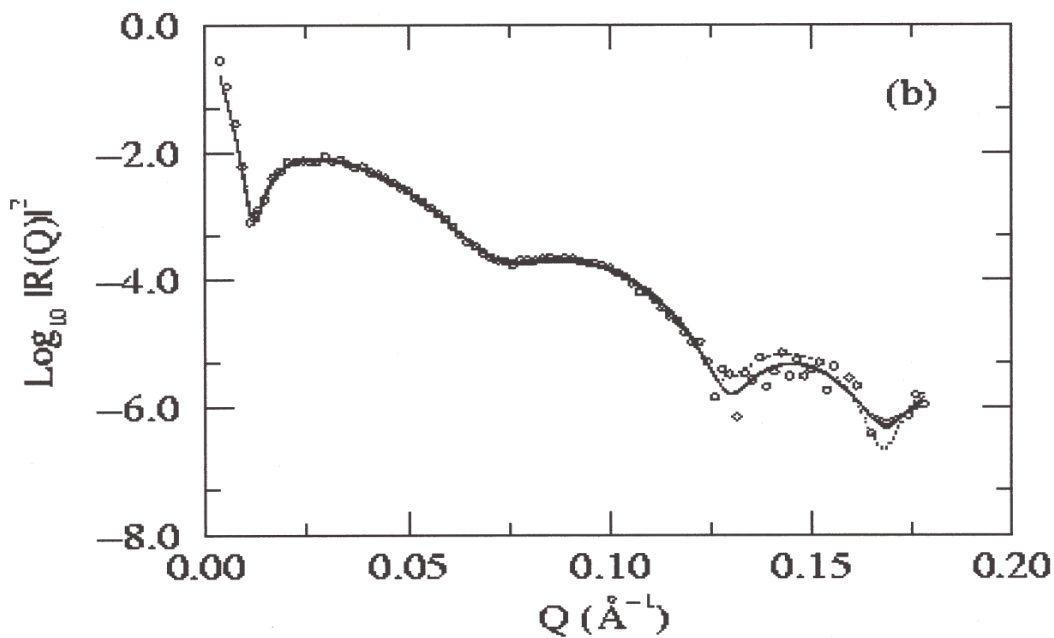
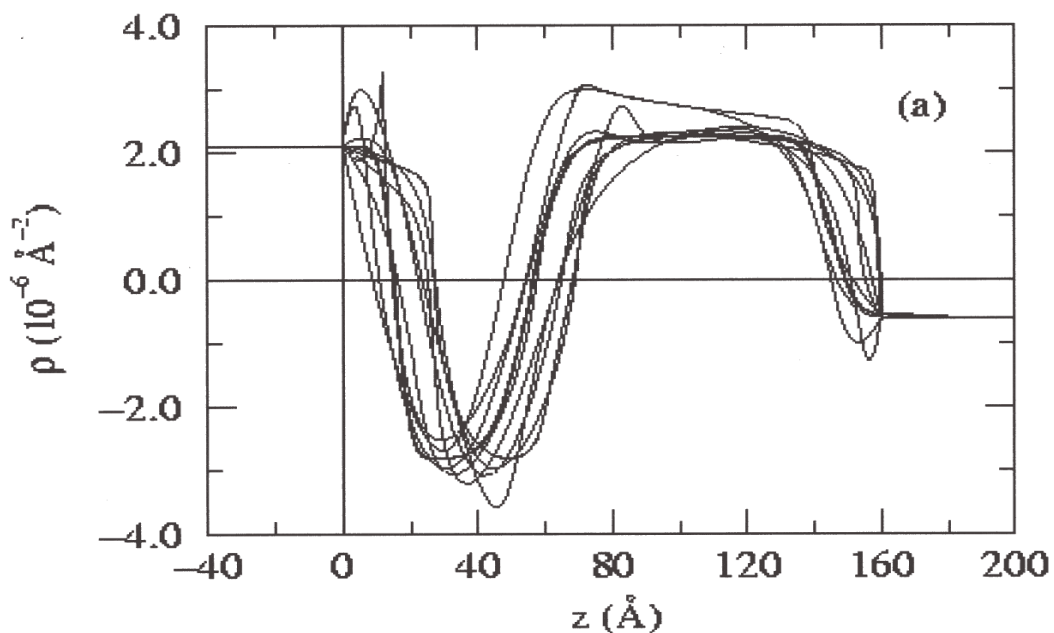




Polarized neutron reflectometer at NIST

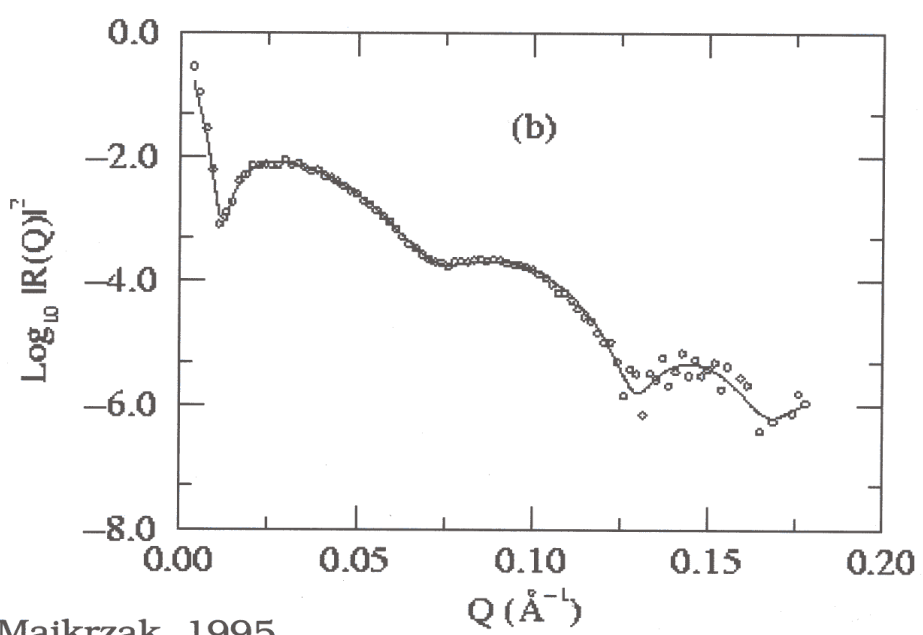
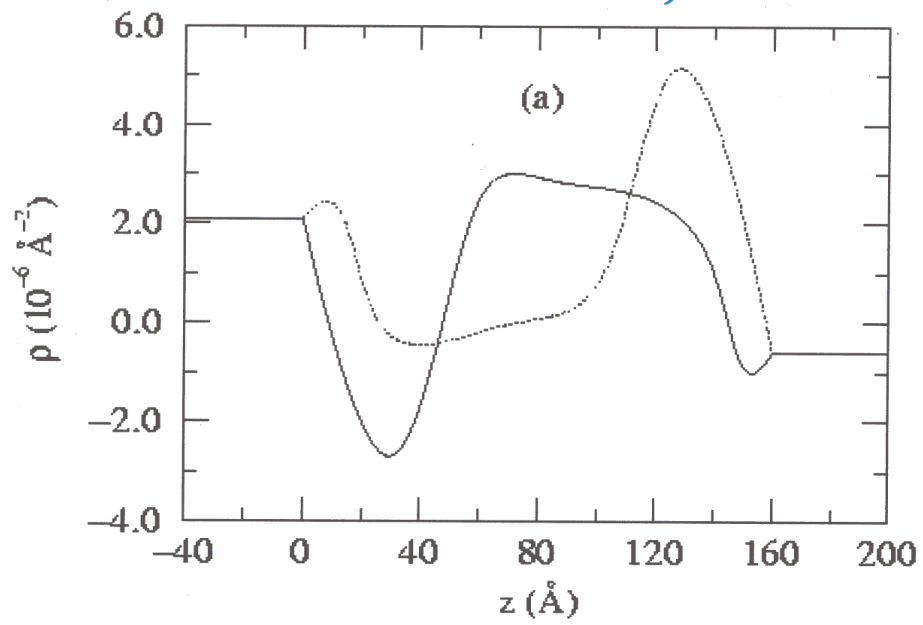
Part 3: The Phase problem, Direct Inversion and Simultaneous Fitting

- <> ambiguous SLD profiles from reflected *intensities*
- <> measurement of reflection *amplitude* via references yields unique solution -- one-to-one correspondence with SLD profile
- <> given the reflection amplitude, exact, first-principles inversion to obtain unique SLD profile for specular reflection is possible
- <> simultaneous fitting of multiple composite (sample + reference) reflectivity data sets can lead to unambiguous solution as well



Repeated fits of reflectivity data from a Ti/TiO film system on a Si substrate in contact with an aqueous reservoir (Berk et al.). The variation among the individual fits is indicative of the accuracy attainable in the SLD profile given the truncation of the reflectivity data at a maximum value of Q and the statistical uncertainty in the data points.

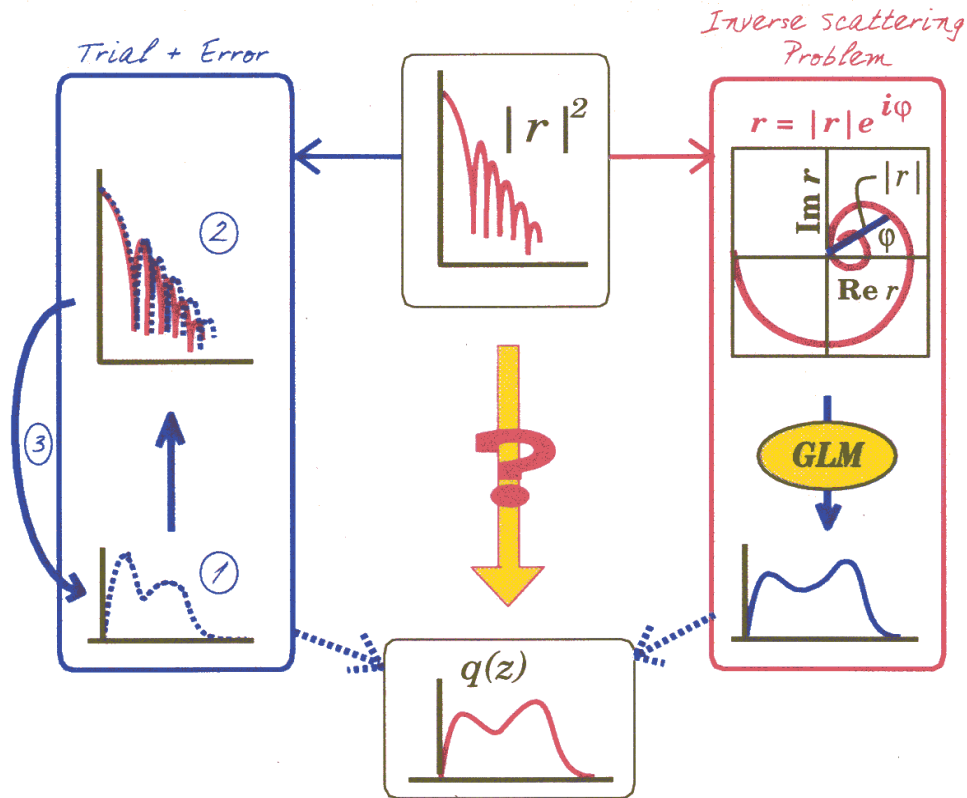
TiO in situ: Wiesler, et al.



Berk & Majkrzak, 1995

It was found that if enough individual fits were performed, another “family” of fits emerged (only one of which is shown above in comparison to a representative fit of the other family shown on the previous slide) with essentially the same chi-squared goodness of fit criteria -- this alternative SLD profile is a consequence of the loss of phase information inherent when the reflectivity $|r|^2$ (proportional to the reflected *intensity*) is measured rather than the complex reflection *amplitude* r -- i.e., the non uniqueness arises from a loss of the phase information carried by the reflected wave function.

Inverting reflectivity



Phase determination

C.F. Majkrzak and N.F. Berk, Phys. Rev. B **52**, 10827 (1995).
V.-O. de Haan, et al., Phys. Rev. B **52**, 10830 (1995).

H. Leeb, H.R. Lipperheide and G. Reiss, this conference.

Logarithmic dispersion

W.L. Clinton, Phys. Rev. B **48**, 1 (1993).

Tunneling times

H. Fiedeldey, H.R. Lipperheide, et al., Phys. Lett. A **170**, 347 (1992).

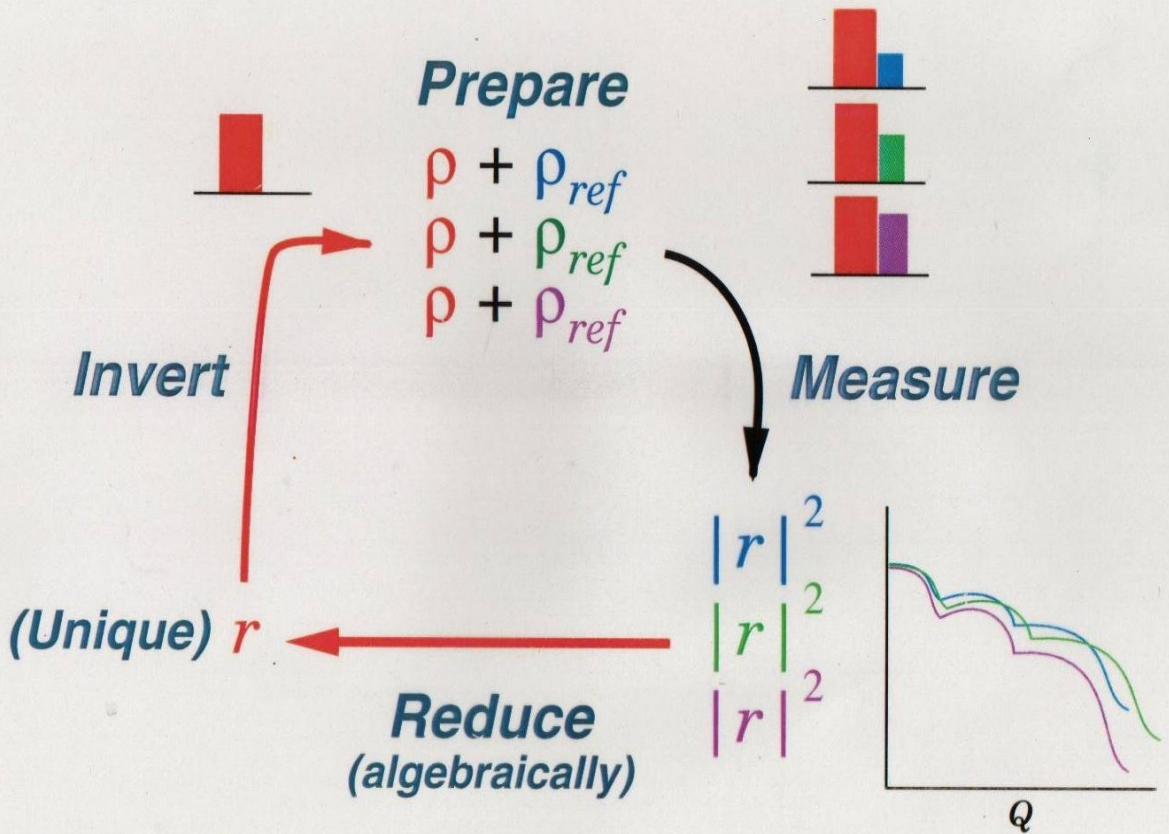
Pseudo-inversion

S.K. Sinha, et al., *Surface X-Ray and Neutron Scattering*, 85 (Springer, 1992).
C.F. Majkrzak, N.F. Berk, et al., SPIE Proc. **1738**, 282 (1992).

NIST

It turns out that it is possible to solve the phase problem for specular neutron reflectometry, in most cases, exactly, through the use of reference film layers -- in essence this is analogous to an interferometric method such as holography.

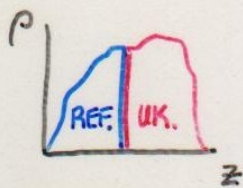
Phase Determination with 3 References



Majkrzak & Berk, 1995
de Haan, et al., 1995

FORMALISM ALLOWS A COMPOSITE POTENTIAL TO BE EXPRESSED AS A PRODUCT:

$$\underbrace{\begin{pmatrix} A & B \\ C & D \end{pmatrix}}_{\text{COMPOSITE}} = \underbrace{\begin{pmatrix} a & b \\ c & d \end{pmatrix}}_{\text{UNKNOWN}} \underbrace{\begin{pmatrix} w & x \\ y & z \end{pmatrix}}_{\text{REFERENCE}}$$



COMPOSITE (1, 2, 3) UNKNOWN REFERENCE (1, 2, 3)

$$|R(Q)|^2 = |R_1(Q)|^2, |R_2(Q)|^2, \text{ and } |R_3(Q)|^2$$

$$\Sigma_i \equiv 2 \left[\frac{1 + |R_i|^2}{1 - |R_i|^2} \right] = A_i^2 + B_i^2 + C_i^2 + D_i^2$$

$$A_i^2 = a^2 w_i^2 + b^2 y_i^2 + 2abw_i y_i$$

$$C_i^2 = c^2 w_i^2 + d^2 y_i^2 + 2cdw_i y_i$$

$$B_i^2 = a^2 x_i^2 + b^2 z_i^2 + 2abx_i z_i$$

$$D_i^2 = c^2 x_i^2 + d^2 z_i^2 + 2cdx_i z_i$$

(INDEPENDENTLY AT EACH Q)

$$\Sigma_i = \underbrace{(w_i^2 + x_i^2)}_{\text{REF}} \alpha + \underbrace{(y_i^2 + z_i^2)}_{\text{REF}} \beta + 2 \underbrace{(w_i y_i + x_i z_i)}_{\text{REF}} \gamma$$

$$\alpha = a^2 + c^2$$

$$\beta = b^2 + d^2$$

$$\gamma = ab + cd$$

$i = 1, 2, 3$

SOLVE FOR UNKNOWN $\alpha, \beta,$ AND γ TO GET

$$R_{\text{UNKNOWN}} = \frac{(\beta - \alpha) - 2i\gamma}{2 + \beta + \alpha}$$

FOURIER TRANSFORM
OF THE COMPLEX
REFLECTION
AMPLITUDE

$$\mathcal{R}(z) = \frac{1}{\pi} \operatorname{Re} \int_0^{\infty} r(k_z) e^{ik_z z} dk_z$$

GELFAND
LEVITAN
MARCHENKO
INTEGRAL
EQUATION

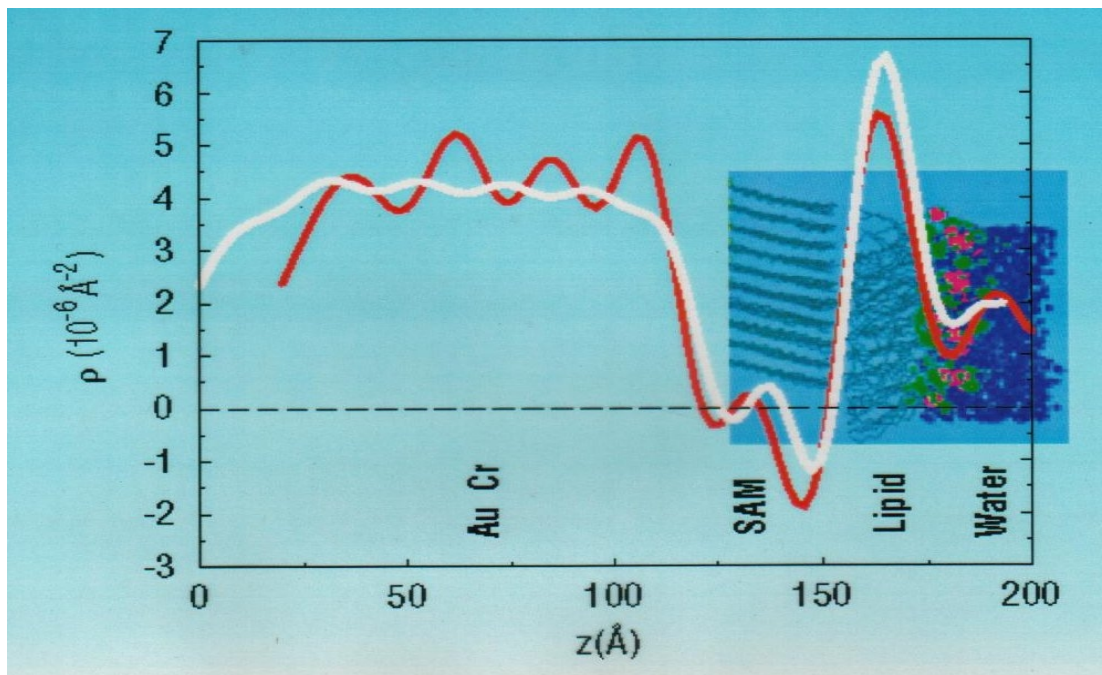
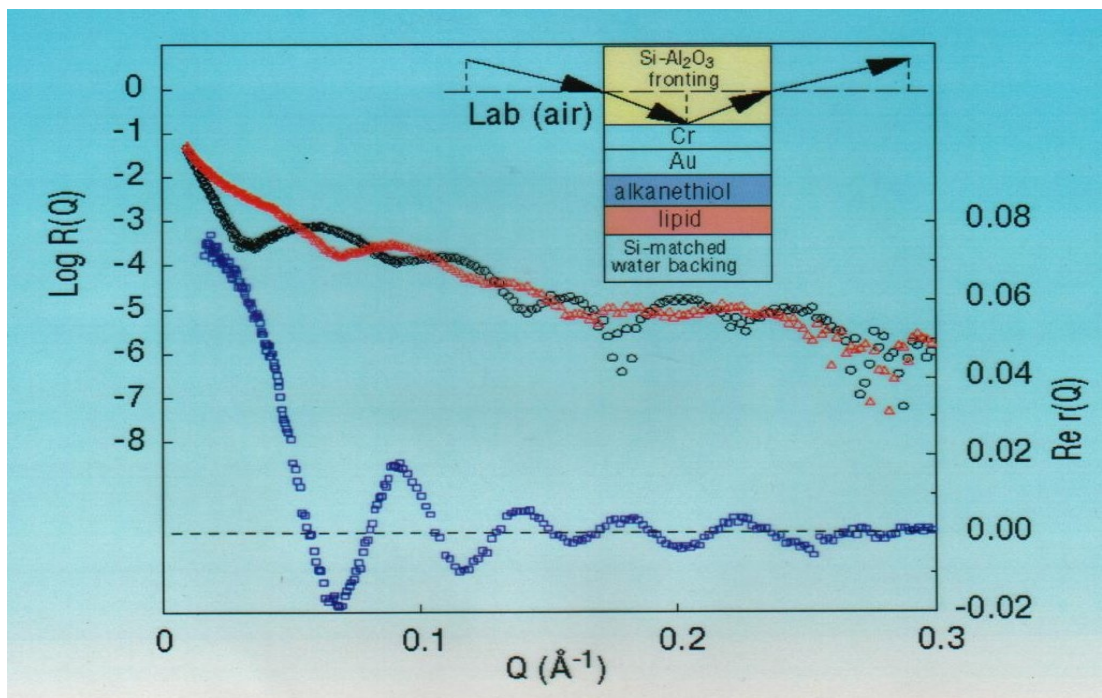
$$K(z, \gamma) + \mathcal{R}(z + \gamma) + \int_{-z}^{+z} K(z, x) \mathcal{R}(x + \gamma) dx = 0$$

SCATTERING
LENGTH
DENSITY

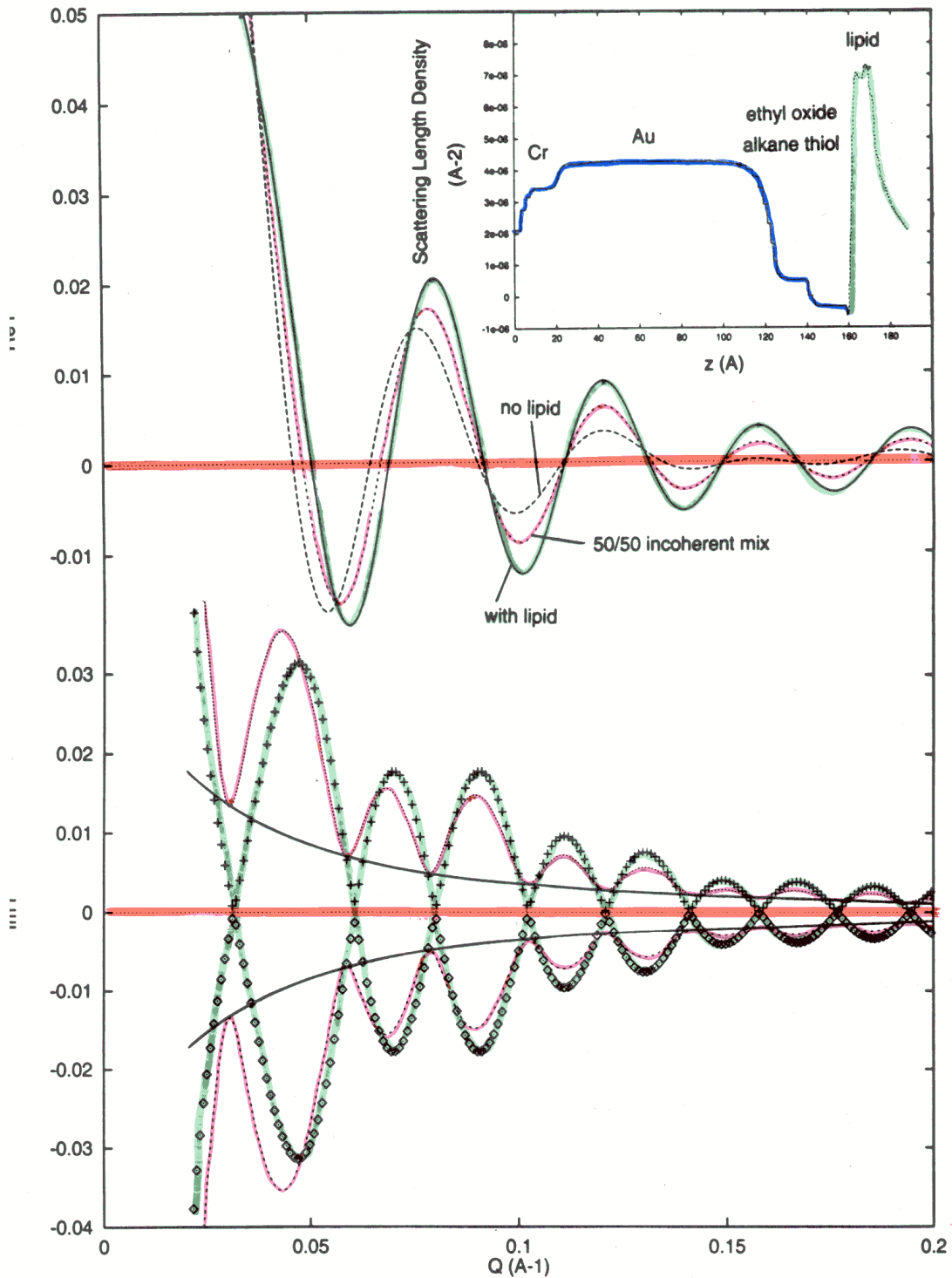
$$\rho(z) = 2 \frac{dK(z, z)}{dz}$$

GIVEN THE COMPLEX REFLECTION
AMPLITUDE, THE SCATTERING
LENGTH DENSITY ρ CAN BE
OBTAINED FROM AN EXACT,
FIRST PRINCIPLE INVERSION
FOR A REAL POTENTIAL OF
FINITE EXTENT — AND THE
SOLUTION IS UNIQUE!

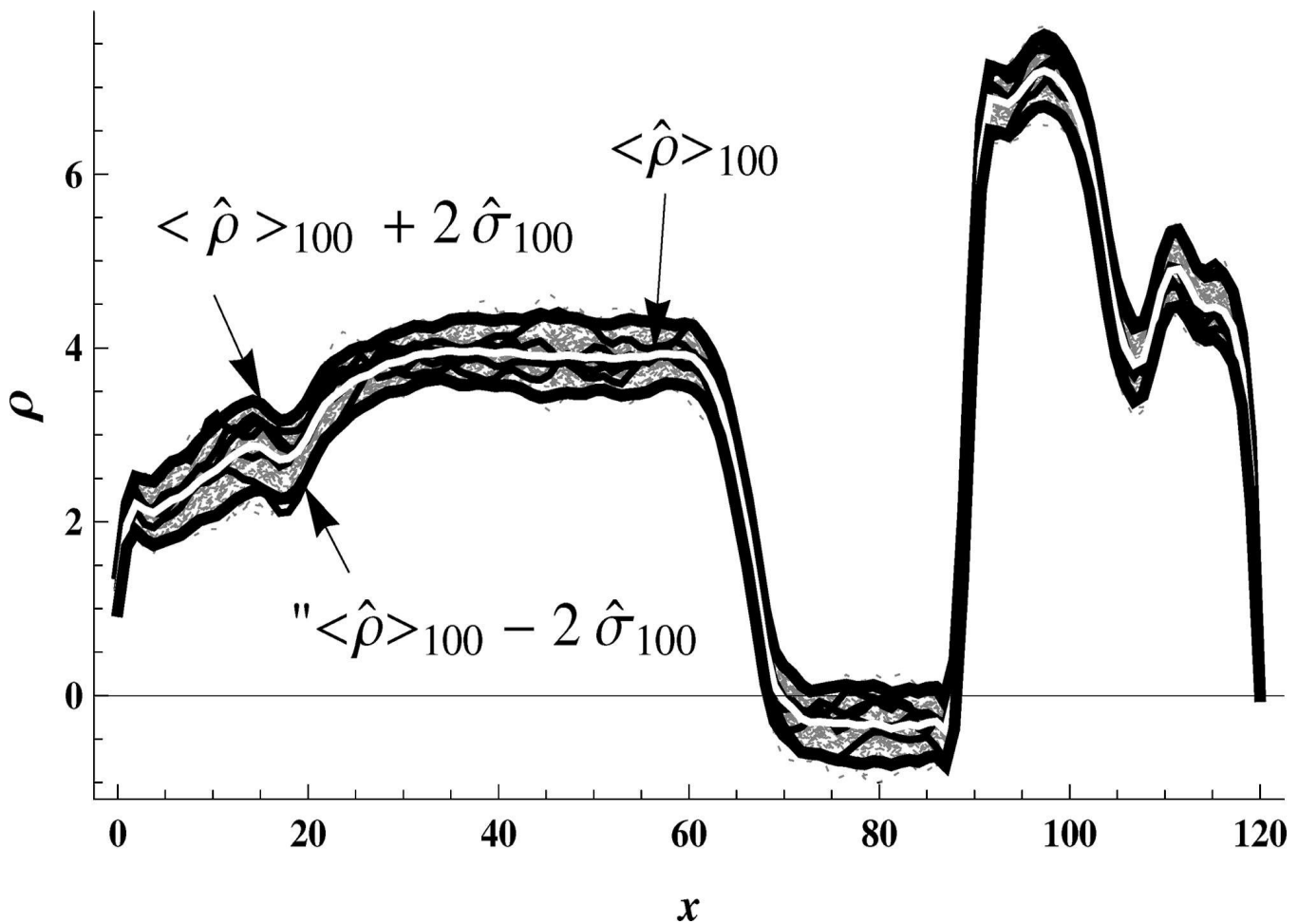
NO FITTING, NO ADJUSTABLE PARAMETERS



In the upper figure, the red and black reflectivity curves correspond to two composite system reflectivity data sets for the film structure in the inset and either Si or Al₂O₃ fronting medium -- from which the blue curve representing the real part of the reflection *amplitude* associated with the film structure of interest was obtained (here, the variable fronting media serve as the reference parts of the composite systems). In the lower figure is the SLD profile (in red) obtained from a first-principles inversion of the exact $Re\ r$ (from the upper figure) -- the “ringing” evident in the gold layer region is due to a truncation of the reflectivity data at a finite Q maximum. The white curve is the SLD profile calculated by a molecular dynamics model simulation of the lipid bilayer membrane which was actually deposited on the substrate for the experiment.



An additional benefit of determining the phase -- i.e., the real and imaginary parts of the reflection amplitude -- is that the presence of any in-plane inhomogeneity in the SLD which is not properly averaged over by the incident neutron packet wavefront shows up as a characteristic splitting of the quadratic roots of the equation for $\text{Im } r$.



“Statistical Analysis of Phase-Inversion Neutron Specular Reflectivity”, N.F.Berk and C.F.Majkrzak, *Langmuir* 25, 4132 (2009).

The phase-inversion method, besides providing a unique solution for the SLD depth profile obtained from a specular neutron reflectivity measurement, also enables a direct analysis of the uncertainty in the SLD profile so-obtained in terms of the truncation of the reflectivity data at a maximum Q and the statistical uncertainties in the reflectivity data points.

Part 4: Applications of NR to studies of the nano-scale structure of thin film materials

<> Soft condensed matter:

-- polymers

-- bio-membranes

-- organic photo-voltaic films

...

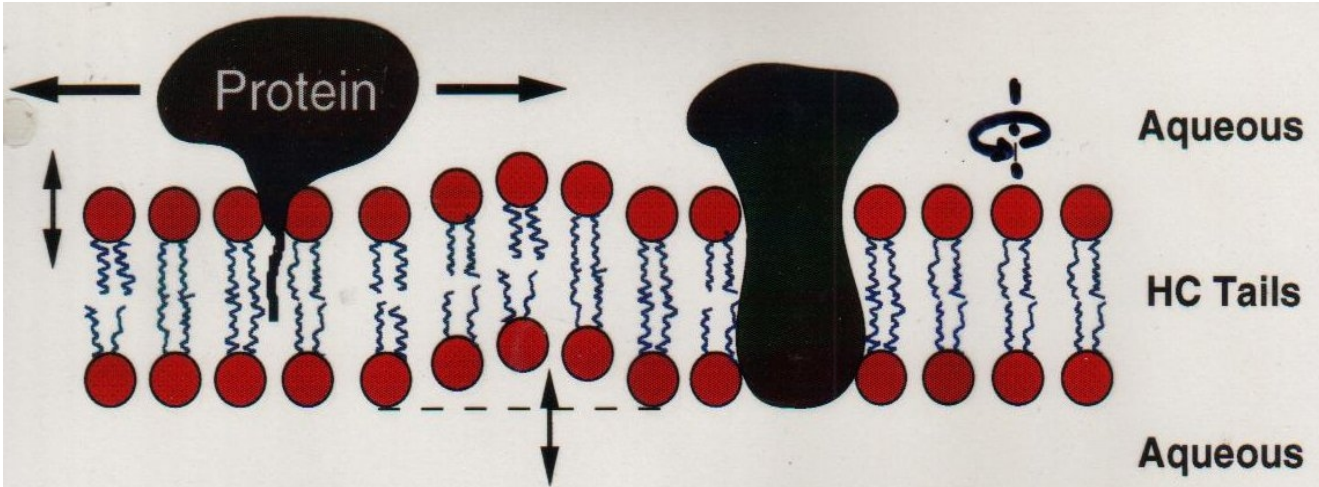
<> Hard condensed matter:

-- magnetic materials (to be discussed in a following lecture)

-- chemical interdiffusion (e.g., $^{58}\text{Ni}/^{62}\text{Ni}$)

-- metal hydrides

...



Supported Lipid Bilayers

A model system to mimic the structure and dynamics of cell membranes.

Proteins in Lipid Bilayers

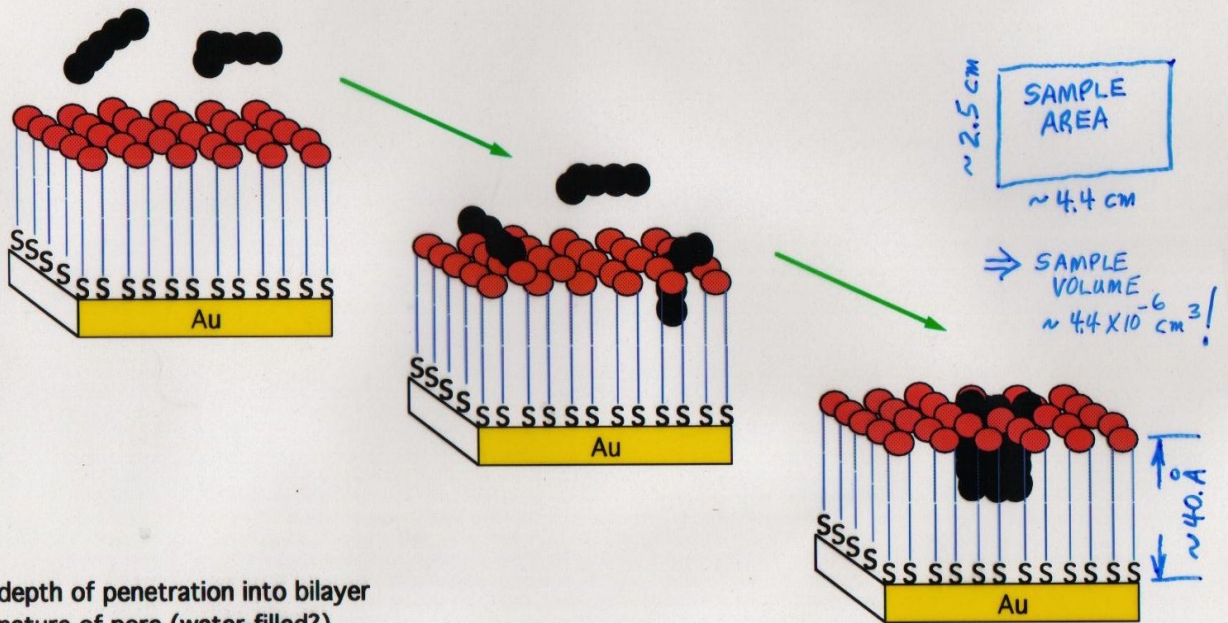
- Difficult to characterize by traditional x-ray crystallography.
- Play a crucial role in cell function
 - regulate ion and nutrient transport
 - engage in binding, signalling and cell recognition
 - participate in cell fusion events.

Biosensors (Anne Plant & coworkers)

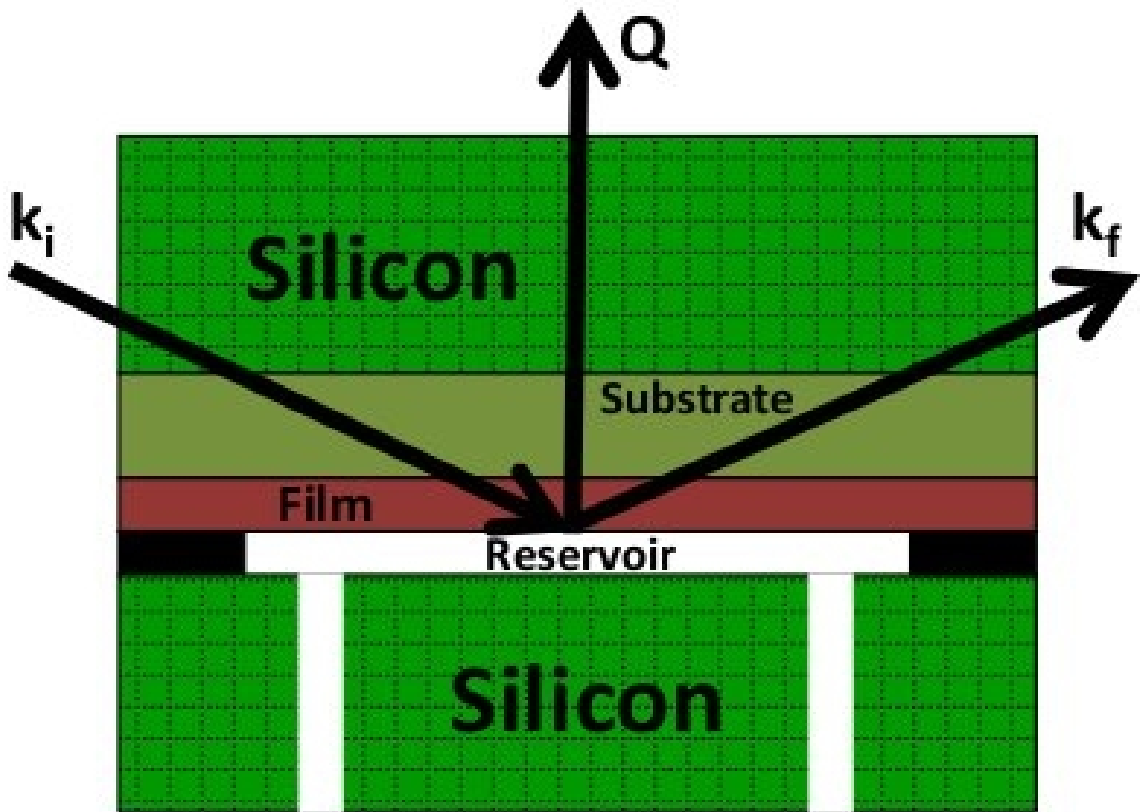
Melittin in Hybrid Bilayer Membranes

S. Krueger, A. Plant, et al., NIST
(Langmuir)

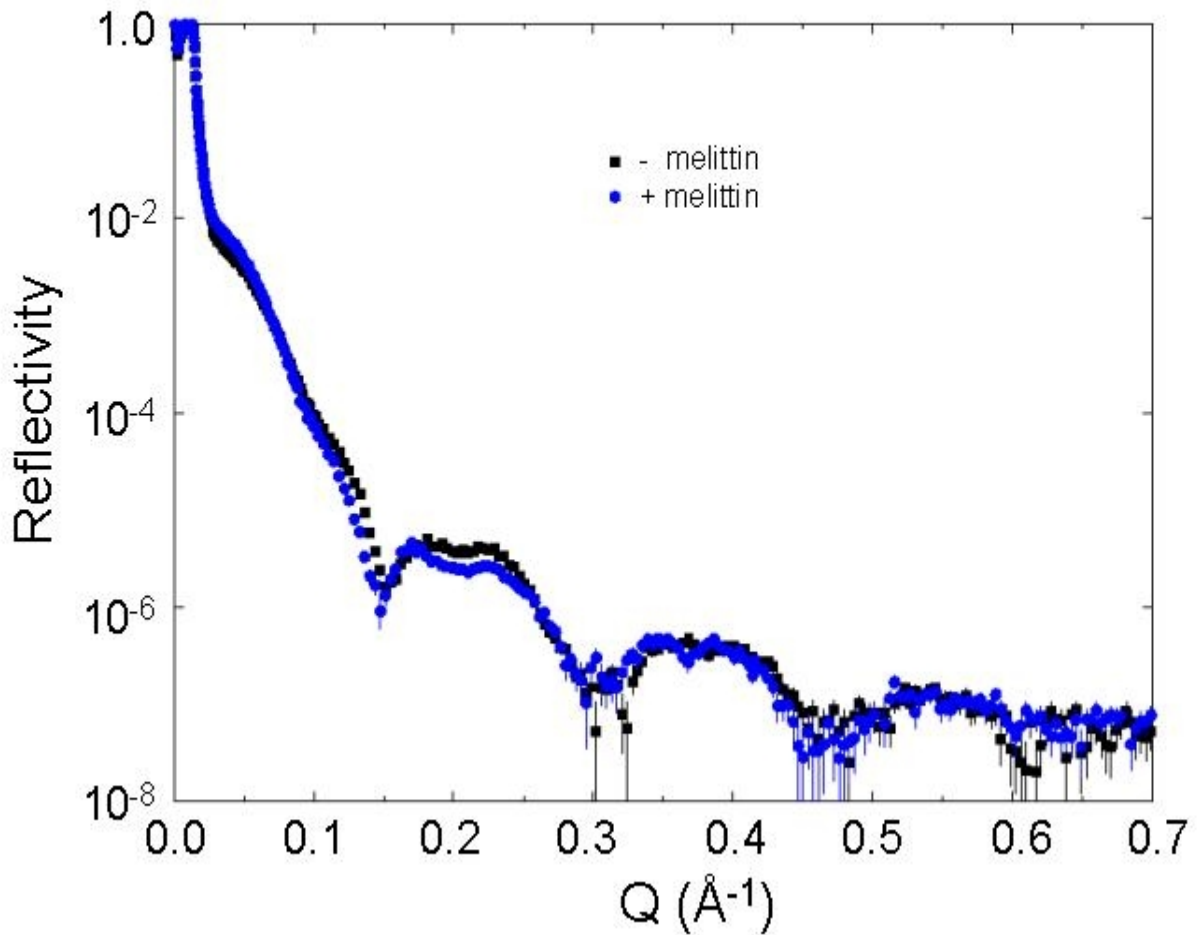
- pore-forming toxin
- used as model membrane peptide
- active in HBMs



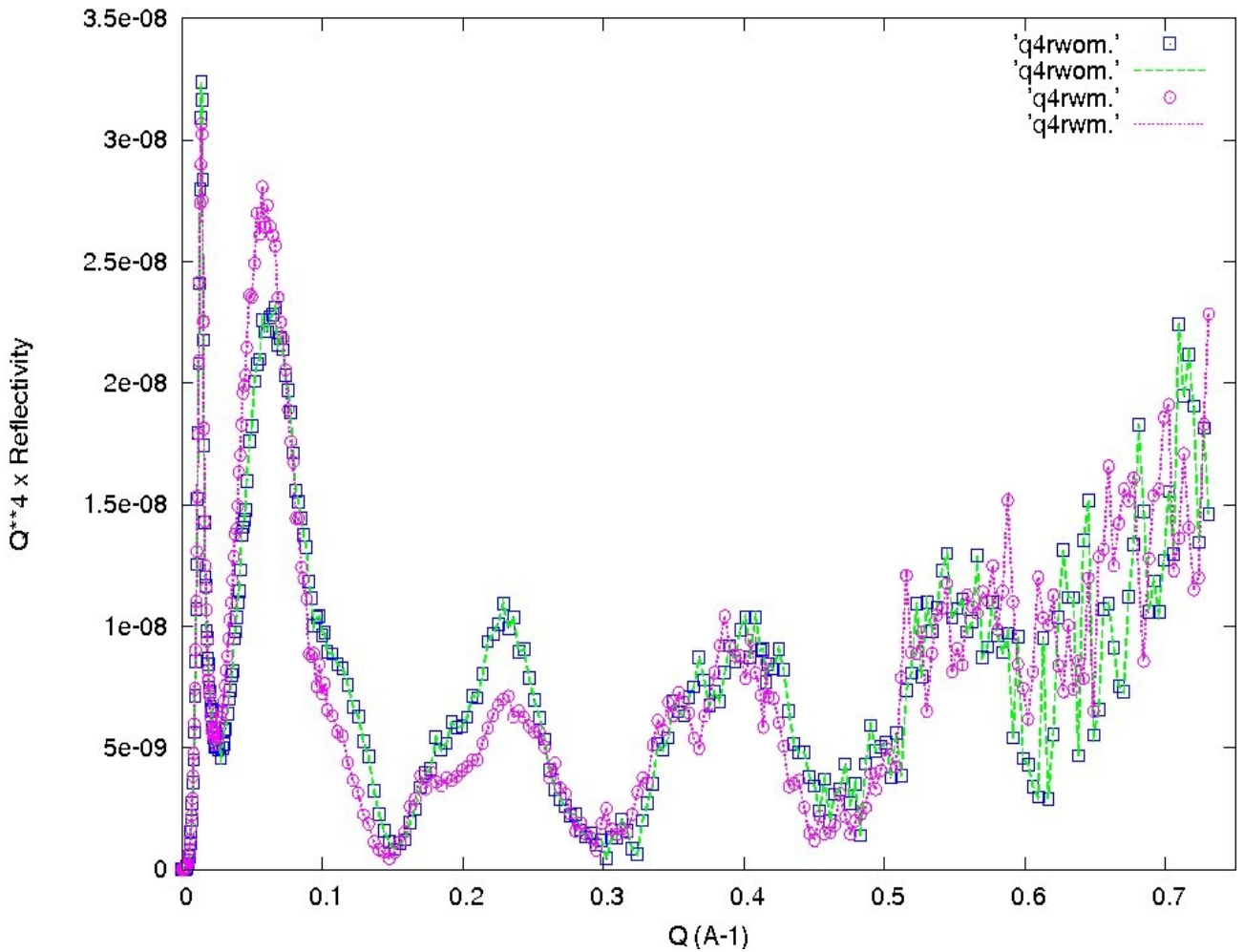
- depth of penetration into bilayer
- nature of pore (water-filled?)
- conformational changes
- random or ordered distribution?
- influence on surrounding lipids (location, conformation)



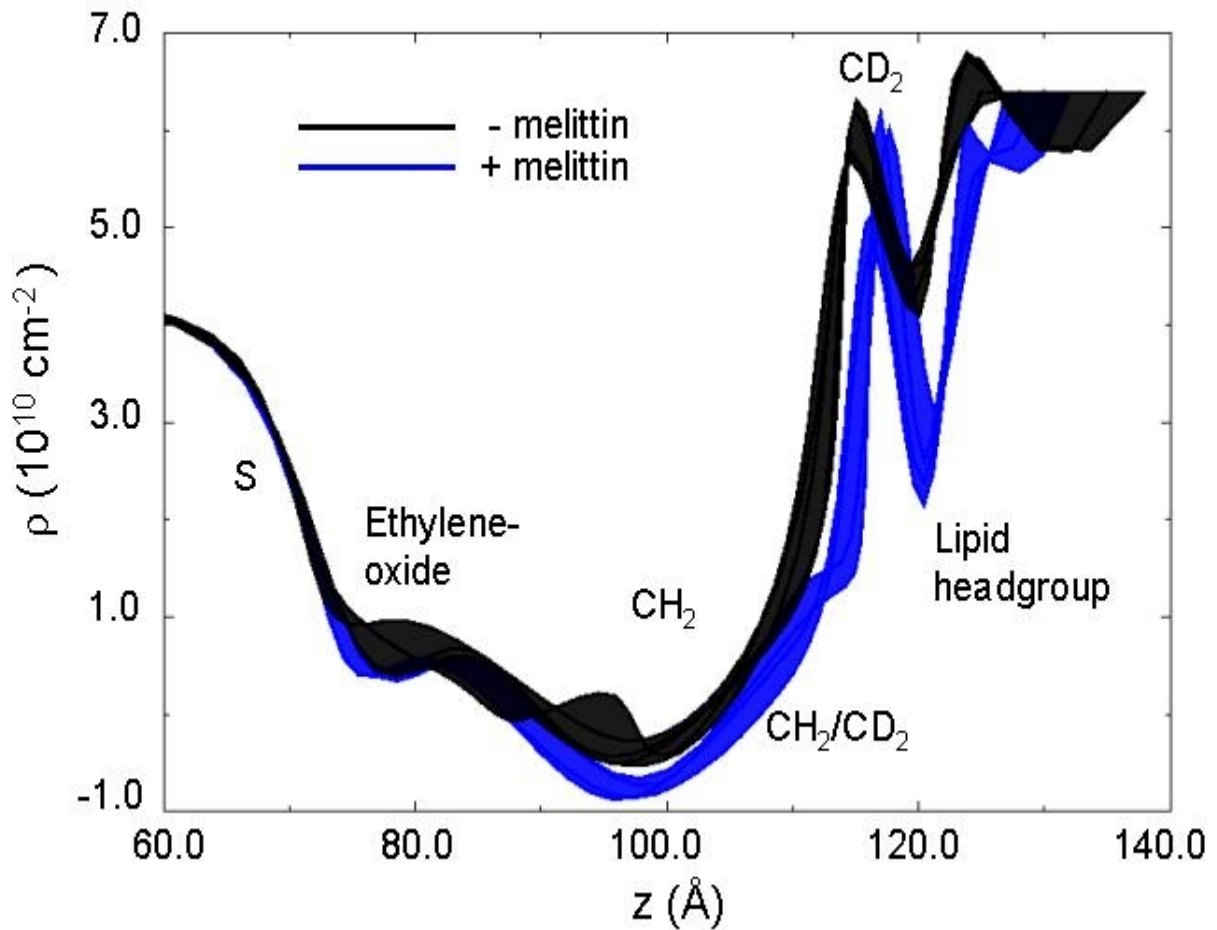
Fortunately, neutrons can be transmitted through macroscopic thicknesses of single crystal materials such as Si -- consequently, it is possible to construct fluid cells in which a deposited thin film structure of interest can be placed adjacent to an aqueous reservoir, for instance. Experiments can then be conducted as a function of PH, salinity, temperature, flow, etc., in-situ.



Specular neutron reflectivity data sets collected from a lipid bilayer membrane with and without exposure to melittin. Even on this log scale, significant differences are observable all across the reflectivity curves. Measurements of the reflectivity were obtained over nearly eight orders of magnitude and out to a Q of 0.72 inverse Angstroms -- which corresponds to a real space resolution of a fraction of a nano-meter in the SLD depth profile.

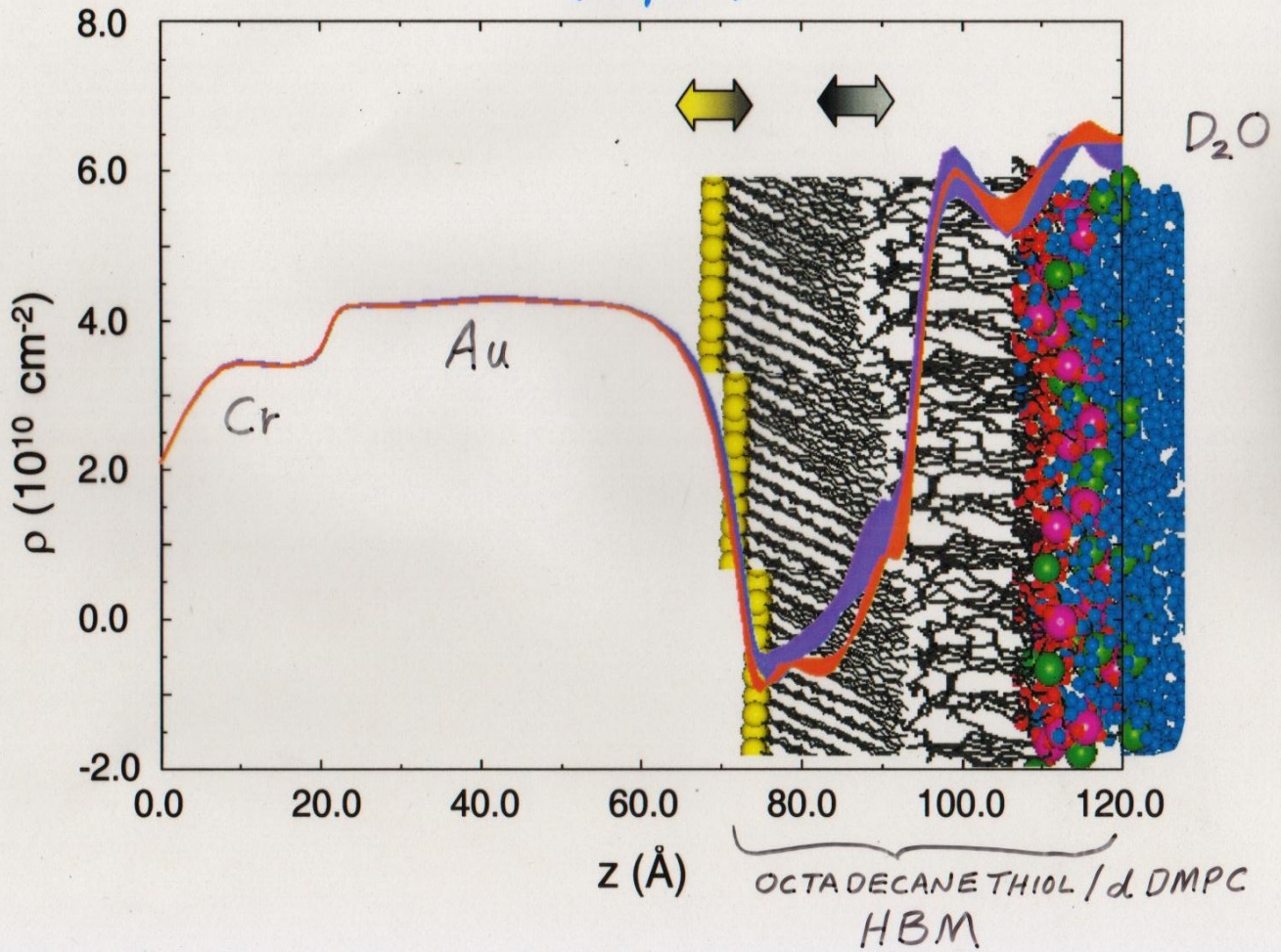


Multiplying the reflectivities of the previous slide by Q^4 enhances the differences between the data obtained with and without melittin.

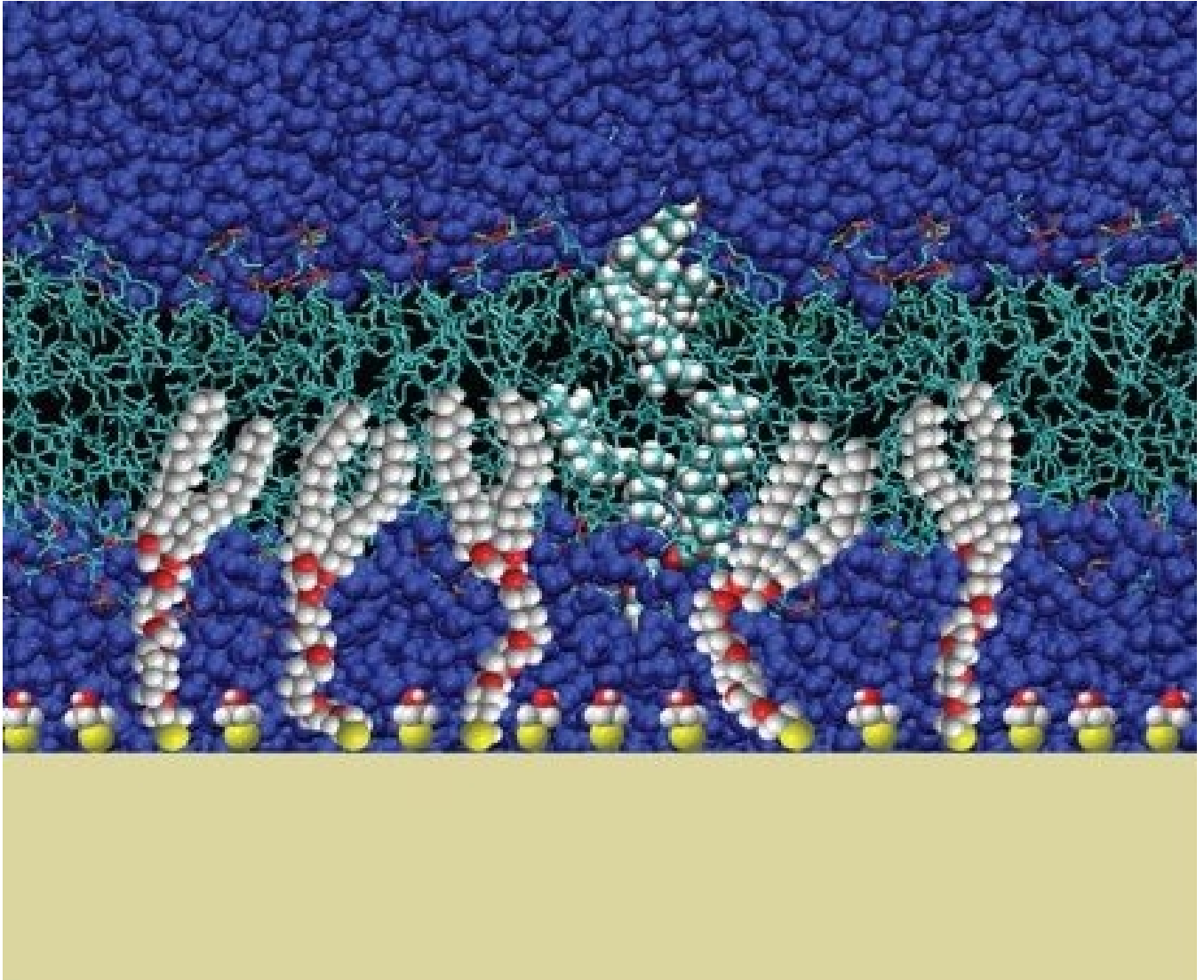


The scattering length density profiles obtained from fitting the reflectivity data -- the thickness of the plotted lines are a measure of the uncertainty in the SLD values. The data suggest that the melittin molecules perturb the outer leaflet of the bilayer membrane but do not penetrate significantly deeper.

S. KRUEGER, C. F. MAJKRZAK, N. F. BERK, M. TAREK, D. TOBIAS,
V. SILIN, J. A. DURA, C. W. MEUSE, J. WOODWARD, A. L. PLANT
(Langmuir)



Comparison of the SLD profile for the lipid bilayer (without melittin) as obtained from the specular neutron reflectivity measurement with that predicted by a molecular dynamics simulation.



Schematic representation of tethered bilayer being used as a support for trans-membrane type proteins in structural studies using NR (Courtesy David Vanderah et al.).

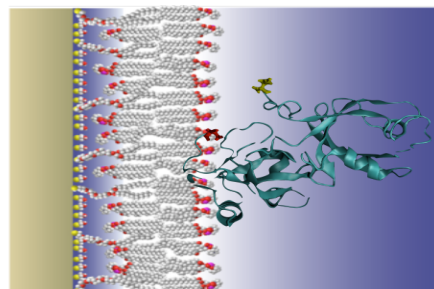
A sampling (on this and the next slide) of more recent specular NR studies of compositional depth profiles of biological macromolecules attached to or embedded in lipid bilayer membranes. These results are remarkable -- if not spectacular (at least in my opinion)!

Water-soluble membrane-associated proteins

>50% of biological NR beam time for biomedical applications using tBLMs

Active projects (last 2 cycles):

- Dengue
- Gaucher's disease
- GRASP
- HIV Gag & antibodies
- RSV & MLV
- Neurotransmitter
- OmpA/LA
- Parkinson's disease
- PTEN Tumor suppressor
- T-Cell receptor



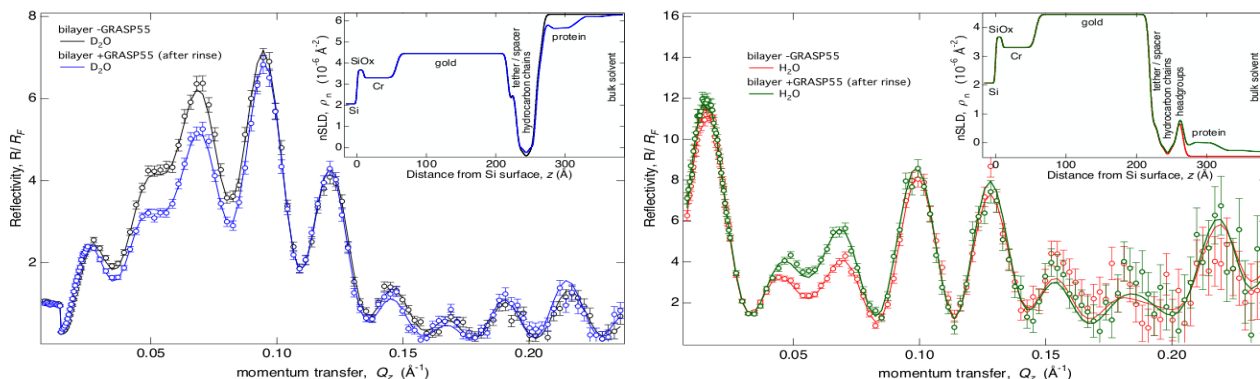
GRASP orientation at a tethered bilayer lipid membrane (tBLM) as determined by NR

Collaborative staff involvement:

- experimental planning
- substrate preparation
- tether synthesis
- neutron measurement
- data analysis

Bulent Akgun, Frank Heinrich, Mathias Lösche, Duncan McGillivray, Hirsh Nanda, David Vanderah

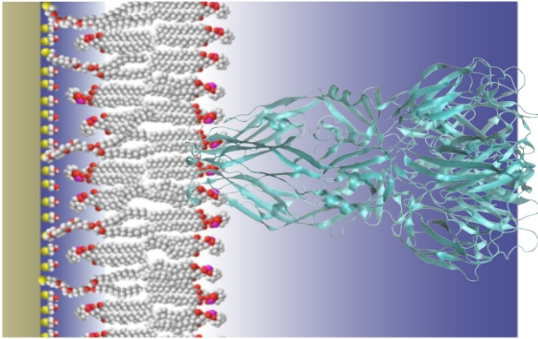
Typical reflectometry data for tBLM experiments



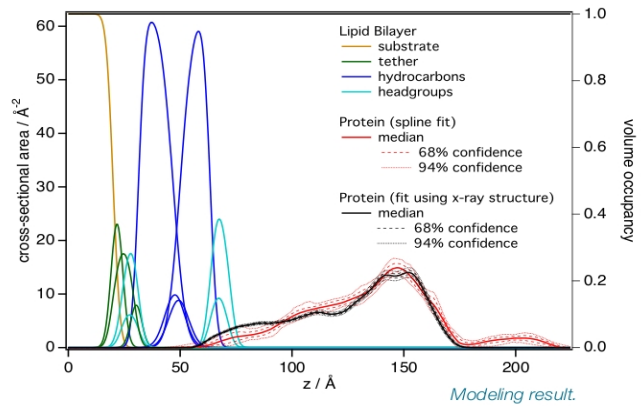
NR data measured on NG7, and best-fits for GRASP association with lipid membranes, project with A. Linstedt, University of Pittsburgh

Bulent Akgun, Frank Heinrich, Mathias Lösche, Duncan McGillivray, Hirsh Nanda

Example: Dengue Virus Envelope Protein



Visualization. Project with Mike Kent, Sandia National Labs.



Modeling result.

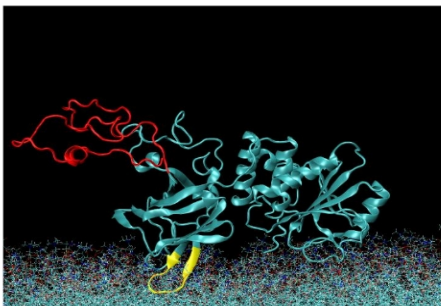
- Monte-Carlo Markov Chain uncertainty analysis
- Composition-space modeling of the bilayer
- Free-form fitting of structurally unknown components of the architecture
- Usage of PDB structure files for position and orientation of rigid proteins



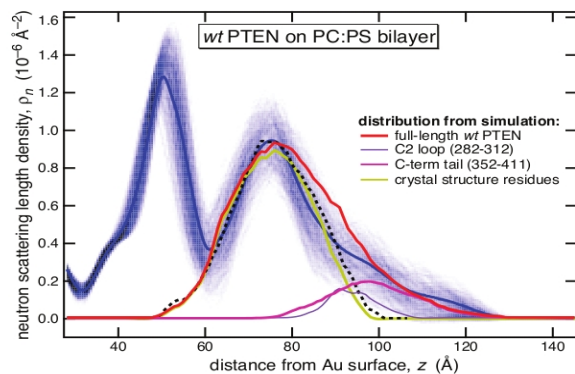
www.nsl.nist.gov/programs/reflect/

Bulent Akgun, Frank Heinrich, Paul Kienzle, Sushil Satija

Combining NR with Molecular Simulations



MD simulation snapshot of PTEN tumor suppressor association with a PS-containing lipid membrane



Comparison of MD and NR results, Shenoy, S. et al. J. Struct. Biol. 1-15 (2012).

Comparison of experimental data with results from:

- MD simulation
- Monte Carlo conformational search (SASSIE) results

Future Challenges:

- Ensemble averaging, integrating NR and simulation

Joseph Curtis, Mathias Lösche, Hirsh Nanda

The next series of slides shows a NR study of the location of water within a particular biomimetic membrane of interest to a vascular surgeon (who is attempting to develop synthetic replacements for arteries and veins in medical applications). Such synthetic vessels must have bio-compatible coatings which won't foster an immune system response.

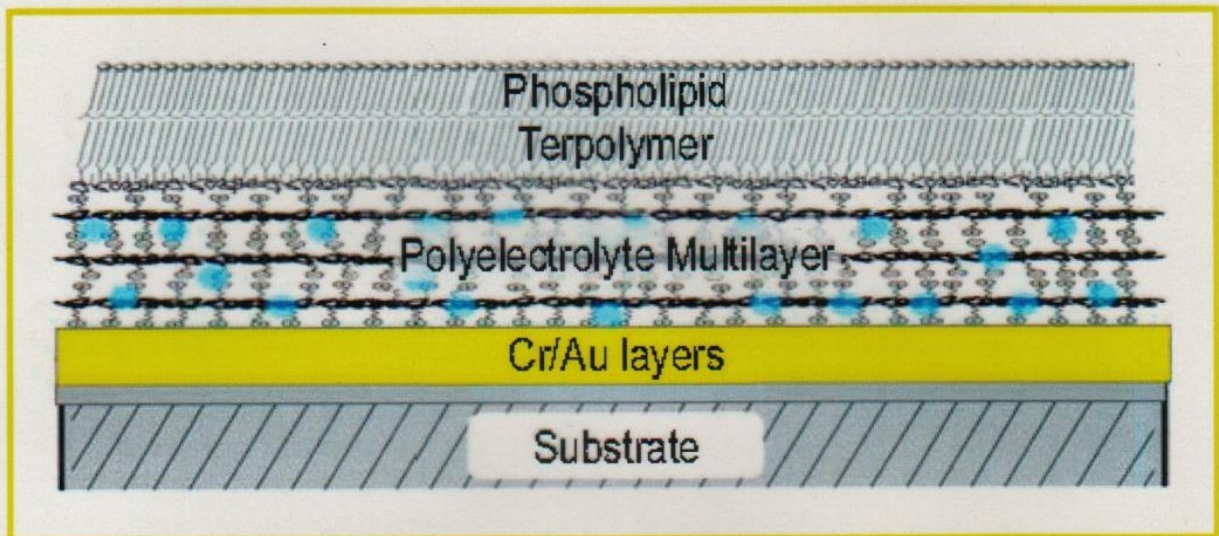
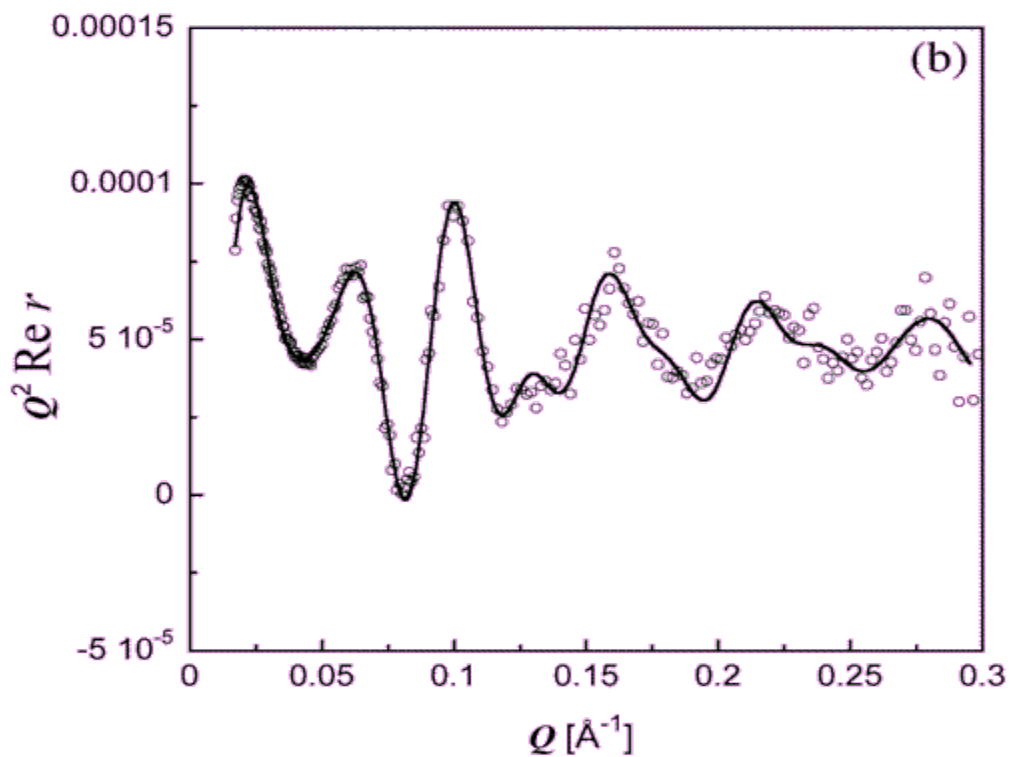
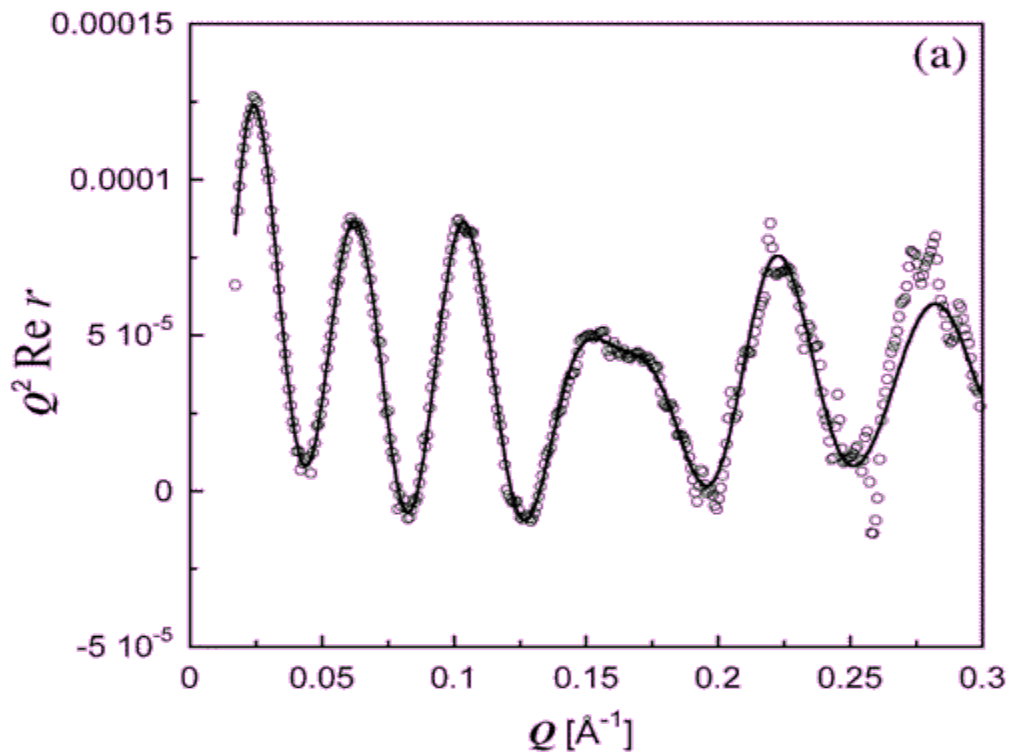


Fig. 1. Schematic diagram of a biomimetic membrane. The phospholipid layer at the top combines with the terpolymer layer to form a membrane-mimic that in turn resides on the water (blue dots) permeable "cushion" polyelectrolyte multilayer. The latter attaches electrostatically to the Au-capped substrate.

(Work of Ursula Perez-Salas, K. Faucher, E. Chaikof, et al.)



Typical real parts of reflection amplitudes obtained via phase-sensitive neutron reflectometry methods for the biomimetic film structure presented in the previous slides.

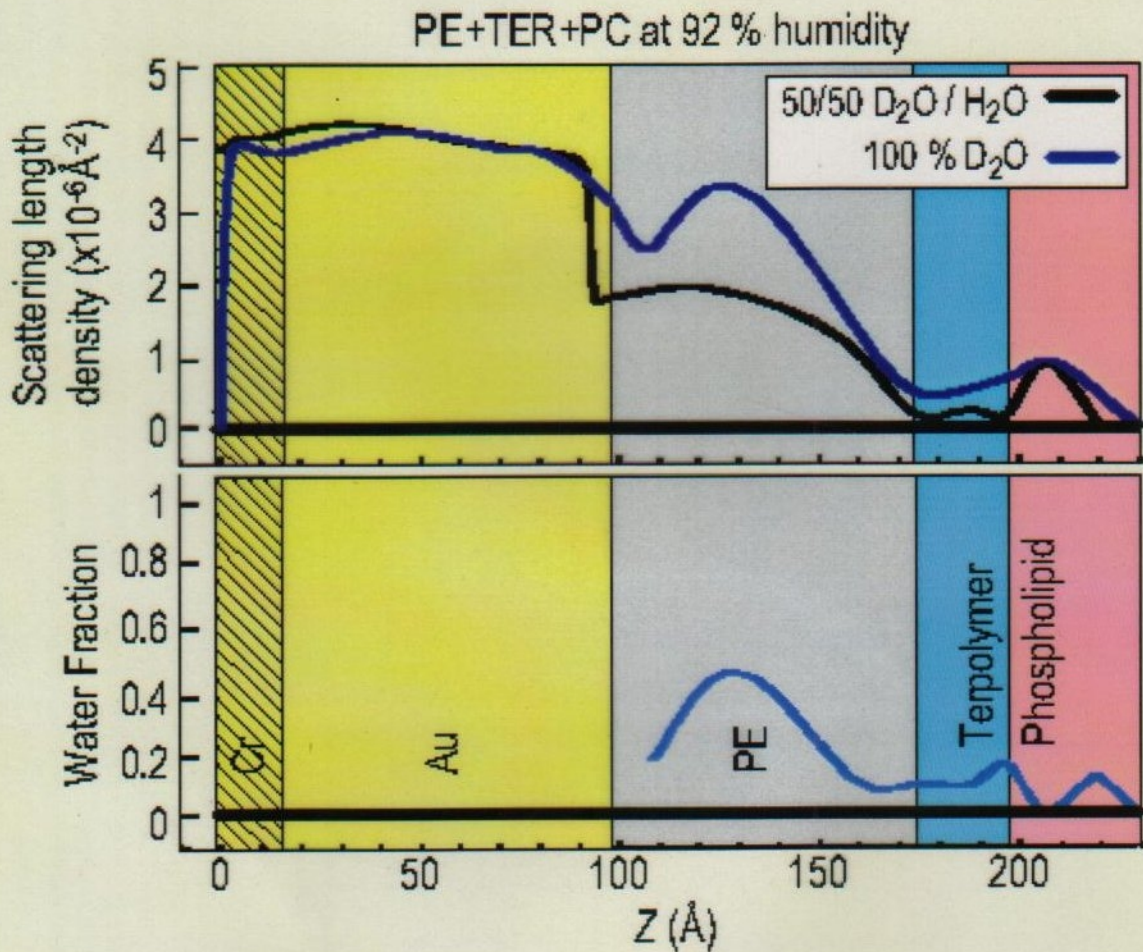


Fig. 3. Scattering length density profiles (top) and water fraction (bottom) for PE+TER+PC under indicated conditions.

After a number of different reflectivity measurements with various aqueous reservoir contrast values for $\text{H}_2\text{O} / \text{D}_2\text{O}$ ratios, it was possible to deduce, from the analysis of that data, the water distribution across the thickness of the film structure. As shown in the figure above, the water is found to reside primarily within the polyelectrolyte layer.

Nanoparticle distribution in polymer-based solar cells affects solar cell performance: A neutron reflectivity study

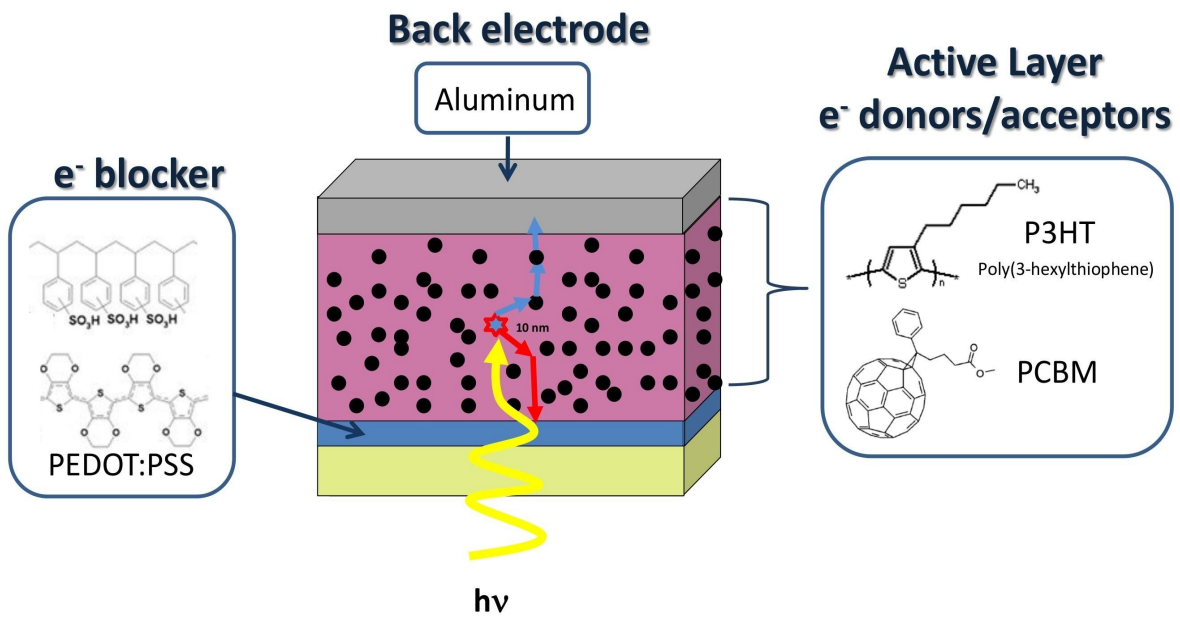
Jonathan Kiel¹, Brian Kirby², Charles Majkrzak²,
Brian Maranville², Michael Mackay³

Thursday, August 20th, 2009

- 1) Michigan State University, Department of Chemical Engineering and Materials Science
- 2) National Institute of Standards and Technology, Center for Neutron Research
- 3) University of Delaware, Materials Science and Engineering



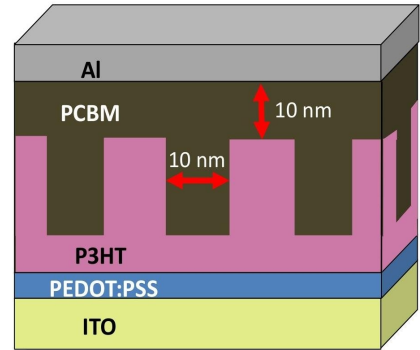
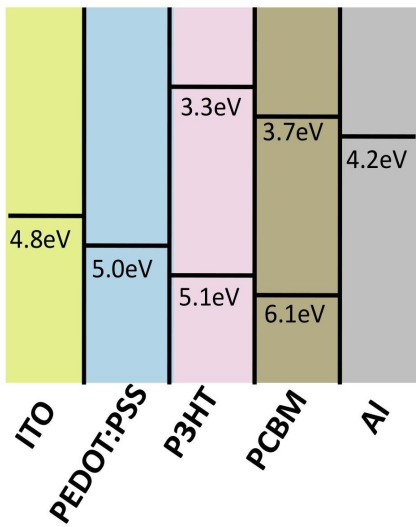
Components of organic solar cells



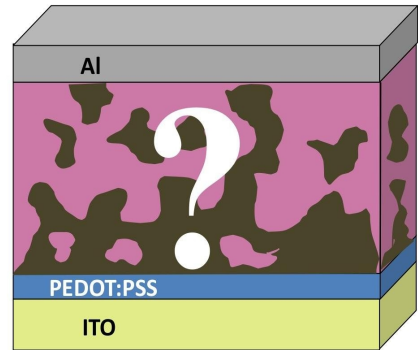
- Exciton diffusion length ~10 nm
- PCBM:P3HT morphology very important

What is the morphology of the active layer

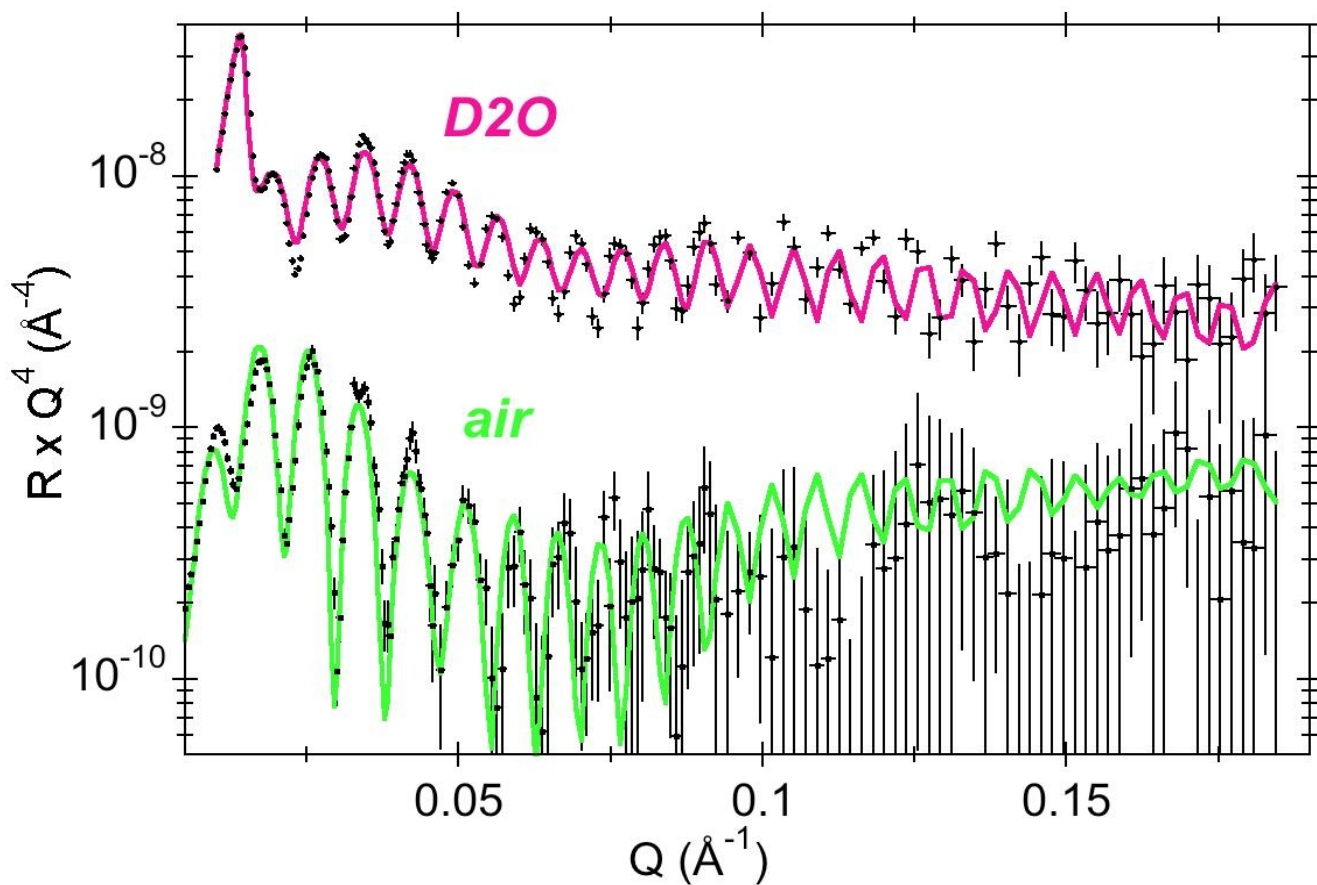
Energy Diagram of Organic Solar Cell



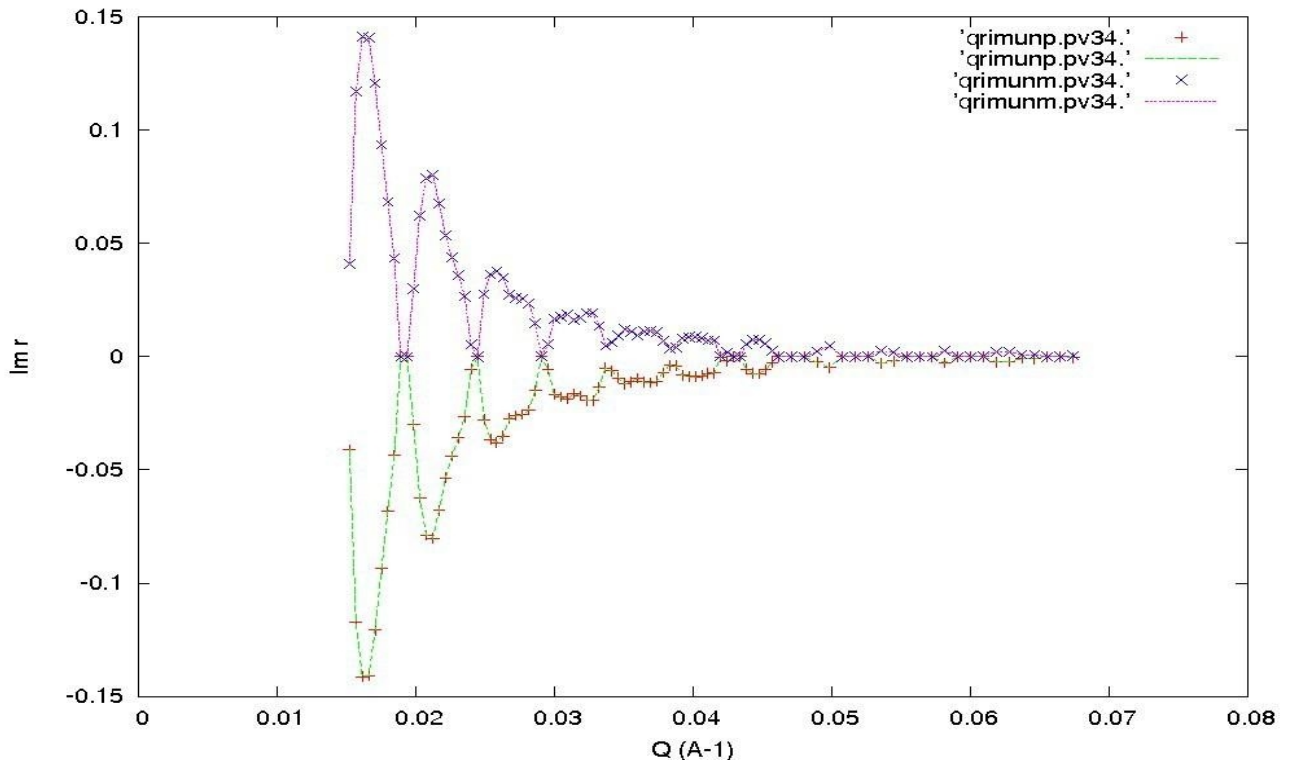
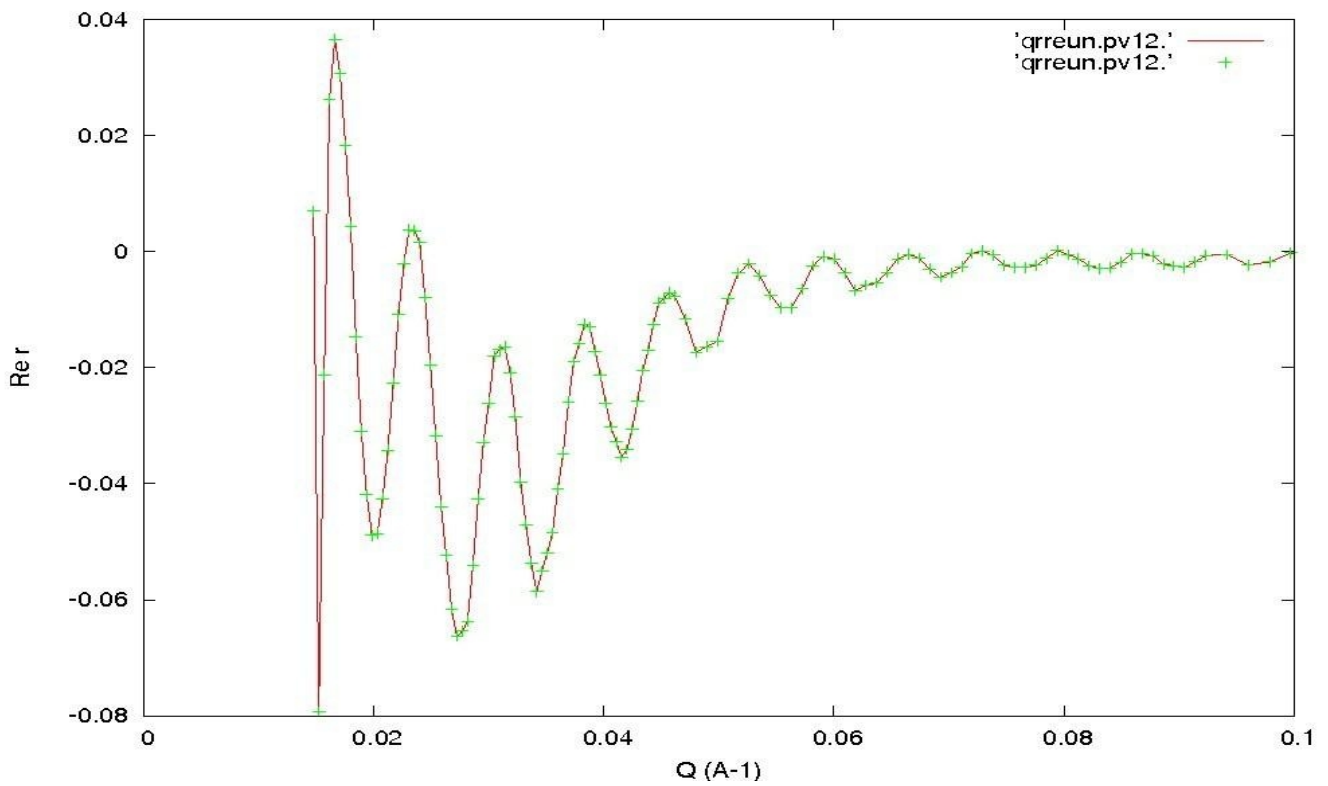
Idealized morphology



Actual morphology

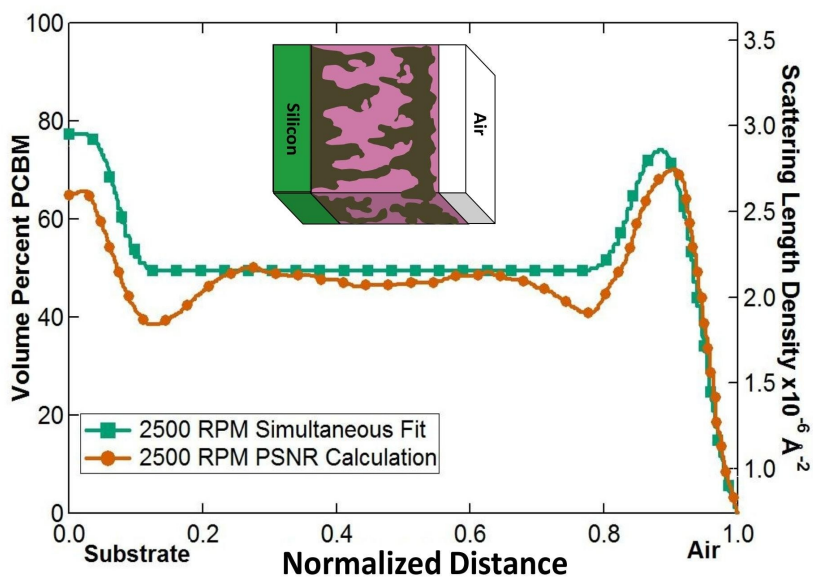


Reflectivity data collected from the same film system with two different backing media -- air and deuterated water. Once again, the reason for collecting such composite system (reference plus unknown part) reflectivity data is to be able to retrieve the phase information.



Real and imaginary parts of the reflection amplitude associated with the film structure alone -- as obtained from analysis of the composite system reflectivity data sets shown in the previous slide.

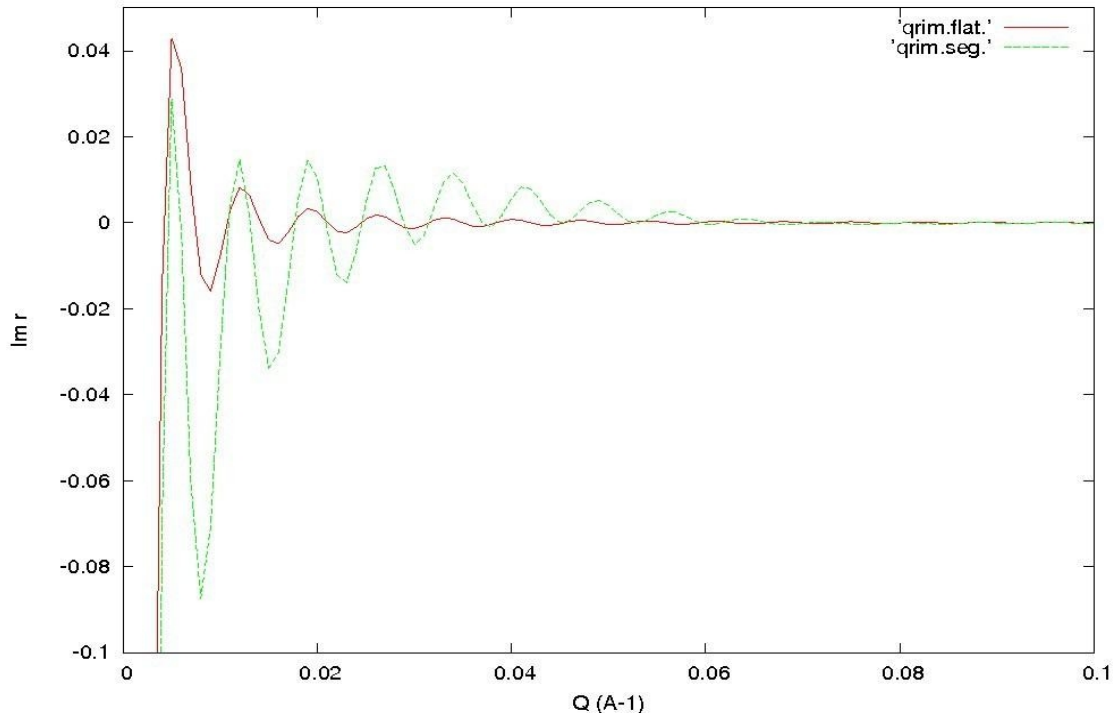
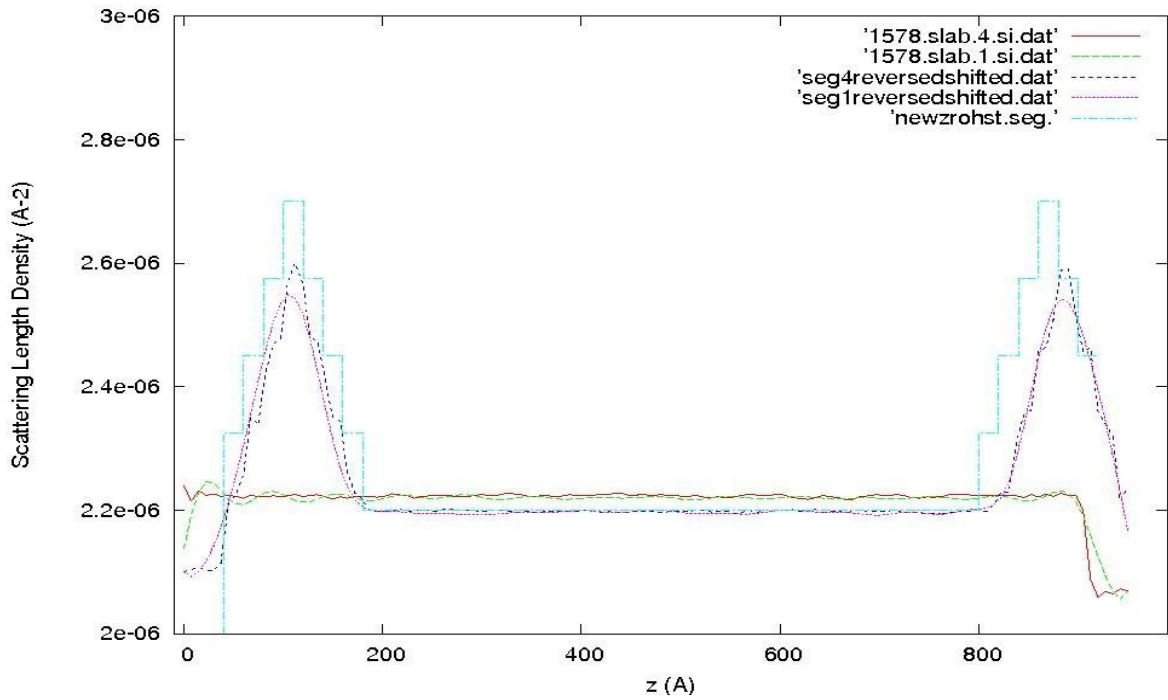
PCBM Volume % Comparison



- Simultaneous fitting and PSNR calculations show great agreement
- High PCBM concentration at substrate
- High PCBM concentration near air interface

$$\text{Vol\% PCBM} = \frac{\text{SLD}_{\text{measured}} - \text{SLD}_{\text{P3HT}}}{\text{SLD}_{\text{PCBM}} - \text{SLD}_{\text{P3HT}}}$$

SLD Depth Profile



The information contained in these plots makes it possible to rule out certain artifacts -- see the original reference for a detailed discussion (COICIS paper cited in the references at the end of this presentation).

Appendices

- <> Solving the one-dimensional Schroedinger wave equation of motion to obtain an expression for the reflection amplitude r in integral form
- <> Solution for the SLD depth profile of an arbitrary object within the Born approximation

$$M_j = \begin{bmatrix} \cos \delta_j & \frac{1}{n_{x_j}} \sin \delta_j \\ -n_{x_j} \sin \delta_j & \cos \delta_j \end{bmatrix} \quad (11)$$

with $\delta_j = k_{ox} n_{x_j} \Delta_j$, with n_{sx} and n_{ox} corresponding to the substrate and incident medium, respectively. The j th matrix M_j corresponds to the j th slab of thickness Δ_j wherein the scattering density is assumed to be constant and equal to ρ_j . The amplitude of the incident wave is assumed to be unity. The transmission and reflectivity are $T^*T = |T|^2$ and $R^*R = |R|^2$, respectively, and can be obtained directly from Equation (9).

Thus, for a given model potential, it is straightforward to calculate the expected reflectivity. Unfortunately, the converse of this statement is not necessarily true, as will be discussed in more detail in Section 4.

At this point it is useful to consider an alternate derivation of the reflectivity from which the Born approximation (corresponding to the kinematic limit which is discussed below) and other useful results can be directly obtained. Suppose that there exist two arbitrary but different density profiles $\rho_1(x)$ and $\rho_2(x)$ for which the corresponding, separate reflectivities are to be calculated. In each case we take the incident wave to propagate from left to right. We then have to solve the following pair of equations (derived from equations 6 and 7):

$$\psi_j''(x) + [k_{ox}^2 - 4\pi\rho_j(x)] \psi_j(x) = 0 \quad j = 1, 2 \quad (12)$$

for $-\infty < x < \infty$ where $\psi_1(x)$ and $\psi_2(x)$ are the exact solutions in each case. From these we can construct the Wronskian function

$$W(x) \equiv W[\psi_1(x), \psi_2(x)] = \psi_1(x)\psi_2'(x) - \psi_1'(x)\psi_2(x). \quad (13)$$

Differentiating both sides of eq. (13) and using eq. (12) we obtain

$$W'(x) = -\psi_1(x)4\pi\rho_{12}(x)\psi_2(x) \quad (14)$$

where

$$\rho_{12}(x) \equiv \rho_1(x) - \rho_2(x) \quad (15)$$

Equation (14) tells us that $W(x)$ is a constant over intervals where the two density profiles coincide, $\rho_1(x) = \rho_2(x)$, which is a property we will exploit to obtain a formula relating the reflectivities for each profile. First, assume that $\rho_1 \neq \rho_2(x)$ only within an interval $\ell_1 < x < \ell_2$. We allow subintervals of (ℓ_1, ℓ_2) where $\rho_1(x) = \rho_2(x)$, but we demand finite ℓ_1 and ℓ_2 such that $\rho_1(x) = \rho_2(x)$ for all $x < \ell_1$ and for all $x > \ell_2$. We also assume that the wave is incident in vacuum so for $x < \ell_1$, $\rho_1(x) = \rho_2(x) = 0$. The wavefunctions for $x < \ell_1$ are then

$$\psi_j(x) = e^{ik_{ox}x} + R_j e^{-ik_{ox}x} \quad (16)$$

where R_1 and R_2 are the reflection amplitudes for each problem. Similarly, we assume that each density profile has a common substrate so that for $x > \ell_2$, $\rho_1(x) = \rho_2(x) = \rho(\infty)$. The wavefunctions for $x > \ell_2$ are then

$$\psi_j(x) = T_j e^{iKx} \quad (17)$$

where

$$K = \sqrt{k_{ox}^2 - 4\pi\rho(\infty)} \quad (18)$$

and T_1 and T_2 are the transmission amplitudes in each problem. Now we see that for the given pair of profile functions $\rho_1(x)$ and $\rho_2(x)$, $W(x)$ is uniquely determined everywhere and varies with x only in (ℓ_1, ℓ_2) , where $\rho_1(x)$ and $\rho_2(x)$ can differ. Substituting (17) into (13) we obtain

$$W(x) = 0 \quad (19)$$

for all $x \geq \ell_2$, since $\psi_1(x)$ and $\psi_2(x)$ are proportional to one another (linearly dependent) in this region. However, substituting (16) into (13) we get

$$W(x) = 2ik_{ox}(R_1 - R_2) \quad (20)$$

for all $x \leq \ell_1$, which is a complex constant. Finally, for $\ell_1 < x < \ell_2$ we integrate both sides of equation (14) to obtain

$$\int_{\ell_1}^{\ell_2} W'(x)dx = W(\ell_2) - W(\ell_1) = -\alpha_{12} \quad (21)$$

where

$$\alpha_{12} = \int_{\ell_1}^{\ell_2} \psi_1(x)4\pi\rho_{12}(x)\psi_2(x)dx \quad (22)$$

Now $W(x)$ is continuous everywhere since $\psi_j(x)$ and $\psi_j'(x)$ are. Thus, evaluating (19) and (20) at $x = \ell_2$ and $x = \ell_1$, respectively, we find $W(\ell_2) = 0$ and $W(\ell_1) = 2ik_{ox}(R_1 - R_2)$. Thus, from equation (21) we get

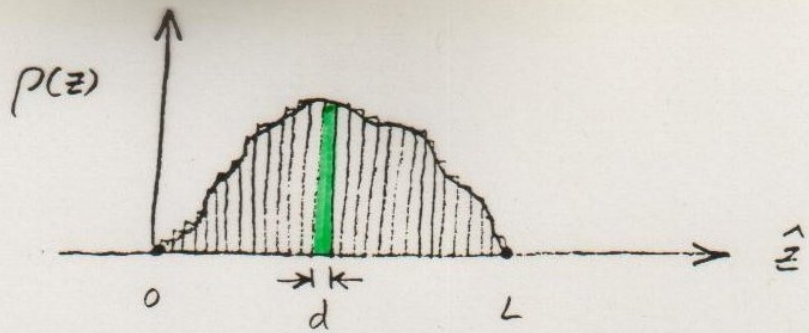
$$R_1 = R_2 + \frac{\alpha_{12}}{iQ} \quad (23)$$

where again $Q = 2k_{ox}$ is the wavevector transfer. Equation (23) is the general formula we set out to derive and is a handy starting point for exact treatments as well as approximation schemes.

For example, consider any $\rho(x)$ which vanishes identically for $x < \ell_1$ and for $x > \ell_2$. Then, in equation (23) we can set $\rho_1(x) = \rho(x)$, $\psi_1(x) = \psi(x)$, and $R_1 = R$ whereas for the "other" density profile we take $\rho_2(x) = 0$ everywhere so that $\psi_2(x) = \exp(ik_{ox}x)$ and $R_2 = 0$. Combining equations (22) and (23) then gives the exact solution of the reflectivity for an arbitrary scattering density profile $\rho(x)$:

$$R = \frac{4\pi}{iQ} \int_{-\infty}^{+\infty} \psi(x)\rho(x)e^{ik_{ox}x} dx \quad (24)$$

where we have formally extended the integration over all x , though only the region where $\rho(x) \neq 0$ contributes. Although it may not be obvious from the derivation, equation (24) also holds if we allow $\rho(x)$ to be nonzero as $x \rightarrow \infty$, as long as the integral exists. Note that (24) requires, to be exact, the exact wavefunction $\psi(x)$ wherever $\rho(x) \neq 0$. The corresponding expression for the reflectivity $|R|^2$, is



ARBITRARY POTENTIAL DIVIDED INTO
RECTANGULAR SLABS OF WIDTH
 d AND CONSTANT P

THEN

(BORN APPROX)

$$\text{Re } r(Q) \approx \frac{4\pi}{Q} \int_0^L p(z) \sin(Qz) dz$$

BECOMES

$$\begin{aligned} \text{Re } r(Q_j) &\approx \frac{4\pi}{Q_j} \sum_{l=1}^N \int_{(l-1)d}^{ld} P_l \sin(Q_j z) dz \\ &= \frac{-4\pi}{Q_j^2} \sum_{l=1}^N P_l \left[\cos(Q_j z) \right]_{(l-1)d}^{ld} \end{aligned}$$

SET OF
Re r FOR
DIFFERENT
VALUES OF
Q OR θ

$$\begin{cases} \text{Re } r_1 = C_{11} P_1 + C_{12} P_2 + \dots + C_{1N} P_N \\ \text{Re } r_2 = C_{21} P_1 + C_{22} P_2 + \dots + C_{2N} P_N \\ \vdots \\ \text{Re } r_N = C_{N1} P_1 + C_{N2} P_2 + \dots + C_{NN} P_N \end{cases}$$

SOLVE SIMULTANEOUS EQUATIONS FOR P_l 's GIVEN $\text{Re } r$'s
e.g., SVD, EIGENVALUE PROBLEM FORMULATION, ...

$$\underbrace{\operatorname{Re} r_{\text{BA}}(Q) \left[\frac{Q^2}{8\pi \sin\left(\frac{Qd}{2}\right)} \right]}_{\equiv \mathcal{I}(Q)} = \sum_{j=1}^N \rho_j \sin\left[\frac{(2j-1)Qd}{2} \right]$$

$$\int_0^{\pi} \sin m\theta \sin n\theta d\theta = \begin{cases} 0 & m, n \text{ INTEGERS, } m \neq n \\ \frac{\pi}{2} & m, n \text{ INTEGERS, } m = n \end{cases}$$

ORTHOGONALITY

$$\rho_j = \frac{d}{4\pi^2} \int_0^{\frac{\pi}{d}} Q^2 \operatorname{Re} r_{\text{BA}}(Q) \frac{\sin\left[\frac{(2j-1)Qd}{2}\right]}{\sin\left(\frac{Qd}{2}\right)} dQ$$

Bibliography / References

Optics, 3rd Ed., by E. Hecht, Addison-Wesley, 1998.

Neutron Optics, by V.F. Sears, Oxford University Press, 1989.

Principles of Optics, 6th Ed., by M. Born and E. Wolf, Pergamon Press, 1987.

Quantum Mechanics, 2nd Ed., by E. Merzbacher, Wiley, 1970.

“Structural Investigations of Membranes in Biology by Neutron Reflectometry”, C.F.Majkrzak, N.F.Berk, S.Krueger, and U.A.Perez-Salas, Chapter 12 in *Neutron Scattering in Biology*, Edited by J.Fitter, T.Gutberlet, and J.Katsaras, (Springer, Berlin, 2006) p.225-263.

“Polarized Neutron Reflectometry”, C.F.Majkrzak, K.V.O'Donovan, and N.F.Berk, Chapter 9 in *Neutron Scattering from Magnetic Materials*, Edited by T.Chatterji, (Elsevier, Amsterdam, 2006) p.397-471.

“Phase-Sensitive Neutron Reflectometry”, C.F.Majkrzak, N.F.Berk, and U.A.Perez-Salas, *Langmuir* **19**, 7796 – 7810 (2003).

B.J.Kirby et al., Phase-sensitive specular neutron reflectometry . . . , *Current Opinion in Colloid & Interface Science* **17** (2012) 44-53.

C.F.Majkrzak et al., *J. Appl. Phys.* **110** (2011).

www.ncnr.nist.gov -- look here for information about neutron reflectometry in general as well as in specific studies highlighted in past and current annual reports for the facility.